Design and Manufacturing of Hierarchical Multi-Functional Materials Via High Resolution additive Manufacturing

Master's Thesis of Matthias Ottmar Karch
Department of Computer Integrated Design
Prof. Dr.-Ing. R. Anderl
Department of Mechanical Engineering
Prof. Dr. Xiaoyu (Rayne) Zheng

TECHNISCHE UNIVERSITÄT DARMSTADT

VirginiaTech
Invent the Future

Design and Manufacturing of Hierarchical Multi-Functional Materials Via High Resolution additive Manufacturing

Master's Thesis of Matthias Ottmar Karch
Department of Computer Integrated Design
Prof. Dr.-Ing. R. Anderl
Department of Mechanical Engineering
Prof. Dr. Xiaoyu (Rayne) Zheng

Matthias Ottmar Karch
TUD-ID: **1794904**
VT-ID: **906059143**
Degree program: Mechanical and Process Engineering

Master's Thesis
Topic: "Design and Manufacturing of Hierarchical Multi-Functional Materials Via High Resolution additive Manufacturing"
Thema: „Design und Herstellung von hierarchisch multifuktionalen Materialien durch hochauflösende Additivherstellung"

Submission Date: 2017-08-11

Advisor: M.Sc. Cordula Auth

Prof. Dr.-Ing. Reiner Anderl
Department of Computer Integrated Design
University Department of Mechanical Engineering
Technische Universität Darmstadt
Otto-Berndt-Straße 2
D-64287 Darmstadt

Prof. Dr. Xiaoyu (Rayne) Zheng
Advanced Manufacturing and Metamaterials Laboratory
Department of Mechanical Engineering, College of Engineering
Virginia Polytechnic Institute and State University
635 Prices Fork Road
24061 Blacksburg, VA

Thesis Statement

Thesis Statement pursuant to § 22 paragraph 7 of APB TU Darmstadt

I herewith formally declare that I have written the submitted thesis independently. I did not use any outside support except for the quoted literature and other sources mentioned in the paper. I clearly marked and separately listed all of the literature and all of the other sources which I employed when producing this academic work, either literally or in contend.

This thesis has not been handed in or published before in the same or similar form. In the submitted thesis, the written copies and electronic version are identical in content

Darmstadt, 08/11/2017
(Location, Date)

Matthias Kaul
(Signature)

TECHNISCHE UNIVERSITÄT DARMSTADT

Master-Thesis

für
Matthias Karch (1794904)

Design und Herstellung von hierarchisch multifuktionalen Materialien durch hochauflösende Additivherstellung

Design and Manufacturing of Hierarchical Multi-Functional Materials Via High Resolution additive Manufacturing

Nowadays the research in additive manufacturing plays an important role in building lightweight structures in micro- or nano-scale with high stiffness and strength. High resolution Projection Microstereolithography (PμSL) is a promising technique of this area which uses polymer, ceramic or metal powder as feedstock to create ultralight materials with designed complex architectures and the rising need of products with high resolution.
Not only the structural design criteria (weight, stiffness and strength) but also other functional attributes (e.g. thermal expansion management, responsive materials) of these structures has an enormous technological importance. For specific applications, there is only a tiny or no thermal expansion tolerable. Thermal expansion can lead to structural damage or failure of the device in these cases. For this reason, it is necessary to fabricate a structure with controllable - preferable zero or negative - thermal expansion.
The main tasks for this research are:

- Investigate the base material regarding the coefficient of thermal expansion
- Fabrication of hierarchical 1st and 2nd order micro-architectures with tunable negative thermal expansion based on hierarchical bi-material design based on multi-material additive manufacturing
- Demonstrate tunable volume shrinkage in metamaterials based on 1st and 2nd order hierarchical materials
- Verify results with experimental measurements of the thermal mechanical properties of these materials
- Improvement of printing efficiency of the multi-material printing system
- Generate CAD modeling that is capable of integration with multiple material attributes
- Use simulation software to evaluate negative thermal expansion and design of a new structure

Betreuer: Cordula Auth, M. Sc.
Umfang der Arbeit: 30 CP

Prof. Dr.-Ing. R. Anderl

Fachgebiet Datenverarbeitung in der Konstruktion

Department of Computer Integrated Design

Prof. Dr.-Ing. Reiner Anderl

Otto-Berndt-Straße 2
64287 Darmstadt

Tel. +49 6151 16 - 21791
Fax +49 6151 16 - 21793
anderl@dik.tu-darmstadt.de

Datum
24.04.2017

TECHNISCHE UNIVERSITÄT DARMSTADT

Master-Thesis

für
Matthias Karch (1794904)

Design und Herstellung von hierarchisch multifuktionalen Materialien durch hochauflösende Additivherstellung

Design and Manufacturing of Hierarchical Multi-Functional Materials Via High Resolution additive Manufacturing

Additive Fertigungsverfahren bieten die Möglichkeit, Produkte und Bauteile zu fertigen, die bisher mit keinem anderen Verfahren oder nur unter hohem Kostenaufwand herzustellen sind. Auch in Bezug auf die Fertigung von Leichtbau-Strukturen im Mikro- oder Nanobereich mit hoher Steifigkeit und Festigkeit spielen additive Fertigungsverfahren eine wichtige Rolle. Ein vielversprechendes Fertigungsverfahren ist die Mikro-Stereolithographie. Neben strukturellen existieren weitere Konstruktionsregeln von hoher technischer Relevanz. Diese betreffen beispielsweise den thermischen Verzug eines Bauteils. Dieser sollte bei bestimmten Fällen möglichst gering bzw. im besten Fall gar nicht vorhanden sein. Aus diesem Grund sind Konstruktionsregeln notwendig, die einen Wärmeverzug nach Möglichkeit verhindern bzw. notfalls zu einem negativen Verzug führen. Das Ziel der Master-Thesis ist daher die Erstellung einer Methode, die bei der Auslegung von Bauteilen unterstützt und die entwickelten Konstruktionsregeln automatisiert berücksichtigt, um eine hohe Bauteilgüte zu erreichen.

Fachgebiet Datenverarbeitung in der Konstruktion

Department of Computer Integrated Design

Prof. Dr.-Ing. Reiner Anderl

Otto-Berndt-Straße 2
64287 Darmstadt

Tel. +49 6151 16 - 21791
Fax +49 6151 16 - 21793
anderl@dik.tu-darmstadt.de

Datum
24.04.2017

Abstract

This master's thesis deals with the coefficient of thermal expansion of 1st and 2nd order unit cells and the improvement of the multi-material printer. The first step is to compute the theoretical thermal expansion of a multi-material 1st and 2nd order octet-truss by using different ratios between the material with high and low thermal expansion and by changing the skew angle. Afterwards, the as base material used resins are investigated with regards to their coefficient of thermal expansion to get a selection of materials with high and low thermal expansion for assigning them to the tested samples.

Thermal expansion tests of multi-material unit cells of 1st and 2nd order octet-truss with a high ratio of the coefficient of thermal expansion and various skew angles are conducted to proof the analytic prediction for achieving a negative volumetric coefficient of thermal expansion.

After a series of thermal expansion tests for the octet-truss, the literature was reviewed to check other unit cells regarding their potential to shrink by assigning them materials with different coefficient of thermal expansion. Modified versions of the dodecahedron and the – here called – quatraeder are promising in this case and further investigated. Especially the latter one is analyzed at its second hierarchical order and offers an even more negative volumetric coefficient of thermal expansion than the octet-truss.

Moreover, the home-made prototype of a multi-material printer is analyzed regarding its reliability and use of resources. Actions like a list of requirements and the creation of a morphologic box are taken to find a suitable solution to improve the current system. By creating three different concepts of the morphological matrix, the concepts are rated and the best one is chosen to be implemented. The implementation of the measures that led to a proper working printer include a revision of the setup, the recoating, as well as the washing and drying process. Furthermore, the design is reconsidered and redesigned for both faster and easier execution of changes. In this way a reduction in the use of resources, the avoidance of contamination, and the increase of reliability is assured.

3D-printing, Microstereolithography, Coefficient of Thermal Expansion

Acknowledgements

First, I would like to thank my advisors Prof. Dr. Xiaoyu Zheng from Virginia Tech Blacksburg and Prof. Dr.-Ing. Reiner Anderl and Ms. M.Sc. Cordula Auth from Technische Universität Darmstadt for their guidance, support and offering me the chance to work in their research area. Secondly, I would like to thank Prof. Dr. Jan Helge Bøhn from Virginia Tech Blacksburg and Prof. Dr.-Ing. Manfred J. Hampe from Technische Universität Darmstadt for creating this wonderful Dual Degree Master Program and enabling me to be a part of it. It was a great pleasure and experience to study at both universities and definitely made me grow in an academic and personal way.

I would also like to thank my lab mates Huachen Cui and Ryan Hensleigh with whom I enjoyed collaborating.

My special thanks also goes to my good friend Athulya Simon from Virginia Tech Blacksburg for her feedback as the second reader of my master's thesis.

Table of Contents

Table of Figures

Table of Tables

Table of Abbreviations

3D	Three-Dimensional
3DP	3D-Printing
ABS	Acrylonitrile Butadiene Styrene
AM	Additive Manufacturing
BMP	Bitmap
C	Carbonate
CAD	Computer Aided Design
CNC	Computerized Numerical Control
CTE	Coefficient of Thermal Expansion
d	Dodecahedron
DC	Direct Current
DMD	Digital Micromirror Device
FLM	Fused Layer Modeling
H	Hydrogen
ID	Identification
LabVIEW	Laboratory Virtual Instrumentation Engineering Workbench
LASER	Light Amplification by Stimulated Emission of Radiation
LED	Light Emitting Diode
LLM	Layer Laminated Manufacturing
MATLAB	MATrix LABoratory
MPμSL	Mask Projection Microstereolithography
PDMS	Polydimethylsiloxane
PLA	Polylactide
q	Quatraeder
SLM	Selective Laser Melting
SL	Stereolithography
SLS	Selective Laser Sintering
STL	STereoLithography
TUD	Technische Universität Darmstadt
UC	Unit Cell
UV	Ultraviolet
VT	Virginia Polytechnic Institute and State University, also called Virginia Tech

Table of Formulas

Latin Letters:

Symbol	Unit	Description
E	MPa	Young's modulus
h	mm	height
I	mm^4	second moment of area
Δl	-	length difference in pixel
l	-	length in pixel
n	-	multiplication factor
ΔT	°C	temperature difference
T	°C	temperature
T_G	°C	glass transition temperature
w	mm	width
x	-	x-coordinate
y	-	y-coordinate

Greek Letters:

Symbol	Unit	Description
α	1/°C	coefficient of thermal expansion
ε	-	strain
θ	°	skew angle
σ	N/mm^2	stress

1 Introduction

This master's thesis deals with the research project about the ascertainment of the coefficient of thermal expansion (CTE) of lightweight structures that shrink under thermal load instead of expanding. Moreover, the home-made 3D-printer that uses the technique of mask projection microstereolithography (MPμSL), an additive manufacturing (AM) method, is improved. The following sections state the problems that were faced during this work and also the motivation and research objectives to solve these issues. Furthermore, the methodology shows the structured approach taken to complete this thesis.

1.1 Statement of the Problems

Nowadays the requirements for structures and components are steadily increasing, especially for commercial applications in microsystems, microrobotics, or biomedical fields. One way to deal with this challenge is through the manufacturing of these components with microstereolithography. Microstereolithography is a category of additive manufacturing that combines the areas of rapid prototyping with microengineering. Having a high resolution makes microstereolithography more than just simple rapid prototyping. It is used for creating complex three-dimensional parts. [BJB02][GRS15] One of these parts in micro architecture is the octet-truss. It is a typical sample of a lightweight structure that is capable of bearing high loads, like tension or compression, at a low relative density. [ZLW14] Besides the advantage of these structures regarding their mechanical capacity to withstand stresses, another factor that plays an important role for highly stressed materials is their behavior at a change of temperature, particularly for increasing temperature. These changes in temperature are crucial for some components in automotive industry or aerospace like telescope mirrors or satellite antennas that lead to undesired deformation. [YGT14][GIL10] As a result of these thermal deformations that mostly lead to an expansion the parts or complete components malfunction and thus failures happen and jeopardize the machine, process or even people. This issue of the undesired expansion of components is one of the major problems this thesis deals with.

The other main problem refers to the hardware, the 3D-printer, that is used to manufacture the samples for the thermal expansion tests. Dr. Zheng's Research group at Virginia Tech (VT) in Blacksburg has several home-made printers in use. One of these printers is the multi-material printer that uses mask projection microstereolithography to manufacture structures that consist of two materials. Due to the fact that this multi-material printer is a prototype and was built from scratch one year ago, the printer is not fully developed yet. Although the process of additive manufacturing, especially 3D-printing, is known as an efficient and sustainable method of producing complex structures the multi-material printer is wasting resources and has room for improvement in this area. [MS16][DZ17] Currently the need of resources and thus the overall efficiency is not adequate to consider this machine as sustainable because resins and ethanol are used in quantities above the ordinary. Besides the lack of efficiency, the multi-material printer shows other major problems - availability and reliability. Even though a prototype is not supposed to produce a high number of samples or work several shifts over days and weeks it still has to have a certain availability. [BM15] The large off time of the multi-material printer and the accompanying hours for repairs hinder the production of even a small-series of samples and slow down the progress in research.

These issues of the undesired thermal expansion of structures and the not fully developed prototype of the multi-material printer lead to the following research goals.

1.2 Motivation and Research Objectives

The research objectives of this master's thesis are derived from the above listed issues. To encounter and deal with this unintentional behavior of expansion under thermal load the tunability of the coefficient of thermal expansion offers a smart opportunity. By combining components of high and low CTE material within a lattice the characteristics of this structure change and open a wide range regarding the deformation under thermal load especially towards a negative volumetric CTE. [XP16]

For this reason, the first objective is to explain the theoretical background behind the idea of the tunability of the CTE towards the negative direction that is picked up by Xu and Pasini. [XP16] In this way the possibility of a negative volumetric coefficient of thermal expansion is demonstrated by deriving the analytic equations for a 1st and 2nd order octet-truss unit cell (UC).

After presenting the opportunities that are given by using a structure with a negative volumetric CTE to solve the problem of undesired thermal expansion, the next step is to figure out appropriate components for building up a multi-material structure to achieve this goal and verify the analytic predictions. Therefore, the priority is to investigate the polymers that serve as the base material of the lattices regarding their own individual CTE by conducting heating tests. This is necessary because the base materials determine the range of the volumetric CTE of the structure. The next step is to build up and print 1st and 2nd order octet-truss unit cells of suitable base materials to conduct the heating tests with complete structures to see if the experimental results match the theory. In case of a deviation the aim is to figure out why the results differ.

Another goal is to find different unit cells that have a negative volumetric CTE, which can enable an even larger shrinkage than the octet-truss. Therefore, existing single-material unit cells are evaluated to consider their potential for achieving a negative volumetric CTE. Two promising unit cells are picked and modified to show in simulation their behavior under thermal load. The purpose is to simulate a 2nd order structure of the unit cell with the higher potential regarding its negative volumetric CTE.

A different, but not less challenging objective of this thesis is the improvement of the prototype of the multi-material printer. As mentioned in the previous chapter, the two main problems of this printer are the availability and efficiency. This is why the focus is on analyzing the current state of the multi-material to detect its weak points and to get starting points for improvements. Moreover, it is planned to use strategic approaches for developing solutions to the issues. The final step of this process and also of this thesis is the implementation of the developed solutions and thereby the creation of an improved and thus more reliable and efficient prototype of a multi-material printer.

By stating the motivation and research objectives of this thesis it is pointed out that on the one side the focus is on the demonstration of the chances and opportunities of multi-material structures with a negative volumetric CTE. On the other side, it is the goal to improve the hardware of the multi-material printer to achieve a stable running process and also a higher efficiency regarding the need of resources like resins and ethanol.

1.3 Methodology

For the fulfillment of the research objectives, a clear structured approach is necessary and is explained in this section.

At the beginning of this work, the chapter on the state of the art provides the knowledge needed to understand the subject and the working methods. It starts with an introduction of the additive manufacturing technologies followed by an explanation of the process of mask projection microstereolithography used to manufacture the samples. Additionally, characteristics of polymers are explained because polymers serve as the base materials of this research project.

Following the state of the art, the theoretical background is explained to give an understanding of how negative thermal deformation works and thus how to achieve a negative volumetric CTE for the octet-truss. This chapter is fundamental for the subsequent heating tests and delivers analytic predictions of the CTEs that are used as reference values to compare the experimental results to the theory.

After offering and demonstrating the theory of this first research part, the setup used for conducting the experimental part is explained. The equipment like the multi-material printer and the Ember 3D printer that are manufacturing the samples as well as the hot plate and the INSTRON heating chamber that are used to conduct the heating tests are described. Moreover, the MATLAB program that serves as the measurement software is exemplified including the camera that is taking the required pictures. Also, the tested polymers are described before mentioning the test procedure for the thermal expansion test on the hot plate and in the INSTRON heating chamber.

Then starts the investigation of the coefficient of thermal expansion. First the CTEs of the base material serving polymers are determined by conducting the thermal expansion tests on the hot plate and computing the CTE values through MATLAB software. Evaluating the results of the base materials enables the choice of appropriate components among these polymers for further research.

Building up multi-material structures is the next step. Starting with 1st order unit cells the heating tests are now conducted in the INSTRON heating chamber with the same measurement methods as before. The results of the examination of the 1st order samples are compared with the analytical predictions to see if there is any deviation or if the results perfectly match. Afterwards, investigations of 2nd order unit cells are conducted and analyzed the same way as the 1st order samples were. These results are also compared with the theory before a final conclusion about the thermal expansion tests is stated.

To accomplish the next research goal different single-material unit cells other than the octet-truss are reviewed. Consideration is given as to whether or not they are suitable for a multi-material lattice to achieve a negative volumetric CTE. The two most promising unit cells are modified and assigned with two components to simulate their behavior under thermal load. The one with the higher potential regarding the negative CTE is further investigated as a 2nd order structure to see if the potential is as high or even higher than the octet-truss.

In the end, the multi-material printer is improved by the following approaches. The current state of the multi-material is analyzed and noted down to find starting points and room for improvements. Then methods of product development like the list of requirements, morphological matrix, etc. are used to find the best solution for the new multi-material printer. After a rating, the best concept is picked, the changes are implemented and the improved system is built up.

This methodology of how to approach and solve the research objectives is summarized and illustrated in the flow chart of Figure 1.

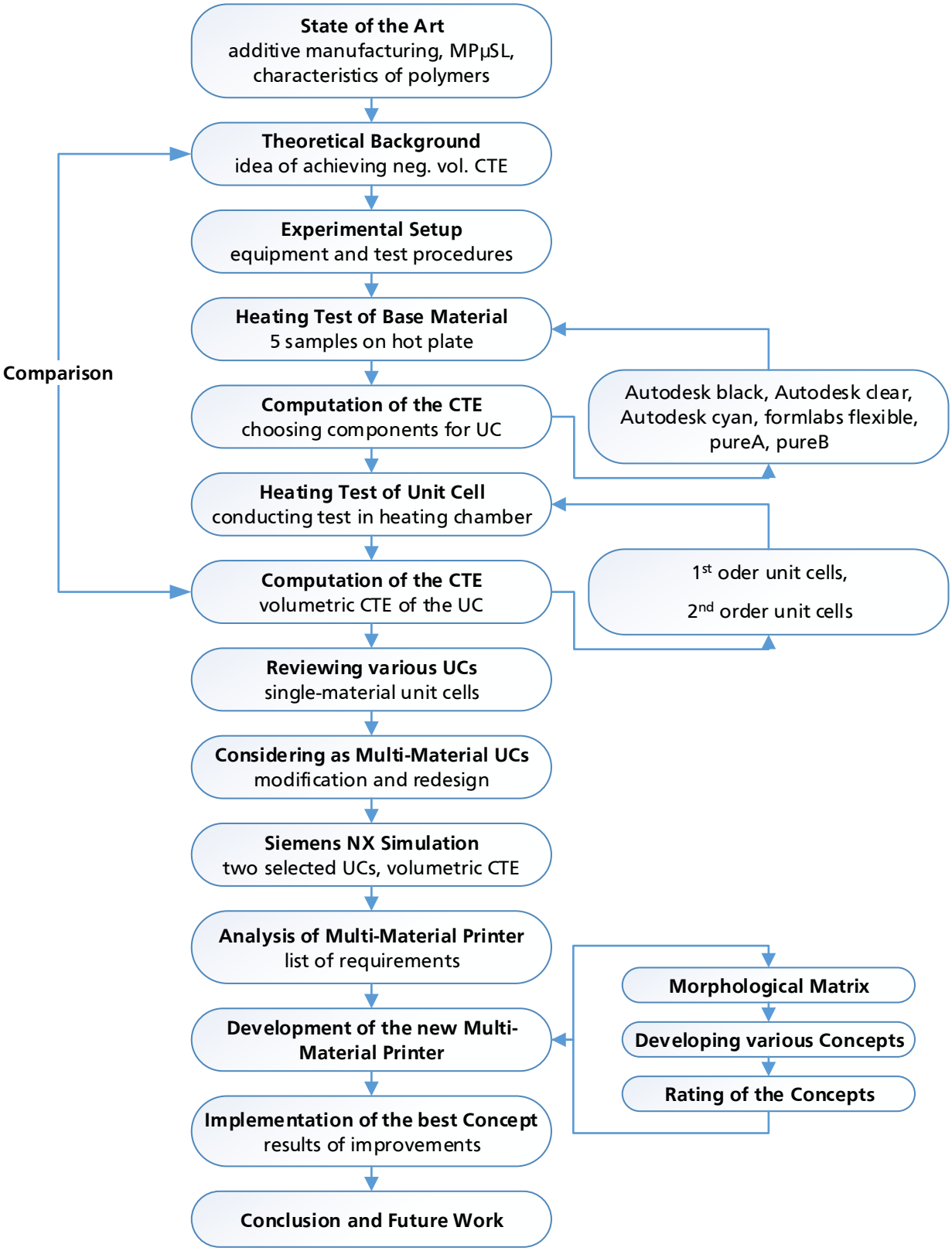

Figure 1: Flow chart of methodology

2 State of the Art

The following chapter describes the process of additive manufacturing in general before referring to a sub-category - the mask projection microstereolithography. Moreover, characteristics of polymers like the coefficient of thermal expansion, the glass transition temperature and the Young's modulus are described.

2.1 Additive Manufacturing

The technology of additive manufacturing is capable of fabricating complex 3D components by building the object layer-wise. This technique increases the standard of complexity in shape compared to subtractive processes like milling or turning. By using the computer aided design (CAD) model of the object that is converted into a stereolithography (STL) file the process of creating prototypes is faster than the conventional methods and does not require special tools for the manufacturing process. Applications of additive manufacturing technologies range from prototypes (Rapid Prototyping), over small-scale series production (Rapid Manufacturing), to tooling applications (Rapid Tooling). With the enhancement of the additive manufacturing processes they are now widely used in many branches of industry like automotive or for medical applications. [SH14][YHB17] On the one side the procedures of additive manufacturing depend on the feedstock and on the other side they depend on the technologies that are used. Figure 2 illustrates the diversity of additive manufacturing methods.

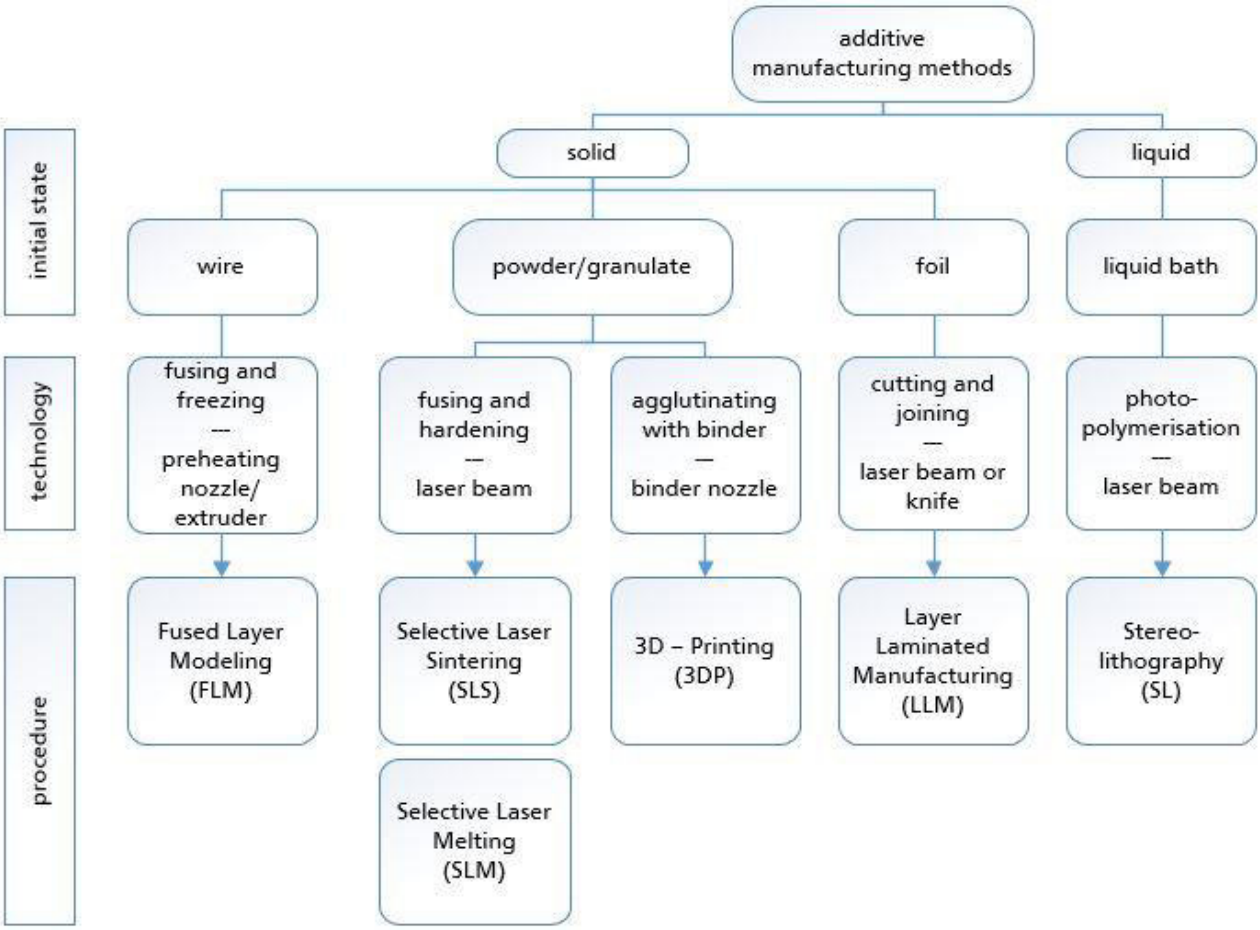

Figure 2: Survey of additive manufacturing methods [AND15]

The procedure of fused layer modeling (FLM) uses a solid wire of acrylonitrile-butadiene-styrene (ABS) or polylactide (PLA) and a preheating nozzle or extruder to fuse the feedstock and print layer by layer in this way. Also, this time a solid powder or granulate feedstock is used instead of a wire for selective laser sintering (SLS) and selective laser melting (SLM). Both methods melt their feedstock – polyamide for SLS and metal alloys for SLM – with a laser beam. With a binder nozzle, the 3D-printing (3DP) procedure is agglutinating cement-ceramic-powder and thus printing the object. The last additive manufacturing method using a solid feedstock is the process of layer laminated manufacturing (LLM). The base material for this procedure is a foil that is needed to print a layer and cut by either a laser beam or a knife. Unlike the previous methods, stereolithography (SL) uses a liquid bath of photopolymers and the technology of photopolymerization activated by a laser beam for the printing process. [AND15]

By starting the manufacturing process straight from the CAD and respective STL file the additive manufacturing methods have several advantages compared to traditional methods. The benefits and also the challenges of these methods are described in the following section before explaining specifically the process of mask projection microstereolithography.

2.1.1 Advantages and Disadvantages of Additive Manufacturing

As already indicated the freedom in design increases dramatically by using additive manufacturing, which is the biggest advantage of this method. It enables the fabrication of complex structures like hollow shapes or objects of different material. Moreover, the process is capable of starting right after finishing the design because no other tooling is required. This is a huge benefit for rapid prototyping. Due to the fact that no special tooling is required, changes in design are very easily feasible. Additionally, this kind of manufacturing saves material because it does not turn or mill the component from a solid block and thus creates less waste than traditional machining. [BGB15]

One of the downsides of additive manufacturing is that the surface often requires post-processing to achieve the desired surface quality. Furthermore, the build rate for fabricating large-series is slower than the one for traditional machining. The third drawback is the high investment that a production with high-end printing requires to manufacture the same quality as turning or milling. These advantages and disadvantages of additive manufacturing are summarized and listed in Table 1. [BGB15]

Advantages	Disadvantages
+ freedom of design and complexity	- post-processing required
+ no tooling required	- not appropriate for large-series
+ prototyping, quick change in design	- high investment
+ save of material	

Table 1: Advantages and disadvantages of additive manufacturing

2.1.2 Mask Projection Microstereolithography

The process of mask projection microstereolithography is a version of stereolithography and a principal part of this work. Hence, the process is described in detail and covers the essential parts like the orientation of the projection, the digital micromirror device, and the process of photopolymerization and recoating.

The process of mask projection microstereolithography uses a light emitting diode (LED) as an ultraviolet (UV) light source instead of a UV laser beam and a dynamic pattern generator (dynamic mask) like the digital micromirror device (DMD). The purple lines in Figure 3 illustrate the path of the light. At first the light passes through several optics like lenses, filters, and mirrors so that the light strikes parallel to the surface of the dynamic mask. By the DMD the light is digitally patterned and projected as the cross-section image through a single or a set of optical lenses to resize the image. Ultimately, the image is focused on the surface of the photopolymer resin and cures the resin by initiating the crosslink through photopolymerization. This effect is visualized by the red layers inside the photopolymer container. After the first layer has been cured, the linear actuator moves the platform downwards so that the previous layer gets recoated. Then the platform is lifted to the surface again so that the subsequent layer can be hardened. [BBR01][CWL09][LAM14] This printing process, where the resin is cured from above is also called top-down configuration. The setup of this method is shown in Figure 3.

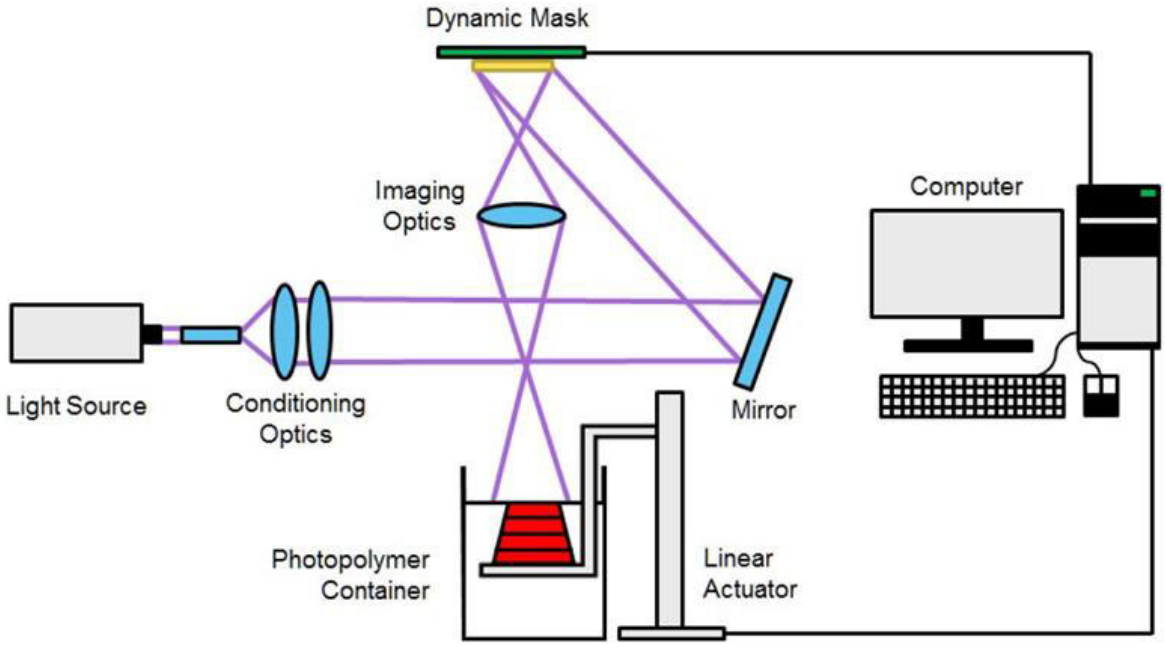

Figure 3: Process of mask projection microstereolithography [LAM14]

The process of MPμSL is controlled by a computer which regulates both, the dynamic mask and the linear actuator. At the beginning, a CAD model is converted into a STL file and sliced according to the layer thickness, which is around 40 μm or even lower due to limitations on controlling the UV penetration for a multi-material printing process. [CMW10] This is followed by exporting the images of each layer as Bitmap images (BMP), and arranging the images in the correct order, which is particularly important for multi-material structures. Then each layer is assigned a certain step for the height – up one layer thickness or remain same height - and exposure time in the rows and columns of the computerized numerical control (CNC) code. [HCL08] Multi-material structures additionally require washing cycles for every change of material.

Besides the projection from above it is also possible to cure the resin from below and thus change the projection direction. These two projection methods are compared in the following section before explaining the main parts of MPμSL, the digital micromirror device, the photopolymerization, and the process of recoating.

2.1.2.1 Orientation of Projection Direction

For the projection of the images during the printing process there are basically two different methods of how to cure the resin. Either the light hardens the polymer from the top or from the bottom. The process in Figure 4 (a) with the projection direction from above is curing the first layer straight at the surface and onto the platform. Then the platform is lowered so that new resin floats on top of the previous printed layer and the UV light is able to cure the next layer. The benefits of printing from above are that a lot of empirical values already exist and that the sample is not attached to a transparent window, usually a polydimethylsiloxane (PDMS) window. On the downside, it should be mentioned that there is a slower printing velocity in comparison to the printing method from below because there is a wait time until the surface is even again after lowering the platform. Also, the method is limited by the depth of the resin vat because the resin has to surround the entire object and depending on the resin vat a high amount of resin is also needed. [LAM14]

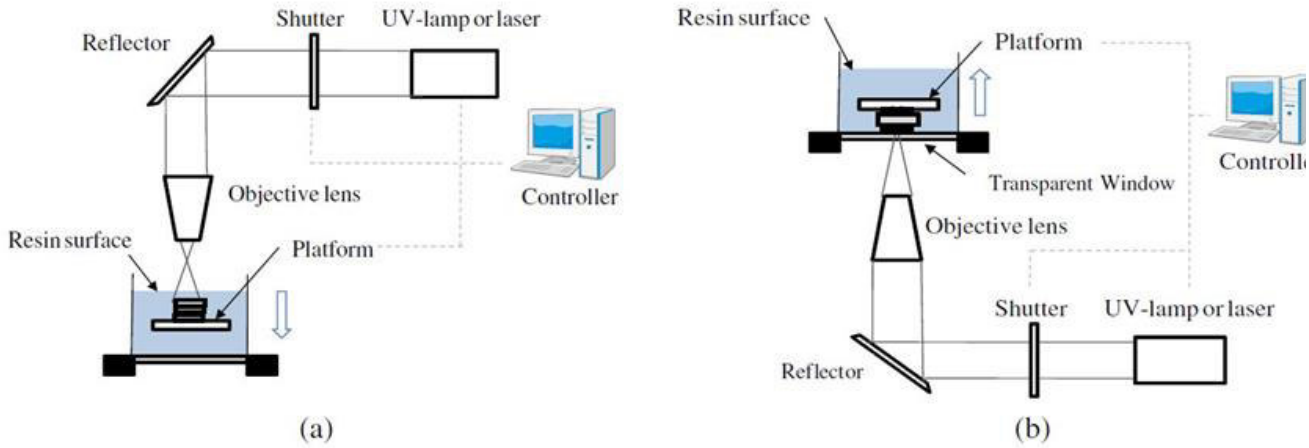

Figure 4: Printing from above (a), printing from below (b) [PHL11]

The process with the projection from below, also called bottom-up configuration, which can be seen in Figure 4 (b) works in a similar way as the printing from above process. Both methods have in common that they cure the layers with UV light and thus building the object on a platform. But the difference between these printing processes is that at the method of printing from below the UV light cures the layers through a transparent PDMS window from the bottom of the resin vat. This means that for the recoating the sample gets lifted and thus the resin has to cover only the surface of the PDMS window and not the whole sample as it is the case for the printing from above method. This save of resin is besides the biggest difference also the greatest advantage of the bottom-up configuration. Moreover, the sample size is not limited to the size of the resin vat as it is for the top-down configuration. Also, the wait time for the recoating is avoided in this way because as soon as the sample gets lifted, resin floats underneath and covers the PDMS window so there is never an uneven surface at the bottom of the resin vat. Whereas there are many advantages of this method there is one large disadvantage – the adhesion of the sample to the transparent window. By curing the resin from below it adheres to both the platform and the bottom of the vat. As a consequence, forces are necessary to release the adhesion on the bottom side to go on with the printing process. In this case, tiny features may possibly get damaged, which lowers the quality of this approach vastly. [LAM14]

In Table 2 the advantages and disadvantages of both approaches are summarized.

Printing from above:	Printing from below:
+ many empirical values	+ faster than printing from above
+ not attached to PDMS window	+ less photopolymer required
- slower than printing from below	+ technically not limited in the height
- limited by the depth of the resin vat	- adhesion to the PDMS window
- high amount of resin needed	

Table 2: Advantages and disadvantages of the printing processes from above and below

2.1.2.2 Digital Micromirror Device

The digital micromirror device plays a crucial part in the process of mask projection microstereolithography because it creates the pattern for the layers that are printed. The DMD made by Texas Instruments contains an array of ~786,000 micromirrors (1024 x 768). Every micromirror has a dimension of 13.68 μm on each side and is activated by electrostatic forces to be independently tiltable $\pm 12°$ to produce the cross-section image. The bundle of light at the angle of $+12°$ creates the favored pattern whereas the micromirrors in the -12° position reflect the light to a mockup or light absorber which is leading to black spots on the resin surface. Figure 5 illustrates the path of the UV light bundle and shows that the projection lens collimates the UV light before curing the resin. This setup ensures an accurate exposure, resolution, and adjusted layer thickness. [BÁR11][CWL09] [LMS06][TS00]

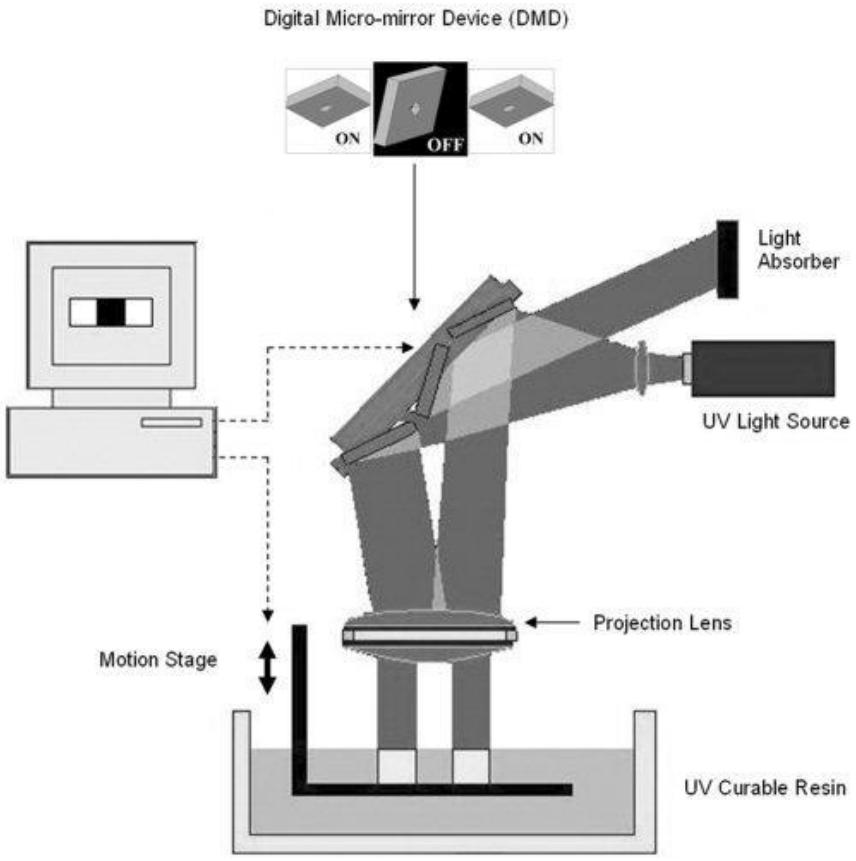

Figure 5: Operating mode of a digital micromirror device [LMS06]

2.1.2.3 Photopolymerization and Recoating

With the UV light being projected on the curable resin, which is a mixture of monomer and photo-initiator, the polymerization process is triggered. Thereby radicals are generated by the photoinitiator absorbing the incident photons. These radicals form larger reactive molecules that grow until two of these reactive molecule chains meet together. The result is a stable polymer chain and the cross-linking of multiple polymer chains leads to a solid phase. This simplified process of photopolymerization is shown in Figure 6. [LIM07][SFW05]

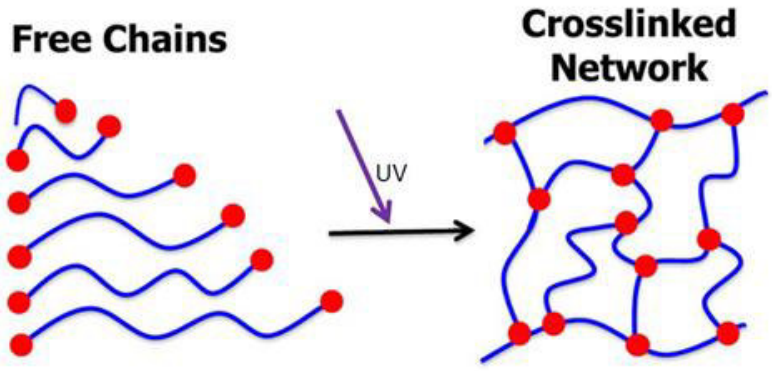

Figure 6: Process of photopolymerization [LAM14]

After a layer has been cured there has to follow a recoating process to print the subsequent layer, which is demonstrated for the top-down configuration. Therefore, the platform is lowered into the vat with the liquid resin so that new liquid resin floats on top of the hardened layer. In the next step, the platform gets lifted up again but stops one layer thickness below the previous position. Before the following image is projected on the surface, a wait time is necessary because the lowering and lifting process undulates the resin and creates an uneven solution surface which is pictured in Figure 7. As soon as the solution surface becomes uniform again the wait time is over and the projecting process starts again. [CWL09][MLC99][PZC12]

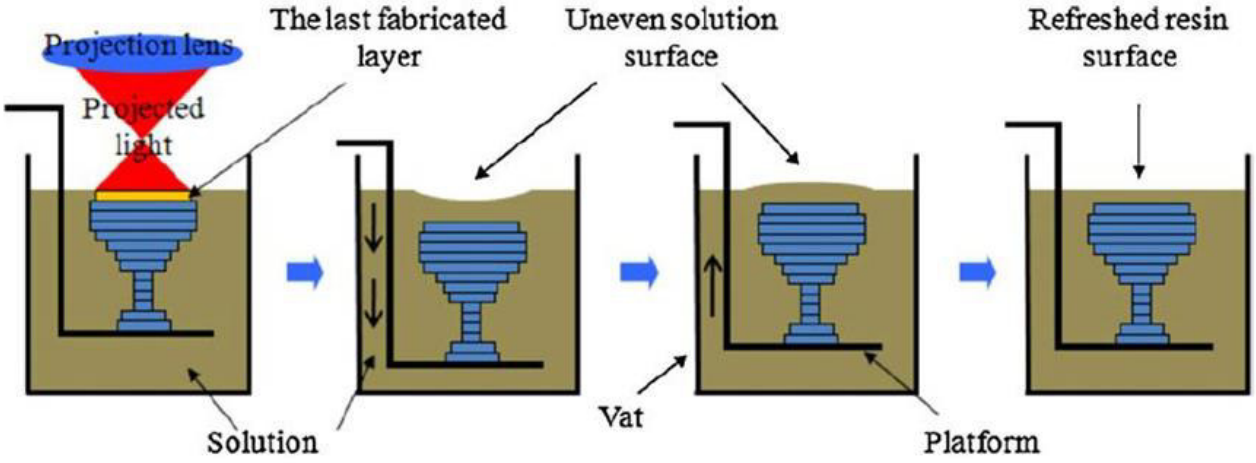

Figure 7: Recoating process of mask projection microstereolithography [CWL09]

2.2 Characteristics of Polymers

Polymers are an alignment of multiply monomers. The process of photopolymerization that triggers this chain reaction is described in section 2.1.2.3. From the chemical point of view the polymerization is shown in the formula for polyethylene:

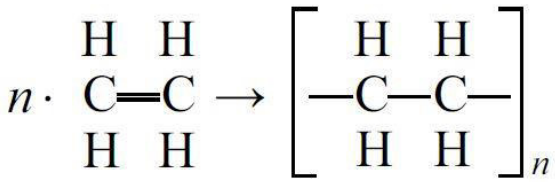

ethylene polyethylene [IS10]

A number of single monomers n of ethylene are connected during the process of polymerization to form the long chain polyethylene. The following subsections will discuss the coefficient of thermal expansion, glass transition temperature and Young's modulus of the polymers.

2.2.1 Coefficient of Thermal Expansion

The coefficient of thermal expansion α describes how much a solid component, in this case a polymer, expands or shrinks under a thermal load and at a constant pressure. [CM14] To get this coefficient α the data about the change in temperature ΔT, the change in length Δl and the initial length l of the sample are required. With the information and the formula

$$\alpha = \frac{1}{\Delta T} * \frac{\Delta l}{l} \qquad \text{[KFG08]}$$

the coefficient of thermal expansion is computed. The CTEs of polymers have a very broad range from for instance 10 x 10^{-6} 1/°C for polyurethane to 250 x 10^{-6} 1/°C for polyethylene. [MW05]

2.2.2 Glass Transition Temperature

An application of the polymer above the glass transition temperature T_G changes its mechanical characteristics. The change is comparable to the transition of a hard ($T < T_G$) to a soft ($T_G > T$) spring. Below T_G the molecular polymer chains are frozen, whereas the polymer chains above the glass transition temperature perform like a soft spring because of the molecular movement. Due to the fact that the polymers have chains of different length, they are not completely homogeneous. This means that when the temperature gets closer to the T_G not all polymer chains turn into a soft state at the same time and thus the characteristics are changing at this point. [KMN14] The transition has also an influence on the coefficient of thermal expansion. Above T_G the CTE of the polymer is significantly higher than below T_G. [STR00]

2.2.3 Young's Modulus

The Young's modulus E is defined as the ratio of stress σ divided by the strain ε. This ratio, also called Hooke's law, is expressed by the following equation:

$$E = \frac{\sigma}{\varepsilon} \qquad \text{[HNK10]}$$

This ratio describes the linear elastic behavior that is reversible and independent of the path. [AE13] To visualize this characteristic Figure 8 shows the graph of the linear elastic area.

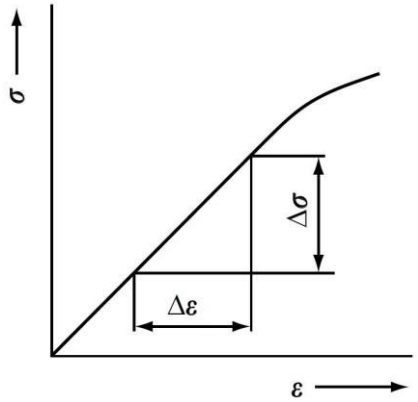

Figure 8: Definition of Young's modulus E = $\Delta\sigma/\Delta\varepsilon$ [BS12]

Values of the Young's modulus for polymers can reach from almost 0 MPa to around 20.000 MPa. [SCH14] With adding particles to the polymers this range can even be increased.

The chapter about the state of the art provides a survey of the different additive manufacturing methods and the advantages and disadvantages of this technology compared to the traditional machining. Moreover, the process of mask projection microstereolithography is elucidated with the two directions of projection, its digital micromirror device, and the photopolymerization and recoating process. In the end characteristics like the coefficient of thermal expansion of the polymers are described.

In the following chapter the theoretical background for achieving a negative volumetric CTE of multi-material hierarchical structures is presented.

3 Theoretical Background

The first main objective of this thesis is dealing with achieving a negative thermal expansion of unit cells. For this reason, the first step is to highlight the theory behind this idea of getting structures with a negative volumetric CTE. As a typical unit cell, the octet-truss is ideal because lightweight structures like the octet-truss are known for their advantage of having a high stiffness at low density. [ZLW14] In addition, the structure allows a combination of different materials within the lattice to adjust the coefficient of thermal expansion of the structure.

This opportunity of adjusting the deformation of an octet lattice at a certain thermal load is indicated and shown in simulations by Xu and Pasini. [XP16] By operating with an octet-truss it is demonstrated how the idea of the tunable CTE works. The basic component of the octet-truss is a tetrahedron which consists of six struts and is defined by the skew angle θ, as illustrated in Figure 9 (a). Besides the tetrahedron, the octet-truss, which is also called a 1st order unit cell is assembled of eight tetrahedrons and shown in Figure 9 (b). The next hierarchical step is a 2nd order unit cell, which consists of bars aligned with 1st order unit cells and is pictured in Figure 9 (c).

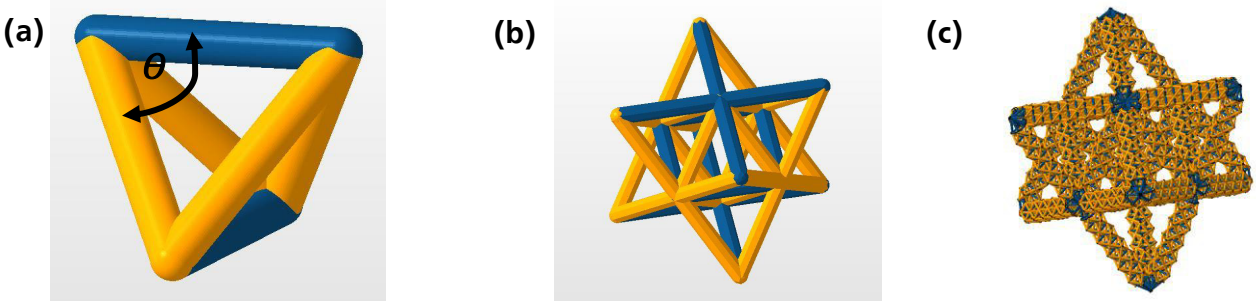

Figure 9: (a) Tetrahedron, (b) 1st order unit cell, (c) 2nd order unit cell

The blue struts (for illustration purposes) of the tetrahedron at the bottom and at the top are assigned to a material with a high CTE, whereas the yellow struts have the characteristic of a low CTE material. This distinction has to be made to achieve the negative thermal expansion. Heating up the tetrahedron causes a higher expansion of the blue than the yellow struts. In this case the height h of the tetrahedron – distance between top and bottom strut – decreases. Displayed in Figure 10, the thermal influence and thus the expansion of the individual struts of the tetrahedron is strongly amplified, where h_0 points out the height of the tetrahedron before and h_1 the height after the thermal load is applied.

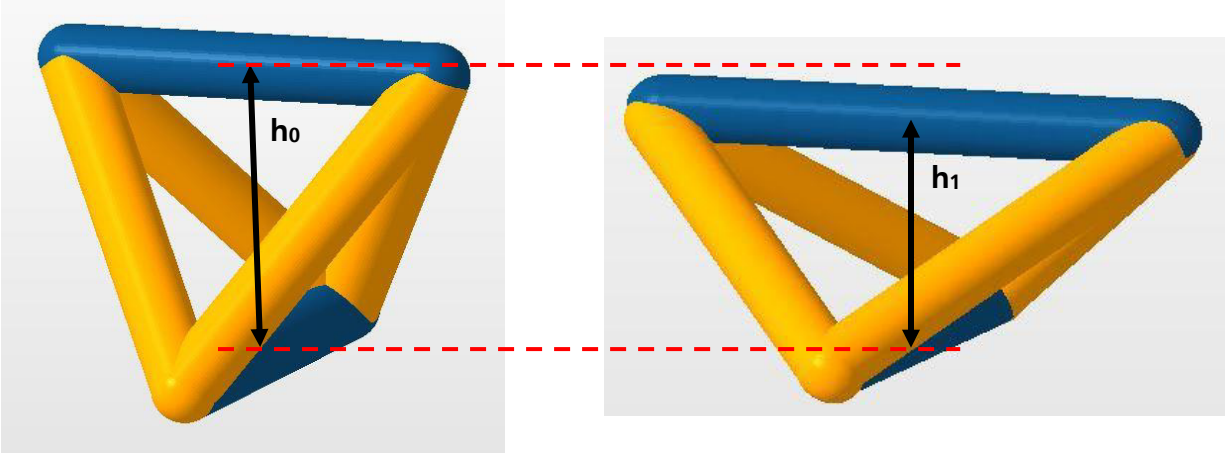

Figure 10: Thermal influence on the height of the tetrahedron with materials of different CTE

With a reduction of the height of the tetrahedron the height of the octet-truss also decreases. This deformation is affected by the skew angle θ, temperature difference ΔT, the CTE of the blue material α_1 which is representing the high CTE, and the CTE of the yellow material α_2 that represents the low CTE. The CTEs α in x-, y-, and z-direction of a 1st order unit cell are expressed below by the following analytic equations:

$$\alpha_{x,1st} = \alpha_{y,1st} = \alpha_1$$

$$\alpha_{z,1st} = \frac{1}{\Delta T} * \frac{\sqrt{(1+\alpha_2 \Delta T)^2 - 2cos^2\theta(1+\alpha_1 \Delta T)^2} - \sqrt{1-2cos^2\theta}}{\sqrt{1-2cos^2\theta}}$$

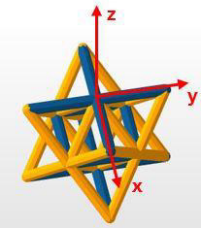

The image on the right-hand side illustrates the directions within the 1st order unit cell and thus visualizes that the coefficients of thermal expansion in x- and y-direction - $\alpha_{x,1st}$ and $\alpha_{y,1st}$ - equal the CTE α_1 where the CTE in z-direction, $\alpha_{z,1st}$, is dependent on the CTE of both materials and especially the skew angle θ. In chapter 10.1 this equation is derived in detail.

For the 2nd order unit cell the struts are assembled of 1st order unit cells and called bars. The alignment is along the z-axis and illustrated with five 1st order unit cells in Figure 11.

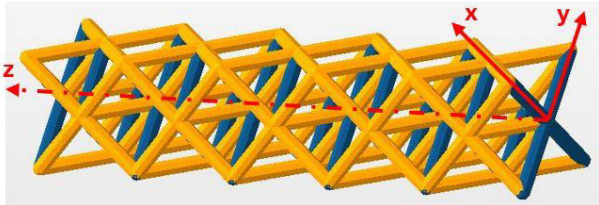

Figure 11: Bar of 2nd order unit cell 60° aligned of five 1st order unit cells 60°

The 2nd order unit cell consists of bars that all have the same CTE, the one of the 1st order unit cell in z-direction. Hence, the analytic equations for the higher order sample are derived as followed:

$$\alpha_{x,2nd} = \alpha_{y,2nd} = \alpha_{z,1st}$$

$$\alpha_{z,2nd} = \frac{1}{\Delta T} * \frac{\sqrt{\left(1+\alpha_{z,1st}\Delta T\right)^2 - 2cos^2\theta\left(1+\alpha_{z,1st}\Delta T\right)^2} - \sqrt{1-2cos^2\theta}}{\sqrt{1-2cos^2\theta}}$$

$$= \frac{1}{\Delta T} * \frac{\sqrt{\left(1+\alpha_{z,1st}\Delta T\right)^2(1-2cos^2\theta)} - \sqrt{1-2cos^2\theta}}{\sqrt{1-2cos^2\theta}}$$

$$= \frac{1}{\Delta T} * \frac{\left[\left(1+\alpha_{z,1st}\Delta T\right)-1\right] * \sqrt{1-2cos^2\theta}}{\sqrt{1-2cos^2\theta}}$$

$$\alpha_{z,2nd} = \alpha_{z,1st}$$

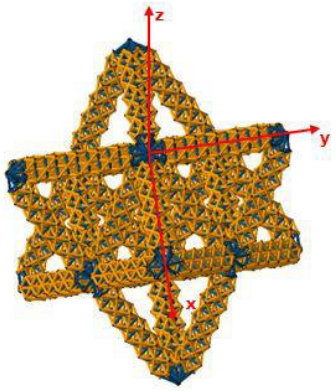

These equations state that the 2nd order unit cell of an octet-truss shrinks uniformly in all directions with the CTE $\alpha_{z,1st}$. With these results for both unit cells the volumetric CTE is computed by looking at the change in volume.

The two graphs below point out the impact of the different CTE ratios at a skew angle of 60° as well as at 55°. The CTE ratios of 6:1, 2:1, and 1:1 are used to cover a certain range and to see the impact of a steep increase in the ratio. Figure 12 shows how both criteria are changing the volumetric CTE of the 1st and 2nd order unit cell. The temperature difference ΔT for this computation is 128°C which is calculated from heating up the sample from 22°C room temperature to 150°C.

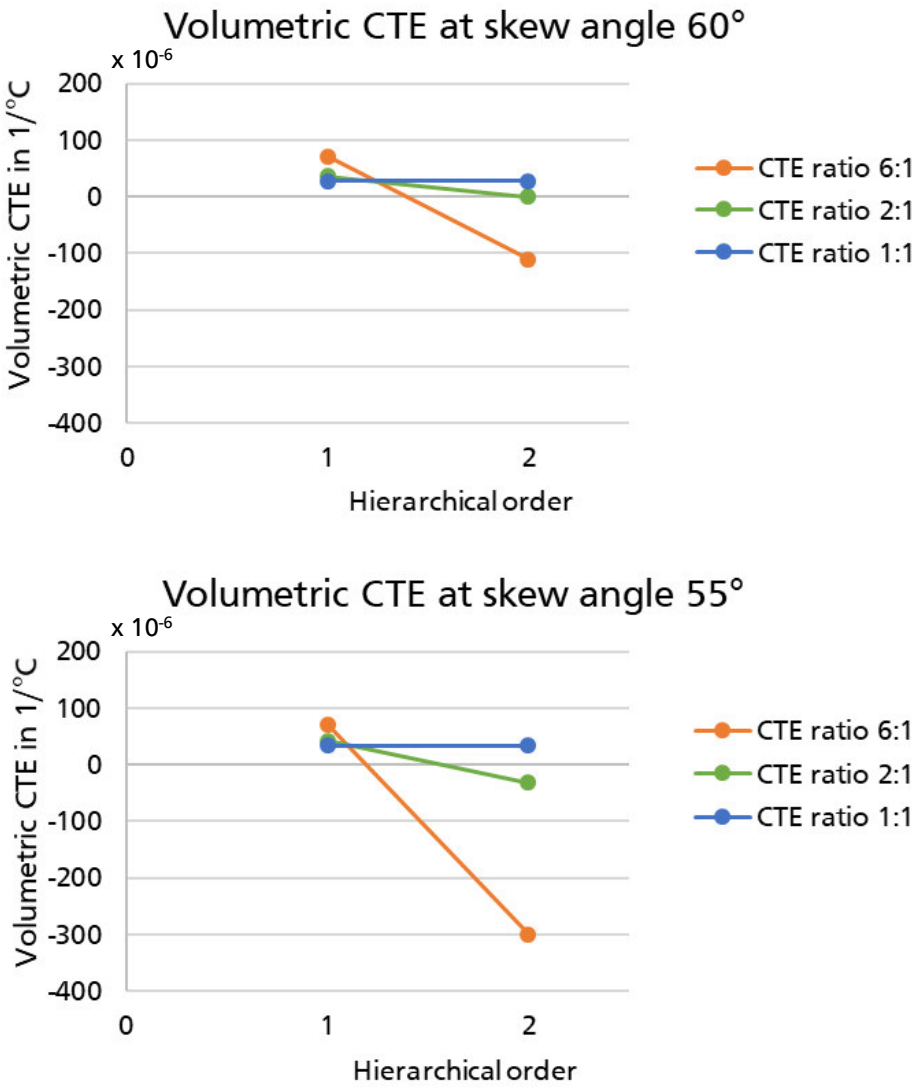

Figure 12: Impact of the skew angle θ and the CTE ratio on the volumetric CTE

It can be seen that for both skew angles the CTE ratio of 6:1 and hierarchical order of one has the highest value and decreases dramatically to the lowest volumetric CTE at the hierarchical order of two. The values start for both angles at around 71 x 10^{-6} 1/°C and end at -109.94 x 10^{-6} 1/°C for the skew angle of 60° and at -299.38 x 10^{-6} 1/°C at 55°. A similar decline happens for the ratio of 2:1, where it ends up at zero for the skew angle of 60° and at -31.70 x 10^{-6} 1/°C at the angle of 55°. In contrast to the other ratios, the 1:1 ratio remains stable as expected at 27.09 x 10^{-6} 1/°C for 60° and at 34.08 x 10^{-6} 1/°C for 55° because it behaves like a single-material unit cell. The reason why all 1st order unit cells have a positive volumetric CTE is that the negative thermal expansion in z-direction is compensated by the expansion in the x- and y-direction. However, for the 2nd order unit, where only $\alpha_{z,1st}$ matters, a negative volumetric CTE is achievable.

To put it in a nutshell, the influence of the skew angle θ and the CTE ratio on the volumetric CTE is clearly pointed out in Figure 12. A high CTE ratio between the two materials enables a negative volumetric CTE at a hierarchical order of two and the reduction of the skew angle from 60° to 55° enforces this effect strongly. Thus, a CTE ratio of 6:1 and a skew angle of 55° enable a negative volumetric CTE of roughly -300 x 10^{-6} 1/°C for a 2nd order unit cell.

This analytic prediction about the thermal deformation of octet lattices of 1st and 2nd order structures is investigated in the following heating tests after explaining the experimental setup.

4 Experimental Setup

Conducting the thermal expansion tests and the measurements to determine the CTE of the base material and complete structures requires special equipment and certain test procedures. This chapter provides an overview about the equipment that is used for this research including multi-material printer, Autodesk Ember 3D printer, INSTRON heating chamber, hot plate, the measurement method, and the polymers that are used. Moreover, the test procedure on the hot plate as well as the thermal expansion test in the INSTRON heating chamber are explained.

4.1 Equipment

The equipment is the base of every test procedure. Thus, the devices and components that are used for the thermal expansion tests are described in the following sections beginning with the prototype of the multi-material printer.

4.1.1 Multi-Material Printer

The 3D-printer that is used for manufacturing the samples of unit cells is a home-made multi-material printer (Large Area, Multi-Material Additive Manufacturing System using integrated resin exchange, U.S. Provisional Patent Application No.: 62/313,954, 2016) and is shown in Figure 13.

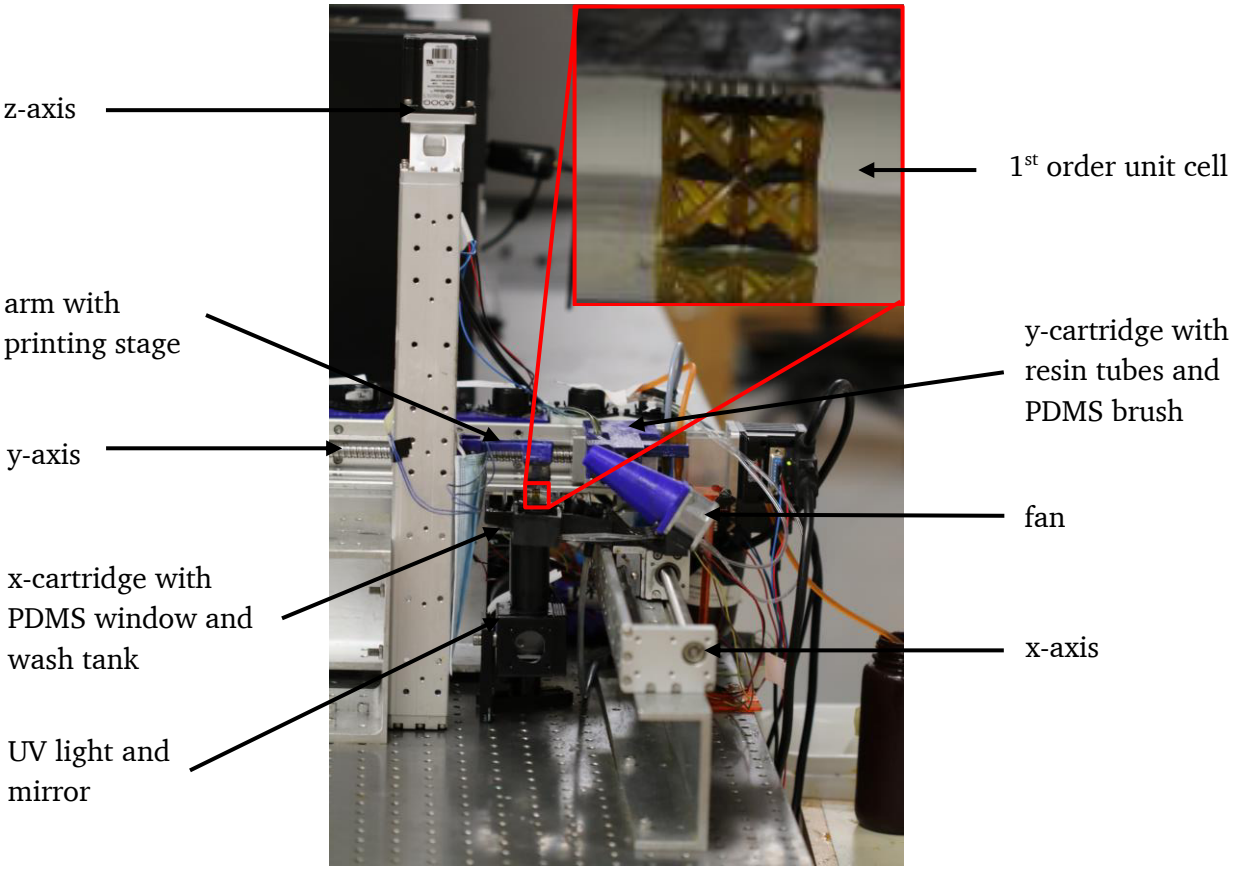

Figure 13: Multi-material printer including sample of 1st order unit cell 60°

It is built up on three axes – x, y, and z. The x-axis holds the x-cartridge with the fan, washing chamber, and the PDMS window on it. The y-axis supports the y-cartridge which holds the print head, various

material feedstock, as well as the PDMS brush. The z-axis guides the elevator with the printing stage. For projection of the printing image a DMD is used and the system works with the printing from below method. The printing area of the multi-material printer is designed for 20 x 15 mm with a resolution of 1024 x 768 pixels where the size of one pixel is 19.5 μm. Theoretically the height of a printing is limited by the height of the actuator of the elevator in the z-axis, but technically it is restricted by the strength of the support material that has to carry the load of the sample and be able to resist the wind power during each drying cycle of the entire printing process. For the minimum layer thickness, the limit is 10 μm and the upper limit is dependent on traits of the resin like light absorption. The exposure time for the utilized polymers is 15 s.

The printer is controlled through Arduino and LabVIEW software. The LabVIEW program needs as input the sliced images of a CAD model in .BMP format as well as a CNC code to assign each layer the right polymer and exposure time respectively the washing cycle. In Table 3 an overview of the technical specifications of the multi-material printer is provided.

Multi-material printer	
Printing area	20 x 15 mm
Min. layer thickness	10 μm
Usual exposure time	15 s
DMD resolution	1024 x 768
Pixel size	19.5 μm

Table 3: Technical specifications of the multi-material printer

4.1.2 Autodesk Ember 3D printer

An Autodesk Ember 3D printer, illustrated in Figure 14, is used for manufacturing single-material samples like the ones for the determination of the base material.

Figure 14: Ember 3D printer by Autodesk [www0]

This system operates with the printing from below technique and has a maximum build volume (x, y, z) of 64 x 40 x 134 mm. Its xy-resolution is 50 μm and in z-direction – layer thickness – is between 10 μm and 100 μm. A maximum printing speed of 18 mm/hour can be achieved at a layer thickness of 25 μm.

Suitable for this system are acrylate photosensitive resins by Autodesk and also self-provided resins. These technical specifications are listed in Table 4 below. [www0]

Autodesk Ember 3D printer	
Build volume (x, y, z)	64 x 40 x 134 mm
xy-resolution	50 μm
z-resolution (layer thickness)	10 – 100 μm
Max. speed	18 mm/h

Table 4: Technical specifications of Autodesk Ember 3D printer [www0]

4.1.3 Heating chamber

An INSTRON environmental heating chamber, seen in Figure 15, is used for heating up the samples of the unit cells under equal environmental conditions. The temperature range of the chamber can be set from -100°C up to +350°C. For heating up the chamber the method of forced convection is used with a fan on the backside of the chamber. [www1]

Figure 15: INSTRON heating chamber

4.1.4 Hot Plate

For the thermal expansion tests of the base materials a hot plate by VWR is used. The temperature range for this device with a ceramic plate is from 5°C above ambient room temperature to 500°C. Its temperature stability is ±1%. The hot plate is illustrated in Figure 16 below. [www2]

Figure 16: VWR hot plate [www3]

4.1.5 Pixel Measurement Method

Measuring the thermal expansion and computing the CTE value of the base material and complete structures like the unit cells requires high precision and reliability. For this reason, pictures from the initial state and the final state are taken with a CANON EOS 7D Mark II with an effective pixel number of 20.2 MP and compared with the help of MATLAB code. This MATLAB tool uses the pixel measurement method. The first step is to select the edges, corners, and center of the initial state. Then the same spots are selected in the picture of the final state. An example of picking the red points of measurement is shown at a 1st order unit cell 60° in Figure 17.

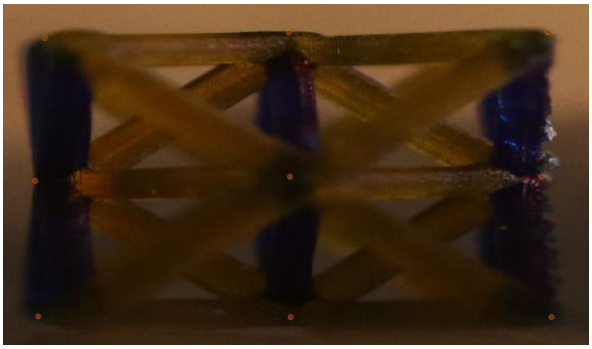

Figure 17: Method of measurement of a 1st order unit cell 60°

The software subsequently provides the coordinates of the points so that the vector length l is computed by:

$$l = \sqrt{(x_2 - x_1)^2 + (y_2 - y_1)^2}$$

By knowing the length of the initial and the final state as well as the temperature difference ΔT the CTE α is computable.

4.1.6 Tested Polymers

The six polymers that are used for the printing tests include three acrylate photosensitive resins by Autodesk called Autodesk black, Autodesk clear, and Autodesk cyan as well as the flexible resin from formlabs and two self-provided resins pureA and pureB. PureA is composed of 97.95% bisphenol A ethoxylate dimethacrylate, 0.05% of sudan I as a photoblocker and 2% of phenylbis(2,4,6-trimethylbenzoyl)phosphine oxide as a photoinitiator. This relation of initiator and blocker is required for the printing process. PureB, consists of the same amount of sudan I and phenylbis(2,4,6-trimethylbenzoyl)phosphine but differs in its main component - trimethylolpropane triacrylate. A characteristic of these polymers, the Young's modulus, is provided by previous tests and listed in Table 5.

Young's modulus	
Autodesk black	550 MPa
Autodesk clear	550 MPa
Autodesk cyan	550 MPa
formlabs flexible	10 MPa
pureA	5 MPa
pureB	800 MPa

Table 5: Young's modulus of the tested polymers

4.2 Test Procedure

After individually describing the devices, measurement method, and components that are preconditioned, now the procedures for the thermal expansion tests are presented. First the testing process on the hot plate to determine the CTE of the polymers is described before the thermal expansion test with the INSTRON heating chamber for getting the CTE of the unit cells is explained.

4.2.1 Thermal Expansion Test on the Hot Plate

The determination of the CTE of the base components occurs with the help of the hot plate. Therefore, five samples of each polymer with the dimension of 15 x 2 x 2 mm are printed on the Ember System by Autodesk. Then these samples are put on the ceramic platform of the hot plate at 22°C room temperature and a picture from the top view of this state – the initial state – is taken by a high-resolution camera. After setting up the samples and taking the picture, the temperature of the hot plate is set to 150°C and 15 minutes later, after the samples are uniformly heated up, a picture of the final state is taken. In this way, the elongation of the samples is recorded and the change in length is computed with the MATLAB tool. In Figure 18 this test procedure of the thermal expansion test on the hot plate is shown.

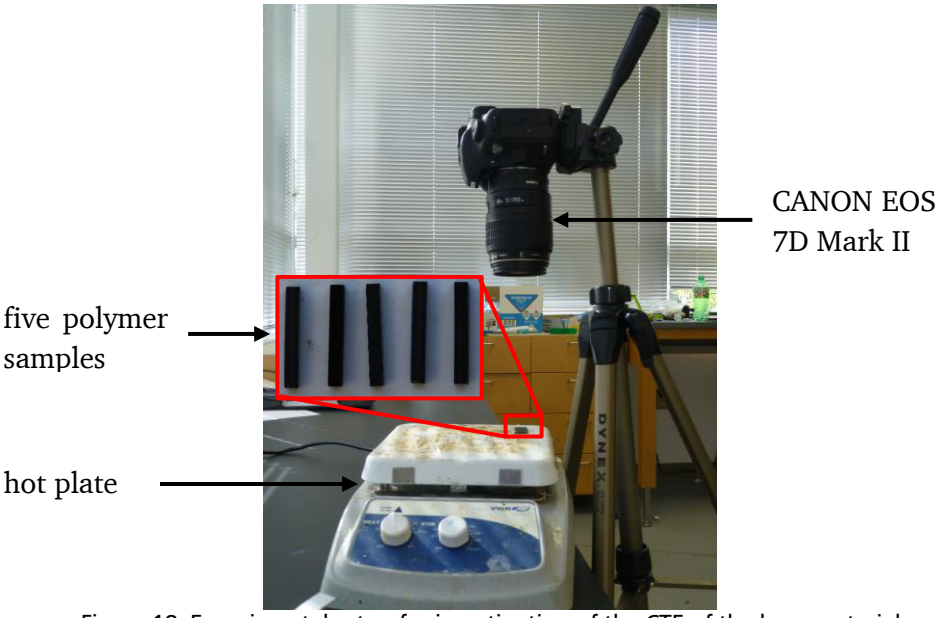

Figure 18: Experimental setup for investigation of the CTE of the base material

After a test for one series of samples is finished, there is a wait time of at least two hours required. This time is necessary so that the hot plate reaches the 22°C room temperature again after switching off the power. Then the test cycle starts again with the next series of polymers.

4.2.2 Thermal Expansion Test in the Heating Chamber

In contrast to the previously described thermal expansion test, the determination of the coefficients of thermal expansion of complete structures like the unit cells requires an environmental heating chamber. The unit cells are built of single struts so there are free spaces within the structure and because of the low thermal conductivity of polymers the hot plate is not an appropriate method to heat up the samples of the unit cells uniformly. [HOR06] The heating chamber on the other hand uses a fan and thus forced convection to meet the requirement of having a constant temperature everywhere around the sample.

Unlike with the hot plate, the conduction of this thermal expansion test starts with a preheating of the heating chamber for three hours. The reason for this is that the stage, on which the sample is put on is a metal platform. This means that by heating up the chamber the metal is also expanding. But for the documentation and video recording a constant environment is necessary so that the temperature inside the chamber has to be 150°C and the expansion of the metal platform has to be finished before putting the sample in. Additionally, a box is set up in the middle of the platform, where the sample is put in to protect the sample from getting moved by the wind caused by the fan. When the preheating is finished the sample with 22°C room temperature is put in the box and a picture of the initial state is taken and a video is started. After 15 minutes, the picture of the final state is taken and the video is stopped. These two pictures serve as the base of the measurements of the thermal expansion whereas the video is used as a method to visualize the deformation of the sample. In Figure 19 the experimental setup is illustrated with a 1st order unit cell 60°.

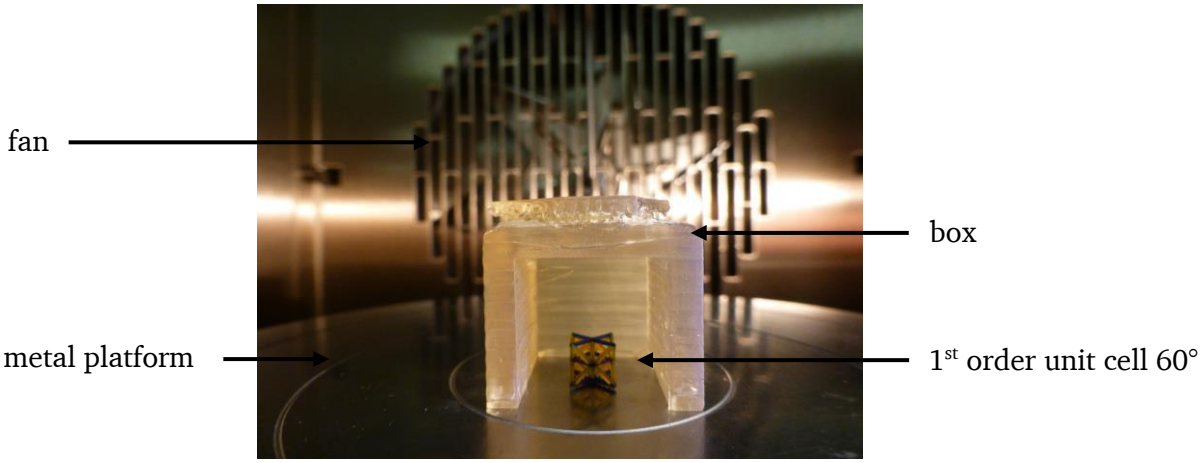

Figure 19: 1st order unit cell 60° in INSTRON heating chamber

The computation of the CTEs for the structures is also accomplished with the MATLAB software. Further tests are practicable right afterwards because the heating chamber is already preheated. Depending on the symmetry of the sample, one or two measurements are required to compute the volumetric CTE because the thermal deformation is only detectable from the front side and thus in width and height and not in depth.

By explaining the equipment and the test procedure for both cases a general understanding for the thermal expansion tests is created before the tests are conducted in the subsequent step.

5 Thermal Expansion Tests

An important concept for this thesis is transferring the theory of a tunable CTE for multi-material hierarchical structures, which was predicted by Xu and Pasini for metals, to polymers with lightweight character. [XP16] For conducting and investigating this case, first the base materials have to be examined to pick the appropriate constituents. After selecting the suitable components for the thermal expansion tests, the investigation starts with a 1st order unit cell before inspecting samples of 2nd order unit cells.

5.1 Investigation of the Coefficient of Thermal Expansion of the Base Materials

The first step of creating a hierarchical multi-functional structure is the investigation of the base materials regarding their coefficient of thermal expansion. The examination has to be done because neither Autodesk nor formlabs provide CTE values and for the home-made resins pureA and pureB the CTE values are also unknown. In general, the coefficients of thermal expansion of polymers have a large range, from for instance 10 x 10^{-6} 1/°C for polyurethane to 250 x 10^{-6} 1/°C for polyethylene. [MW05]

The thermal expansion tests are conducted on the hot plate as described in section 4.2.1. and the subsequent Figure 20 represents the computed average CTE values of the tested resins Autodesk black, Autodesk clear, Autodesk cyan, formlabs flexible, as well as the home-made resins pureA and pureB.

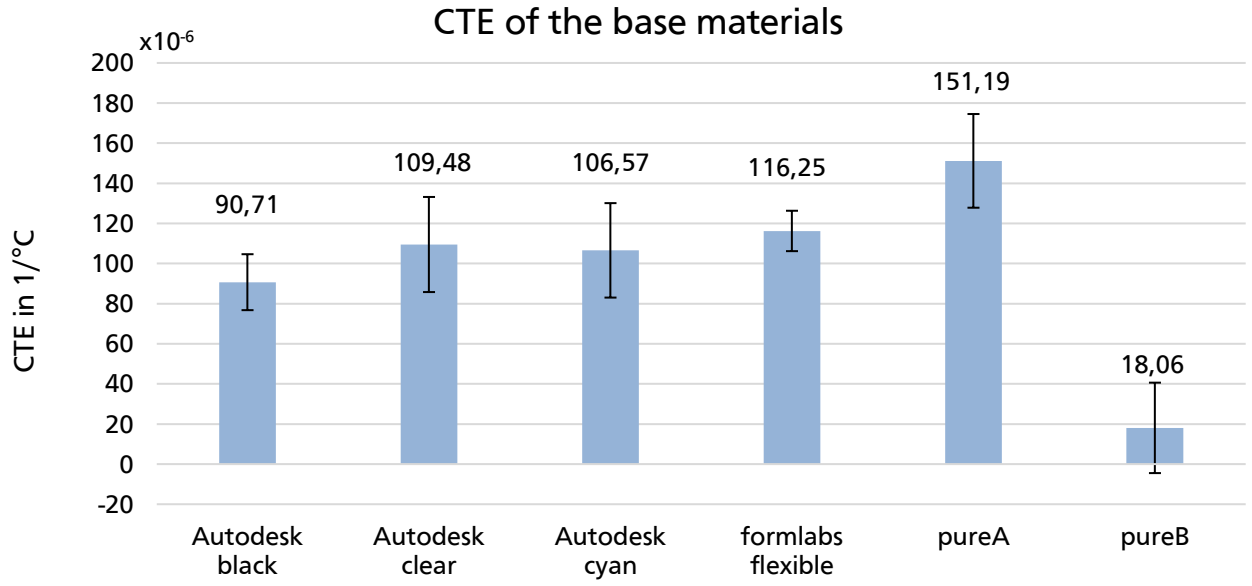

Figure 20: CTE of the base materials

All three coefficients of thermal expansion of the Autodesk resins are very similar and fall within the range of 90.71 x 10^{-6} 1/°C to 109.48 x 10^{-6} 1/°C where Autodesk clear has the highest and Autodesk black the lowest value. Formlabs' flexible CTE is 116.25 x 10^{-6} 1/°C which is slightly higher than the Autodesk values and pureA has the biggest CTE of all six resins at 151.19 x 10^{-6} 1/°C. Noticeable by far is the lowest CTE of the home-made resin pureB. At 18.06 x 10^{-6} 1/°C its CTE is at least five times lower than all the other CTEs. The individual standard deviation of each base material, which is pointed out by the vertical lines within the graph, reaches from 13.95 x 10^{-6} 1/°C to 23.70 x 10^{-6} 1/°C with an average standard deviation of 19.53 x 10^{-6} 1/°C. Although there is a wide range of the CTEs they are still within the scope of the literature values.

For selecting the appropriate resin combination for the thermal expansion tests the CTE values of all tested materials are set in relation to each other and the CTE ratios are noted down in Table 6.

CTE ratios	Autodesk black	Autodesk clear	Autodesk cyan	formlabs flexible	pureA	pureB
Autodesk black	T	1:1.2	1:1.2	1:1.3	1:1.7	5:1
Autodesk clear	1.2:1	U	1:1	1:1.1	1:1.4	6:1
Autodesk cyan	1.2:1	1:1	D	1:1.1	1:1.4	5.9:1
formlabs flexible	1.3:1	1.1:1	1.1:1	V	1:1.3	6.4:1
pureA	1.7:1	1.4:1	1.4:1	1.3:1	T	8.4:1
pureB	1:5	1:6	1:5.9	1:6.4	1:8.4	B

Table 6: CTE ratios of the base materials

From the analytical computation in chapter 3 we know that a large negative thermal deformation is achievable by either choosing a skew angle of 55° over 60° or by increasing the CTE ratio of the constituents. Since the skew angle is a design aspect the focus is on the high CTE ratios in Table 6. As seen from the bars in Figure 20 the CTE ratios between the three Autodesk resins, formlabs flexible and pureA all vary within a small range from 1:1 to 1.7:1. Bigger CTE ratios are presented in the row and column of component pureB. For this reason, pureB is picked as the material with the lowest coefficient of thermal expansion. In combination with pureA the highest CTE ratio of 8.4:1 is possible, but because of the high expenses and the low availability this option is crossed out. Low availability is also the reason for not considering Autodesk clear resin. Another option is formlabs flexible resin where the CTE ratio of 6.4:1 is the second highest behind the one of pureA to pureB. But it has a crucial drawback because of its high viscosity. This is especially disadvantageous for printing samples with a very small strut diameter of 200 μm or lower. From experience we know that resin leftovers are more likely to stick in free spaces and the additional weight of the resin will cause cracks or failures of the thin struts over a printing time of a few hours. Also, extra washing cycles are required for a proper printing result which increases the printing time and the amount of ethanol needed. For these reasons formlabs flexible is also not an option for the thermal expansion tests. After eliminating three components only Autodesk black and Autodesk cyan are left as possible constituents for pureB. Both resins are sufficiently available so the decision is made in favor of the higher CTE ratio of 5.9:1 of Autodesk cyan to pureB.

Therefore, the upcoming thermal expansion tests for the 1st and 2nd order structures are conducted with Autodesk cyan as the material with the high CTE value and pureB is used for the struts with the low CTE value. The CTE ratio of 5.9:1 is close to the computed analytic result for a ratio of 6:1, and the tests should verify these predictions.

5.2 Investigation of the Coefficient of Thermal Expansion of Hierarchical Structures

The impact of heat on a 1st order unit cell of an octet-truss is investigated with thermal expansion tests before a higher 2nd order unit cell is evaluated. The objective is to validate and verify the theoretical assumptions regarding the tunability of the CTE especially towards the negative direction.

5.2.1 1st Order Unit Cell 60°

The first structure that is tested is a 1st order unit cell with a skew angle of 60°. As previously described in chapter 3, the unit cell is assembled out of eight tetrahedrons whereas the blue struts are assigned to the Autodesk cyan resin with a CTE of 106.57 x 10^{-6} 1/°C and the yellow struts consist out of the pureB resin with a CTE of 18.06 x 10^{-6} 1/°C. How the struts of the different material are arranged within the octet-truss can be seen in the CAD-model and the printed sample shown on the left-hand side and right-hand side, respectively in Figure 21.

Figure 21: CAD-model and printed sample of 1st order unit cell 60°

Before the thermal expansion tests are conducted the sample is measured with the ZEISS microscope. The dimensions of the sample from the top and from the side are shown in Figure 22 at a magnification of 7.5. Length of the struts and diameter of the struts are designed to be in a ratio of 6:1.

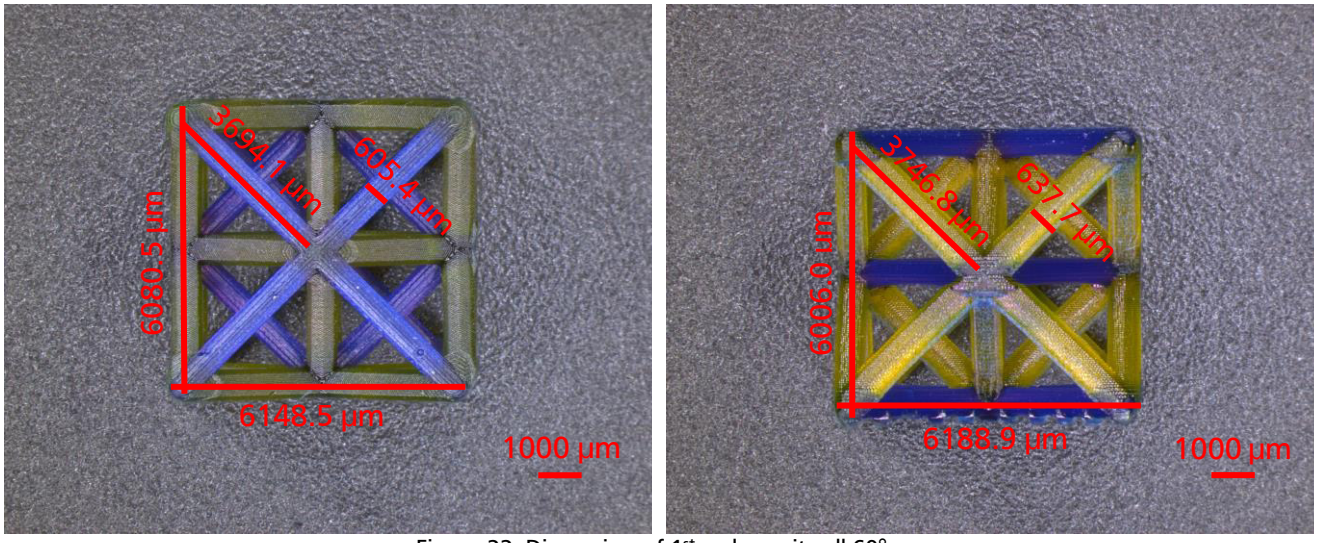

Figure 22: Dimension of 1st order unit cell 60°

For the thermal expansion tests every sample is only used once because by heating it up to 150°C it passes the glass transition temperature of pureB, which is around 62°C, and so the traits of the material change after cooling it down again. [GJS08] Due to the symmetry of the sample, two samples are used to detect the thermal deformation and thus compute the volumetric CTE. According to the analytic computation the height in the z-direction is supposed to shrink whereas the dimension in x- and y-direction should expand by the CTE of Autodesk cyan. The analytic predictions for this case of a 1st order unit cell 60° with a CTE ratio of 5.9:1 and at a temperature difference of 128°C are as follows:

$$\alpha_x = \alpha_y = \alpha_{cyan} = 106.57x10^{-6}\ 1/°C$$

$$\alpha_z = \frac{\sqrt{\left(1+\alpha_{pureB}\Delta T\right)^2 - 2cos^2\theta\left(1+\alpha_{cyan}\Delta T\right)^2} - \sqrt{1-2cos^2\theta}}{\Delta T\sqrt{1-2cos^2\theta}} = -71.46x10^{-6}\ 1/°C$$

However, the analysis of the video and the measurement with the pixel measurement software show an overall shrinkage of the 1st order unit cell. The results are visualized in a net diagram in Figure 23 to demonstrate the CTE along each strut and around each axis. In this way, the deformation and respectively the CTEs are easier to illustrate than in a bar chart. But because the CTEs are illustrated in a circle around the axes that are vertical to the surface of the sample, the axes change compared to the ones of the analytic prediction. These new axes are illustrated in the right top corner of Figure 23.

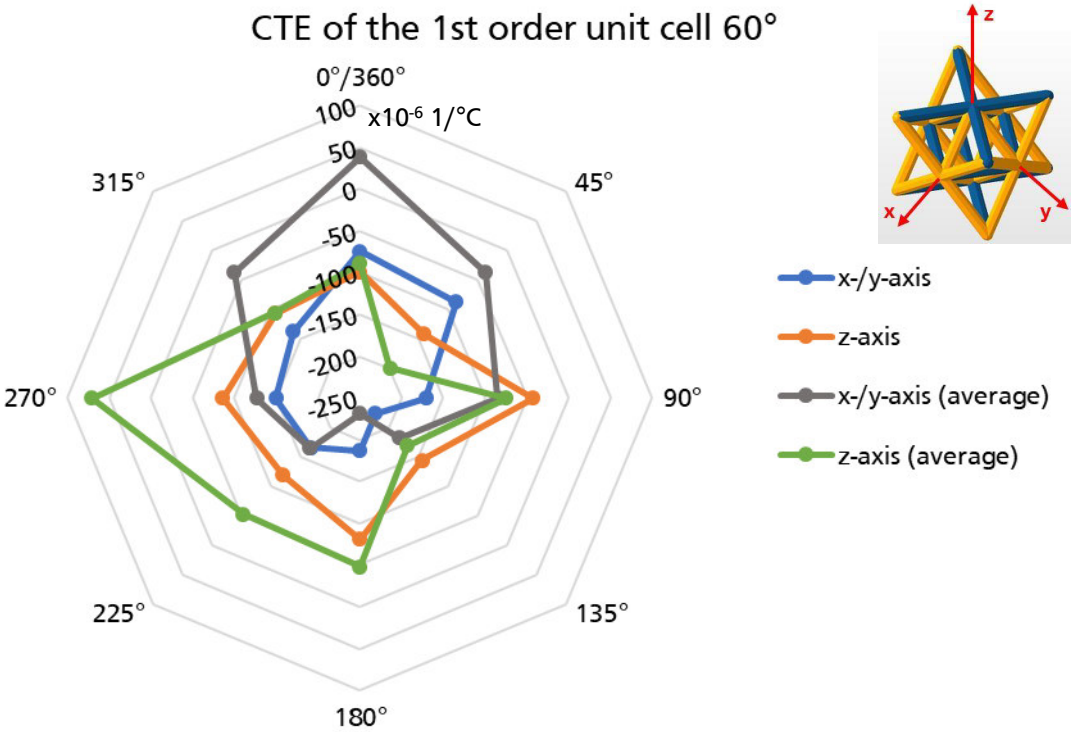

x 10^{-6} 1/°C	0°/360°	45°	90°	135°	180°	225°	270°	315°
x-/y-axis	-74.17	-87.06	-170.95	-224.07	-186.54	-166.08	-149.51	-137.03
(average)	38.74	-37.07	-84.93	-182.94	-231.64	-165.35	-126.67	-37.08
z-axis	-99.24	-141.39	-42.72	-144.55	-80.94	-119.48	-85.52	-106.58
(average)	-88.83	-199.11	-75.21	-169.80	-48.11	-53.04	70.73	-105.69
x-/y-area	-302.43 // -211.11 (average)							
z-area	-252.99 // -262.14 (average)							
volumetric	-398.01 // -324.17 (average)							

Figure 23: CTE of the 1st order unit cell 60°

To transfer the CTE values from the measurement to the analytic predictions the following conversion is necessary. From the CTEs of the z-axis in the net diagram in 135° and 315° direction the average value results in the α_x of the prediction. Also around the z-axis but this time at an angle of 45° and 225° the CTE of α_y is computed. The CTE α_z is computed by looking at the height in x-/y-direction of the net diagram. This means in 0°/360° and 180°. Hence, the measured CTEs for the x-, y-, and z-direction are

$$\alpha_x = -125.57x10^{-6}\ 1/°C$$

$$\alpha_y = -130.44x10^{-6}\ 1/°C$$

$$\alpha_z = -130.36x10^{-6}\ 1/°C$$

It can clearly be seen that only α_z is roughly meeting the predicted value, whereas the other CTEs are showing contrary behavior. The CTE values in the principal directions are all negative, hence the thermal expansion in x-, y-, and z-area is also negative as well as the overall volumetric CTE. The result for the volumetric CTE of -398.01 x 10^{-6} 1/°C is in contrast to the theory that predicts a positive volumetric CTE of about 71 x 10^{-6} 1/°C for a 1st order unit cell 60° and a CTE ratio of 6:1.

With the experimental results being in contrast to the analytic prediction the accuracy of the measurement method is questioned. For checking the exactness of this method, the measurements are repeated five times with the same pictures in x- and y-direction of the initial and final state of the sample to get the error of measurement. Figure 24 illustrates the minimum and maximum CTE values in each direction as well as the average value. Thereby it can be seen, that for the 0°/360°, 90°, and 315° directions the results show positive and negative CTEs. Moreover, the analysis of these measurements results in an average standard deviation of 73.31 x 10^{-6} 1/°C. This large standard deviation in- or decreases the values of above listed CTE values of α_x, α_y, and α_z by more than 50% and shows that the error of measurement is not negligible.

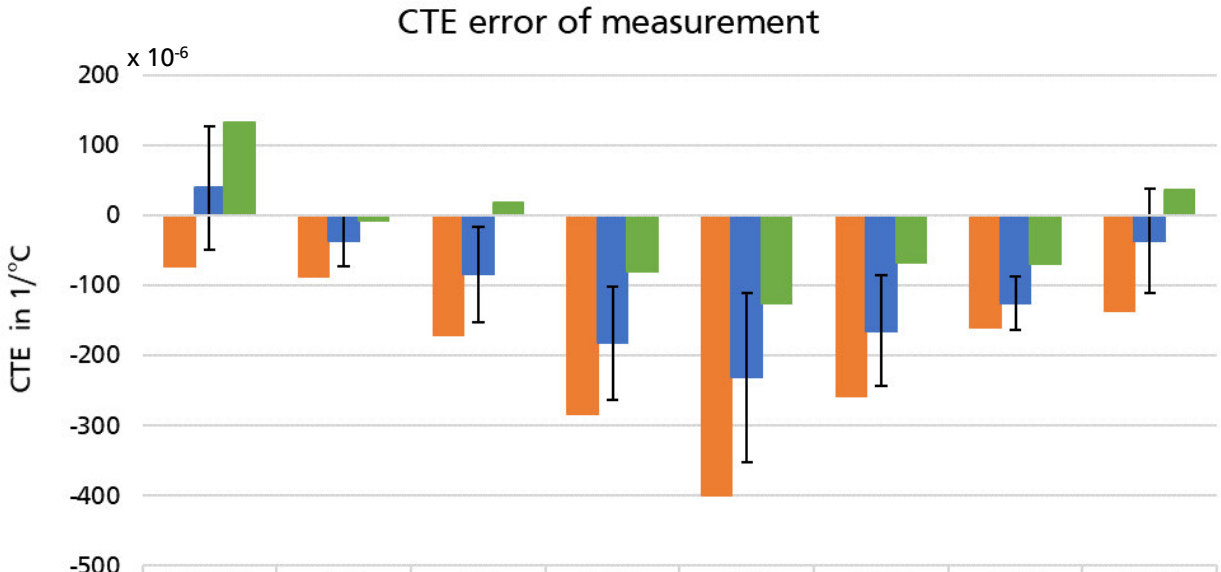

	0°/360°	45°	90°	135°	180°	225°	270°	315°
min	-74.17	-87.06	-170.95	-284.83	-400.56	-258.92	-160.60	-137.03
average	38.74	-37.07	-84.93	-182.94	-231.64	-165.35	-126.67	-37.08
max	131.86	-7.81	18.31	-81.25	-125.42	-67.36	-69.68	35.98

Figure 24: CTE error of measurement of the pixel measurement method

By observing the average CTE values in x-, y-, and z-direction the new results are now:

$$\alpha_x = -137.75x10^{-6}\ 1\ /°C$$

$$\alpha_y = -126.08x10^{-6}\ 1/°C$$

$$\alpha_z = -96.45x10^{-6}\ 1/°C$$

Only the average α_z with -96.45 x 10^{-6} 1/°C is getting closer to the predicted value of -71.46 x 10^{-6} 1/°C and would be within the range of the standard deviation, but the CTEs α_x and α_y are still far off even with considering the large standard deviation. An assumption for this behavior might be a change of the characteristics of the resins by passing the glass transition temperature.

Although the first thermal expansion test deviates from the analytic prediction a shrinkage is visible in the measurements and the video so the thermal expansion tests are continued with a 2nd order hierarchical structure.

5.2.2 2nd Order Unit Cell 60°

This 2nd order unit cell 60° is assembled out of 180 1st order unit cells 60° and scaled to a cubic dimension of 14 x 14 x 14 mm. All bars consist of five connected 1st order unit cells and the sample is completely symmetric. An impression of the CAD-model as well as the printed 2nd order unit cell 60° out of Autodesk cyan and pureB is given in Figure 25. The variation of the color within the printed sample is caused by the dyeing of the pureB struts by Autodesk cyan during the washing process.

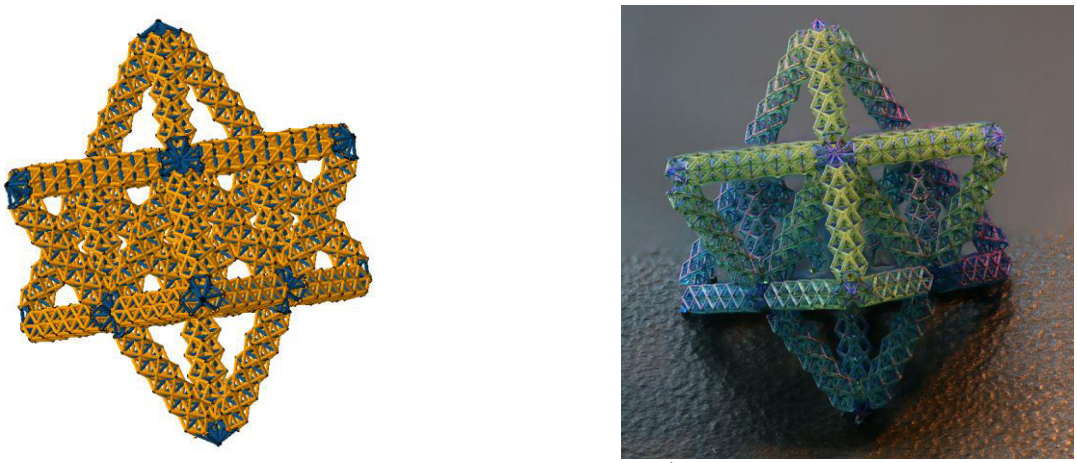

Figure 25: CAD-model and printed sample of 2nd order unit cell 60°

Pictures from the microscope with a magnification of 7.5 for the quarter section of the complete 2nd order unit cell 60° and a 40 times magnification of the bar are shown in Figure 26. It can be seen that almost all the joints at the corners are incompletely printed. This is traced back to having a strut diameter of only around 170 μm at a strut length to strut diameter ratio of 6:1. At the corners the joints are fairly exposed to the airflow of the fan that dries the sample after the washing process. The low stiffness of struts at the corners is the reason why they are getting bent during the drying process. As a result of the bending the next printing layer is no longer attached to the previous one and hence the connection of the strut is interrupted.

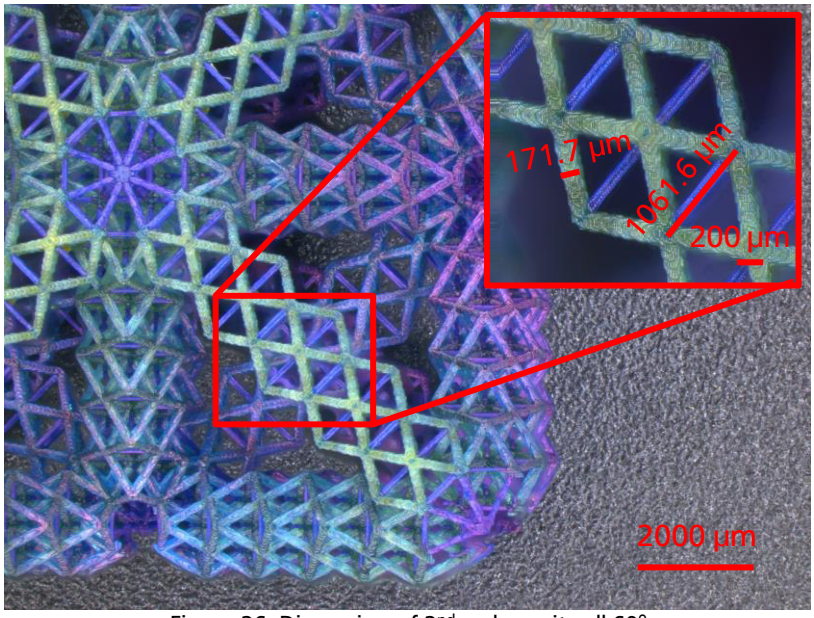

Figure 26: Dimension of 2nd order unit cell 60°

Although the sample is not perfectly manufactured the heating test is conducted and the results are shown in Figure 27. The CTE values are averaged like in the previous measurement to reduce the deviation.

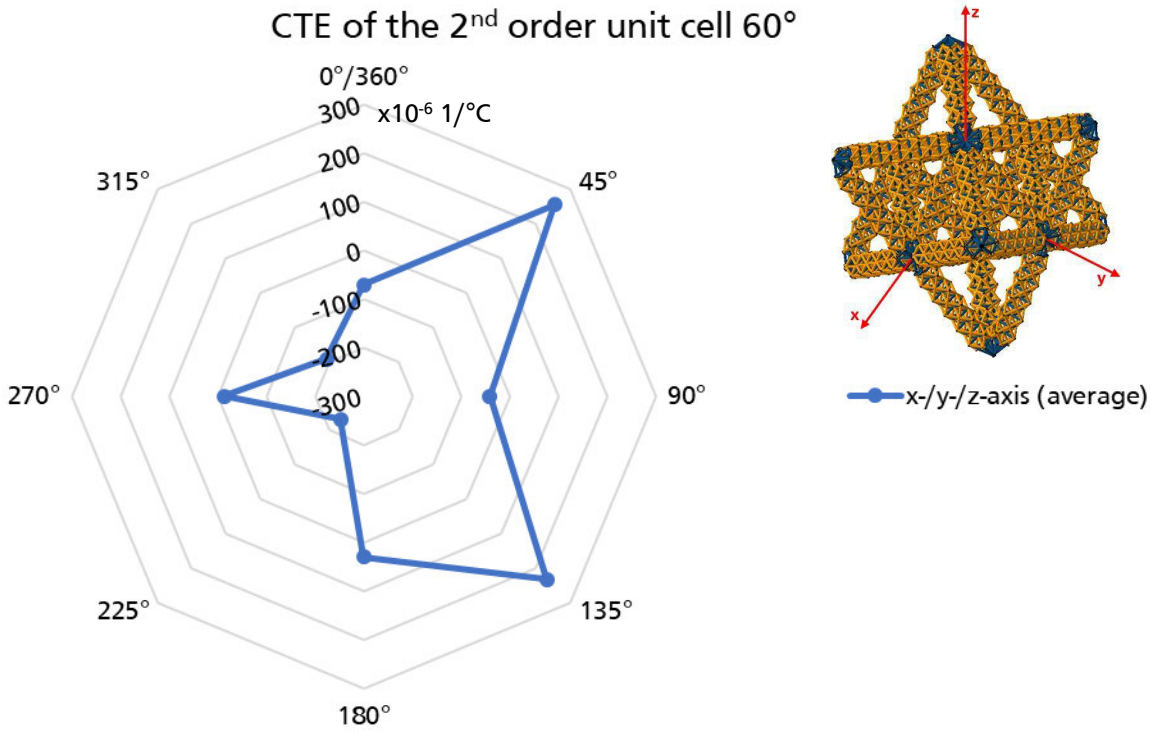

x 10^{-6} 1/°C	0°/360°	45°	90°	135°	180°	225°	270°	315°
x-/y-/z-axis	-71.91	254.74	-41.58	231.85	30.90	-233.26	-13.46	-191.98
area	23.25							
volumetric	35.81							

Figure 27: CTE of the 2nd order unit cell 60°

In the table shown in Figure 27, the listed CTE values alternate between positive values - expansion - and negative values - shrinkage. In the 0°/360°, 90°, 180°, and 270° directions the values vary around

zero by considering the standard deviation of about 73 x 10^{-6} 1/°C. The CTEs α in the directions of 45° and 135° are both positive and bigger than 200 x 10^{-6} 1/°C, whereas in the opposite directions the CTEs are around -200 x 10^{-6} 1/°C. This big difference is probably caused by a shift of the center point, but by adding up the deformations they roughly cancel each other out like all the others do. Hence, the volumetric thermal expansion of the 2nd order unit cell is 35 x 10^{-6} 1/°C which is close to zero. These results of the measurements are not close to the analytic prediction of the volumetric CTE of about -100 x 10^{-6} 1/°C for the 2nd order sample and are not an even lower CTE than the one observed for the 1st order unit cell. By evaluating the video of this test, the sample is neither expanding nor shrinking, which confirms the measurements.

A reason for the nonnegotiable thermal expansion might be the incompletely printed joints of the sample. A more likely reason is that the 150°C preheated chamber is heating up the 2nd order unit cell with its thin struts within the first few seconds so that the sample has already reached its final state before closing the door of the heating chamber and starting the video, respectively taking the pictures.

To solve these two problems the idea is to increase the stiffness of the struts by changing the ratio from 6:1 to 5:1 and by conducting the thermal expansion test without preheating the chamber to detect the deformation of the sample. The drawback of this approach is that the deformation will probably not be visible in the video because of the relative movements of the metal platform and the box around the sample. Additionally, a change of the skew angle from 60° to 55° is executed because according to the theory the predicted shrinkage should be larger and thus easier to examine.

5.2.3 2nd Order Unit Cell 55°

By changing the skew angle from 60° to 55° the cubic shape of the sample becomes an ashlar and the symmetry reduces from three to two directions - x and y – in comparison to the 2nd order unit cell 60°. The new dimension of the 2nd order unit cell 55° is 14 x 14 x 10.58 mm and represented in Figure 28.

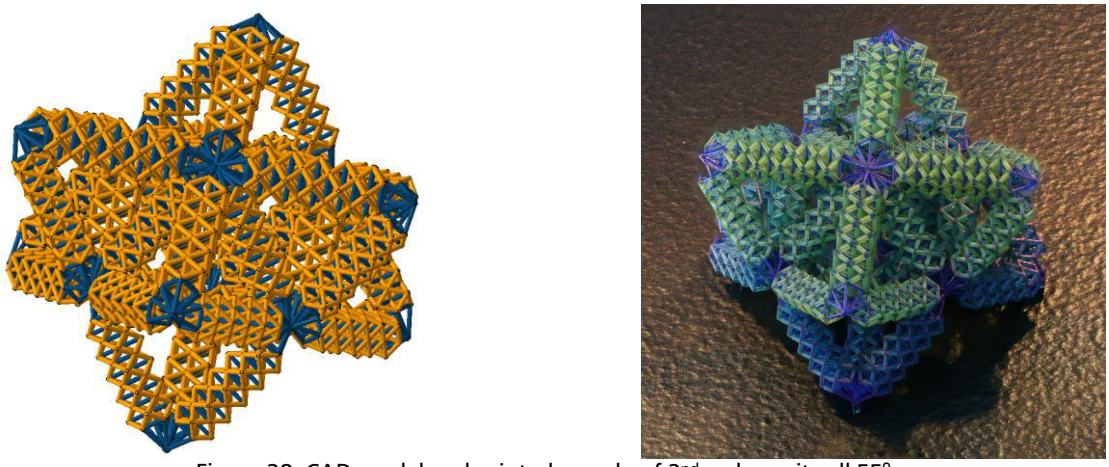

Figure 28: CAD-model and printed sample of 2nd order unit cell 55°

This printed sample of the 2nd order unit cell 55° with a strut length to strut diameter ratio of 5:1 shows that still not all the struts in the joints are printed but enough of them are existent so that there is a connection between the bars. Measurements of this sample at a magnification of 40 are illustrated in Figure 29.

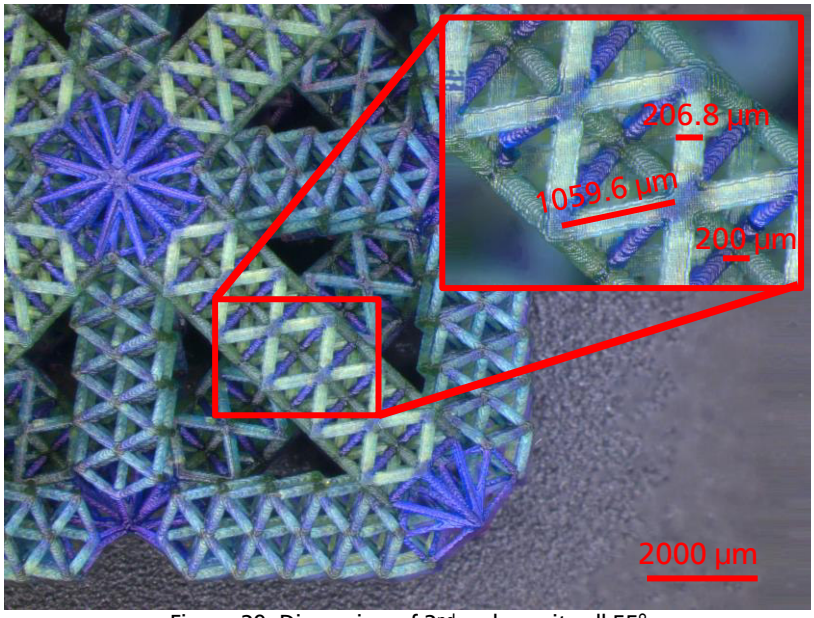

Figure 29: Dimension of 2nd order unit cell 55°

In this heating test, the INSTRON heating chamber is not preheated so that the initial temperature inside the chamber equals the room temperature of 22°C at the beginning. After setting up the sample, a picture of the initial state is taken and the video is started before the temperature of the heating chamber is set to 150°C. Fifteen minutes later the picture of the final state is taken for the analysis of the test. While evaluating the graphical material, the video shows movements of the metal platform and the box caused by their own thermal expansion, so that in the video a deformation of the sample is not visible. But by

comparing the picture of the initial state with the one of the final state the measurements for the CTE are feasible with the pixel measurement method. The results are shown in Figure 30.

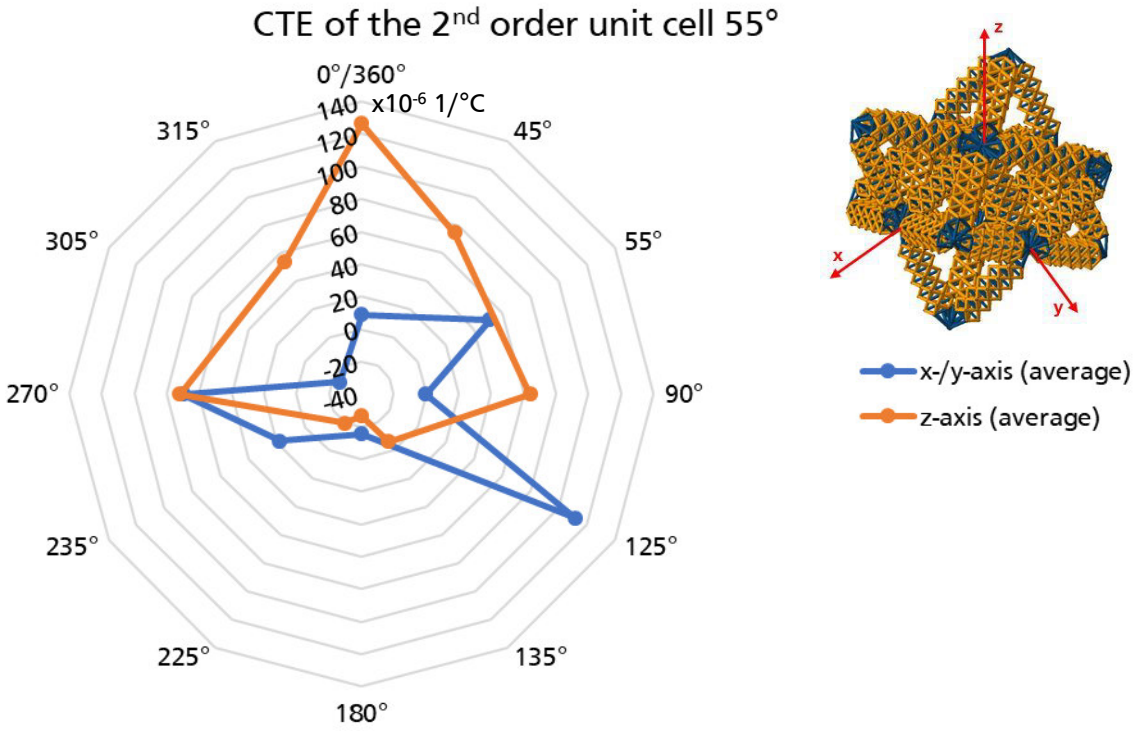

x 10^{-6} 1/°C	0°/360°	55°|45°	90°	125°|135°	180°	235°|225°	270°	305°|315°
x-/y-axis	8.79	51.51	-0.44	112.15	-15.37	18.01	69.74	-24.91
z-axis	126.38	74.67	63.96	-6.19	-26.72	-19.26	71.93	54.28
x-/y-area	48.87							
z-area	51.28							
volumetric	102.84							

Figure 30: CTE of the 2nd order unit cell 55°

For the CTE, the values around x-, y-, and z-axis vary from -26.72 x 10^{-6} 1/°C to 126.38 x 10^{-6} 1/°C where the distribution is skewed towards the higher positive CTEs. As a result, the CTE values of the areas as well as the volumetric CTE are positive. The volumetric CTE of 102.84 x 10^{-6} 1/°C is clearly positive which indicates an expansion of the sample. After eliminating the preheating of the chamber as a possible reason for the nonnegotiable shrinkage of the sample, the actual reason must be different. Hence, two more hypotheses are investigated to figure out why shrinkage of a 1st but not of a 2nd order unit cell is observable:

1. The incompletely printed joints are not able to connect the bars in a strong enough way, which means that the bars are not able to influence each other.

2. A reduction of the diameter changes the characteristics of the struts and thus the size has an impact on the result although the strut length to diameter ratio remains the same – which will be referred to as the size effect.

The first hypothesis is still referring to the not fully printed joints of the sample which might have an impact on the interaction of the bars of the 2nd order unit cell during the thermal deformation. To solve

this problem of the weak connection between the bars the joints of the 2nd order unit cell 55° are redesigned as solid cones to assure a strong connection. Figure 31 shows the CAD-model and the printed sample with the new designed joints of the 2nd order unit cell 55°.

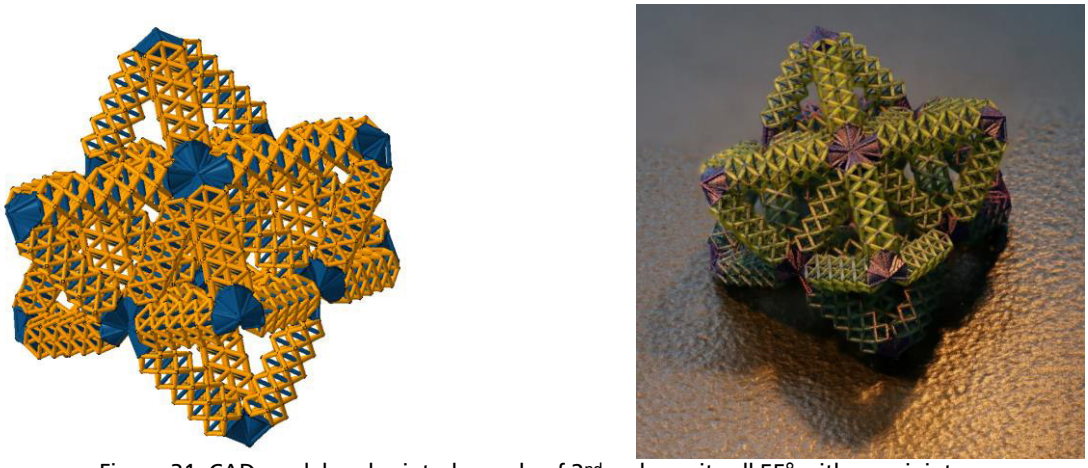

Figure 31: CAD-model and printed sample of 2nd order unit cell 55° with new joints

With the dimension of the struts and the test conditions remaining the same as for the previous 2nd order sample, the thermal expansion test is conducted and the results can be seen in Figure 32. Because of a lack of resin and the enormous off time of the multi-material printer only one sample of the 2nd order unit cell is available for the testing.

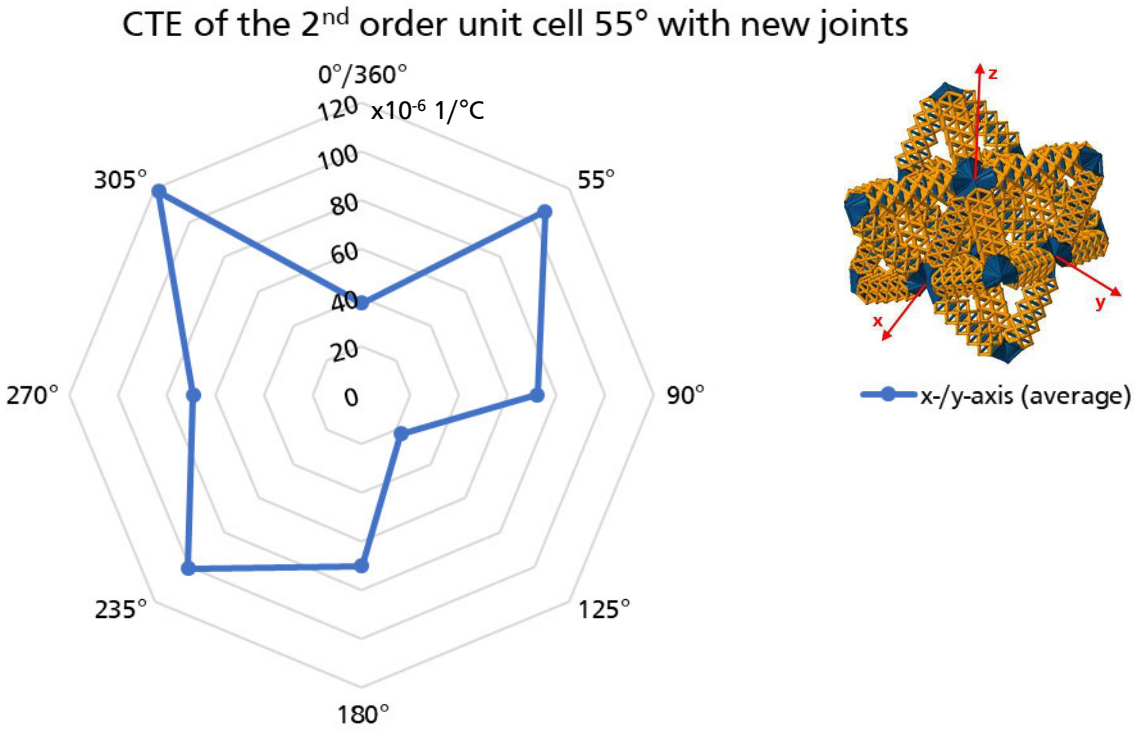

x 10-6 1/°C	0°/360°	55°	90°	125°	180°	235°	270°	305°
x-/y-axis	37.65	106.30	72.15	22.53	70.25	100.90	69.26	117.99
x-/y-area	165.18							

Figure 32: CTE of the 2nd order unit cell 55° with new joints

All CTE values shown in the net diagram of Figure 32 and the table beneath are positive in all directions and by computing the thermal deformation of the observed x-/y-area the expansion is 2.12%. This means that the 2nd order unit cell 55°, even with the newly designed joints is not able to shrink and the weak joints are not the reason for this problem. Thus, the first hypothesis is proved wrong and now the second hypothesis is contemplated.

Examining the second hypothesis that suggests that the size effect is the origin of this problem means observing the struts of a 2nd order unit cell 55° before and after the heating test to see if there are any abnormalities. The struts of the 2nd order unit cells have a decreased diameter of about 200 μm which is only 33% of the diameter of the 1st order unit cell although the ratio between the length of the strut and the diameter has been lowered from 6:1 to 5:1. This adaptation of the size is caused by the available printing area of the multi-material printer which is 20 x 15 mm.

By looking at the pictures from before and after the heating test of a 2nd order unit cell 55°, small cracks within the struts of pureB are visible in Figure 33 (b) at a magnification of 63.

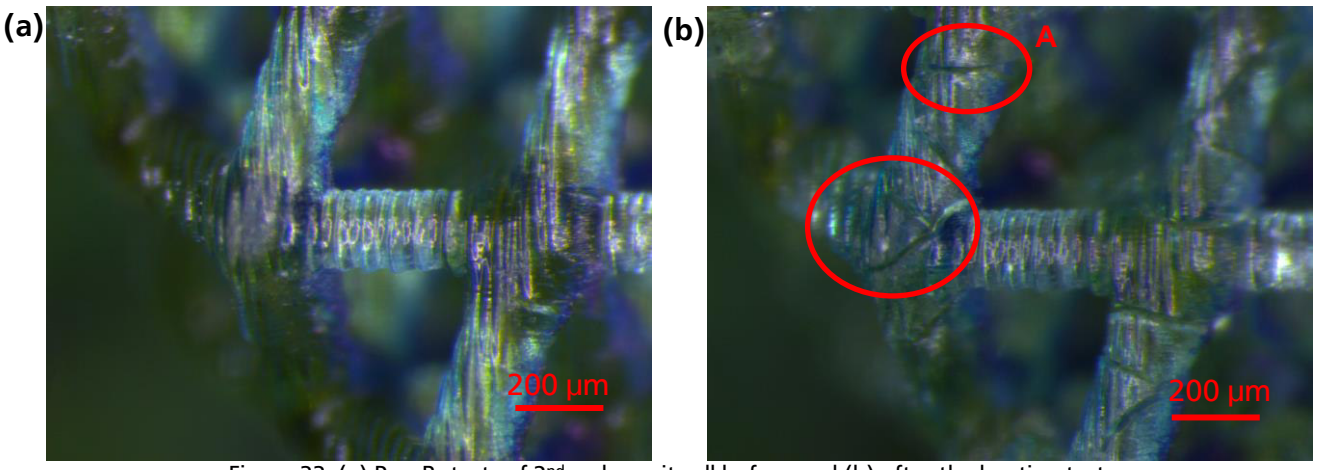

Figure 33: (a) PureB struts of 2nd order unit cell before and (b) after the heating test

In Figure 33 (a) the struts of pureB do not show any cracks in comparison to the picture on the right-hand side which represents the sample after the heating test. The cracks are marked within the red circles and it can be seen that they are going across the complete strut. To emphasize the cracks a picture with a magnification of 125 is taken of section A and shown in Figure 34.

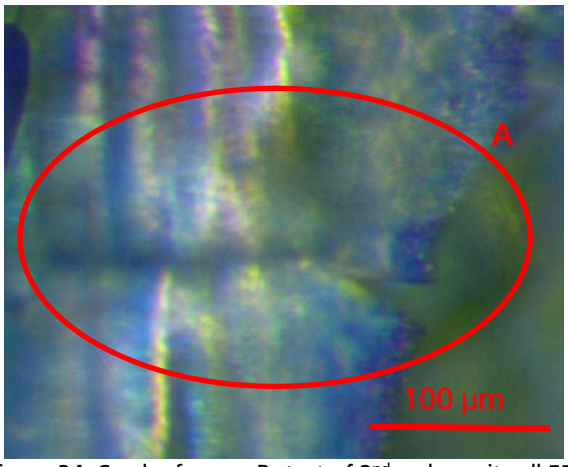

Figure 34: Crack of a pureB strut of 2nd order unit cell 55°

The crack shown in Figure 34 is more than a split within the strut. It is breaking the strut apart and creating a notch. More of these kinds of cracks are distributed all over the struts of pureB of the 2nd order unit cell and they are the reason why the sample is not able to shrink and instead slightly expands. In contrast to the struts of pureB, the struts of Autodesk cyan are not having any cracks after the heating test. As an example, the struts at the corner of the 2nd order unit cell 55° are demonstrated in Figure 35.

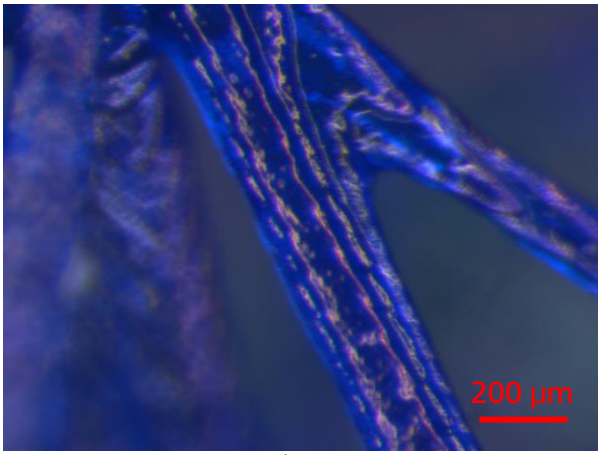

Figure 35: Autodesk cyan struts of 2nd order unit cell 55° after the heating test

This phenomenon is probably caused by the different traits of the base material. Autodesk cyan has a Young's modulus of 550 MPa which is lower than the one of pureB at around 800 MPa. Furthermore, the CTE of Autodesk cyan is 5.9 times higher than the one of pureB which probably causes lower tension within the struts.

Explaining this case by mentioning the traits of the materials raises the question why we are able to observe shrinkage at the 1st order unit cell 60°, but not at the 2nd order unit cell. We will have a closer look at the struts of resin pureB of the 1st order unit cell 60° before and after the heating process. As shown in Figure 36 (b) there are some small cracks visible in comparison to Figure 36 (a) which illustrates the strut before the heating test.

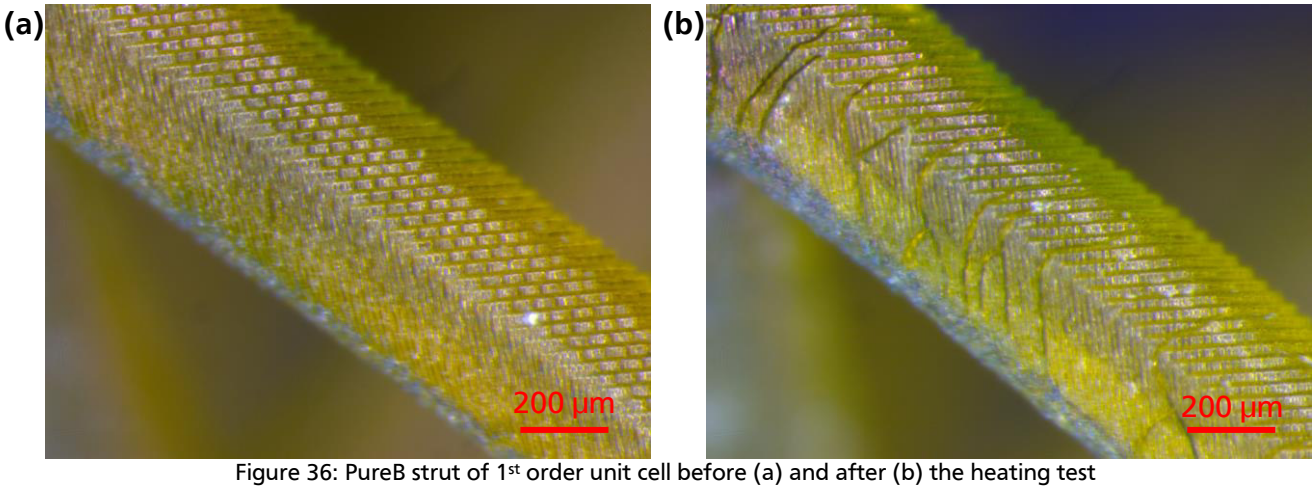

Figure 36: PureB strut of 1st order unit cell before (a) and after (b) the heating test

But these cracks are not as serious as they are at a higher order sample. At a diameter size of around 600 μm the cracks are not damaging the strut so much that the strut is breaking. This compensation of the cracks by the larger diameter of the 1st order unit cell 60° is enabling the sample to shrink.

In conclusion, we can say that the size of the minimum strut diameter has an impact on the performance of the thermal expansion test and thus on the CTE. The size effect is determined to be the critical factor why the higher order sample are not shrinking after also considering the hypotheses of stiffer joints or the error of measurement.

5.2.4 Conclusion

The thermal expansion tests of the 1st order unit cell 60° show that in contrast to the analytic prediction where the sample is supposed to shrink in only the z-direction, the sample is shrinking in all three directions. The reason for this unexpected behavior might be caused by a change in the characteristics of the resin by passing the glass transition temperature. This already high negative thermal deformation of the 1st order unit cell leads to the assumption that the 2nd order unit cell has to have a much higher negative volumetric CTE than the theory predicted. But instead of shrinking, the higher hierarchical structures are expanding. By considering different reasons for this cause, such as an error in the measurement method or not fully printed joints, it is figured out that cracks within the thin struts break the struts and prevent the sample from shrinking. Further examinations of the 1st order unit cell struts also demonstrate that at a larger diameter the cracks are not harming the struts, in contrast they are compensated by them. Hence, the size of the diameter has an impact on the results of the thermal expansion tests.

At this point the experimental part is halted because the current multi-material printer is very unstable and has an enormous off time. Moreover, the multi-material printer wastes a huge amount of resources like the resins and the ethanol for each printed unit cell, especially for 2nd order structures when frequent material changes are required. Based on these facts the decision has been made to update the printing system. Simultaneously, ideas for a different kind of structure are gathered, designed, and simulated regarding a negative thermal expansion.

6 Design of new Multi-Material Unit Cells with negative Coefficient of Thermal Expansion

In the previous chapters the thermal expansion of 1st and 2nd order octet unit cells with different skew angles have been investigated. Now different single-material unit cells are reviewed and two are selected and modified to multi-material structures with theoretically analyzing their behavior under thermal load. This simulation is aiming for an alternative for the CTE of the octet-truss or an even better opportunity.

6.1 Review of Single-Material Structures for Unit Cells

Besides the mentioned octet-truss structure for a unit cell, several other unit cells exist and seven are subsequently described. Vaidya and Anand are using truncated octahedron and rhombic dodecahedron unit cell models that are pictured in Figure 37 (a) and (b) for fabrication of support structures because of the advantage of this lightweight structure and also because of the provided flexibility for creating support in different directions by multiple faces of these unit cells. [VA16]

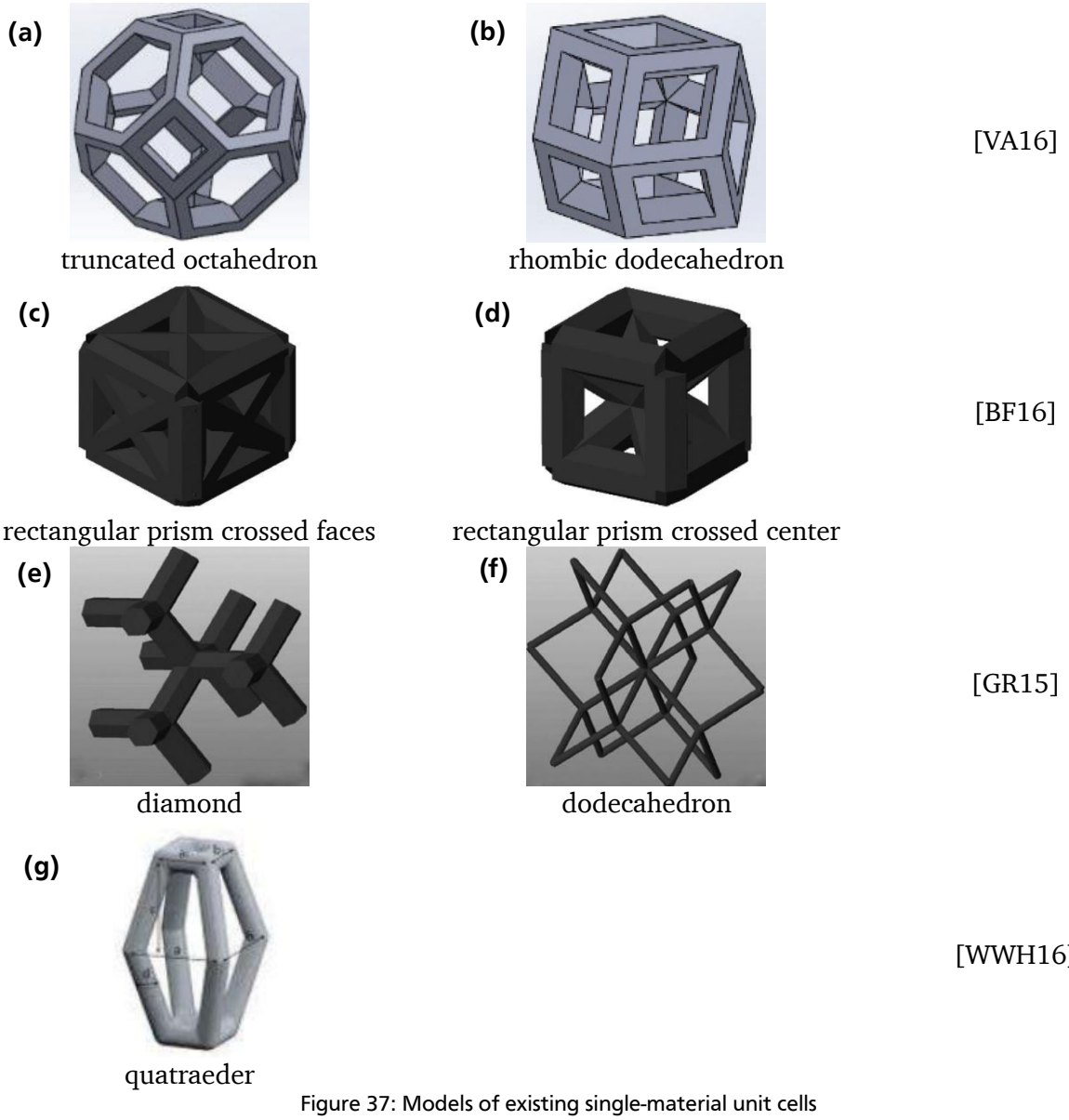

Figure 37: Models of existing single-material unit cells

A different way to create a unit cell is through Beyer and Figueroa's design. Their design of a unit cell for additive manufacturing is based on a rectangular prism. For the first one in Figure 37 (c) the faces are containing crosses but the core of the unit cell remains empty, whereas the rectangular prism with a crossed center in Figure 37 (d) has diagonal struts in the inside but the faces are left blank. [BF16] Furthermore, the diamond and the dodecahedron unit cell of Galba and Reischle are shown in the images (e) and (f) in Figure 37. [GR15] The last unit cell in Figure 37 (g) that is mentioned by Weißmann et al. is here called quatraeder. This design, consists of squares at the bottom and at the top which are linked by eight struts with their joints facing outwards. [WWH16]

Not all of the above listed single-material unit cells are appropriate for creating a high negative CTE structure by assigning materials with different coefficient of thermal expansion. The unit cells (a) and (b) in Figure 37 consist of a hollow frame that leaves less opportunities even by adding internal cross struts because of the closed shape. The shape of a rectangular prism of the unit cells in Figure 37 (c) and (d) leaves no opportunity to achieve a negative volumetric CTE because struts are facing straight in x-, y-, and z-direction. Thus, an expansion in all directions is inevitable. Other problems with similar concerns are shown by the diamond unit cell (e) in Figure 37 that is very branched with 12 open ends. This means that even by assigning different materials the unit cell has still the chance of expanding freely. Adding several connections or a frame around the diamond would change the structure completely and building up a higher order diamond unit cell is very complex and not promising.

More promising is a modification of unit cell (f), the dodecahedron that is visualized in the CAD-model in Figure 38 with the blue struts assigned to Autodesk cyan resin and the yellow ones to pureB resin. By adding the blue vertical struts of Autodesk cyan to the original model, the middle squares get divided into triangles. This separation has the same effect on the dodecahedron as it has on the tetrahedron in chapter 3 which means that there is a potential of achieving a negative volumetric CTE for this unit cell. For a variation of the dodecahedron the skew angle Θ is used within the triangle.

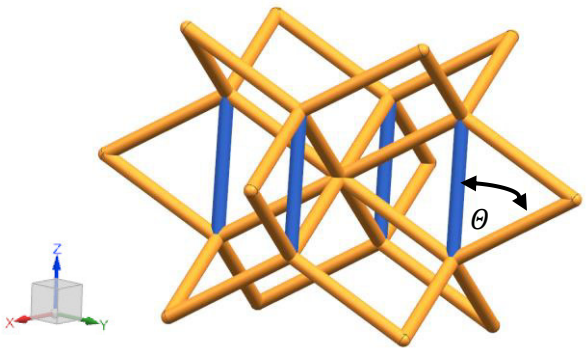

Figure 38: CAD-model of modified multi-material dodecahedron

A small change of the quatraeder unit cell in Figure 37 (g) will also have the potential of achieving a negative volumetric CTE of the multi-material unit cell under thermal load. Adding a third horizontal square at the middle of the quatraeder that has double the lateral length of the top and bottom squares and assigning these squares to the Autodesk cyan resin, whereas the other struts are assigned to pureB resin, will influence the volumetric CTE. The dimension of the quatraeder is defined by the length of the strut of Autodesk cyan a and the length of the strut of pureB b and thus the ratio between both those struts a:b. These adjustments as well as the parameter a and b are shown in Figure 39 in a CAD-model and because of the arrangement of the materials, shrinkage in z-direction is expected.

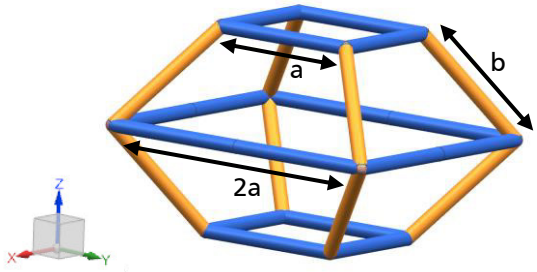

Figure 39: CAD-model of modified multi-material quatraeder

After considering the existing single-material unit cells regarding their potential of a negative volumetric CTE as a multi-material structure the modified versions of the dodecahedron and the quatraeder offer the largest possibilities and thus are considered for the following analyses.

6.2 Simulative Prediction of Quatraeder and Dodecahedron

To get the volumetric CTE of the quatraeder and the dodecahedron both unit cells are built up in Siemens NX with single struts and degrees of freedom in the joints, so that the struts are capable of moving due to a change of length. Afterwards, the length in x-, y-, and z-direction is measured to get the initial length for the computation of the CTE. Then the thermal expansion of the Autodesk cyan and pureB struts is added at a temperature change ΔT of 128°C. This change in length of the struts causes a deformation of the unit cells and leads to the new dimension after an increase of temperature from 22°C to 150°C. The final length after the heating is measured and with the initial length and the temperature difference the CTEs α_x, α_y, and α_z are computed as well as the volumetric CTE. For the investigation of the quatraeder and the dodecahedron regarding their volumetric CTE the aspect ratio between the struts of Autodesk cyan a and pureB b increases from 1:1 to 1.25:1, whereas the dodecahedron varies in its skew angle Θ from 60° down to 45°.

6.2.1 Simulative Prediction of 1st Order Unit Cell Quatraeder and Dodecahedron

The Figure 40 demonstrates the trend of the volumetric CTE for the 1st order unit cells of the quatraeder and the dodecahedron at a thermal load ΔT of 128°C at different states.

At an aspect ratio of 1:1 the 1st order quatraeder has a positive volumetric CTE of 141.51 x 10^{-6} 1/°C whereas the dodecahedron with a skew angle of 60° has a lower but still positive CTE of 82.88 x 10^{-6} 1/°C. Changing the characteristics for the quatraeder by increasing the aspect ratio between a and b from 1:1 up to 1.25:1 leads to a steep decline of the volumetric CTE with the endpoint at -99.57 x 10^{-6} 1/°C. The trend of the dodecahedron also decreases but not as sharp as the one of the quatraeder and ends at -37.62 x 10^{-6} 1/°C with a skew angle of 45°. According to the graph, cross-over of both trends occurs between a strut ratio of 1.1:1 and 1.2:1 for the quatraeder and a skew angle of 55° to 50° for the dodecahedron. Both volumetric CTEs are approximately 30 x 10^{-6} 1/°C at this crossing point. During all the variation of the dimensions, the CTE of the quatraeder remains stable in x- and y-direction and for the dodecahedron in z-direction with 106.57 x 10^{-6} 1/°C, the CTE of Autodesk cyan. Thus, the quatraeder achieves its negative volumetric CTE by shrinking in the z-direction and the dodecahedron by having a negative thermal deformation in the x- and y-direction.

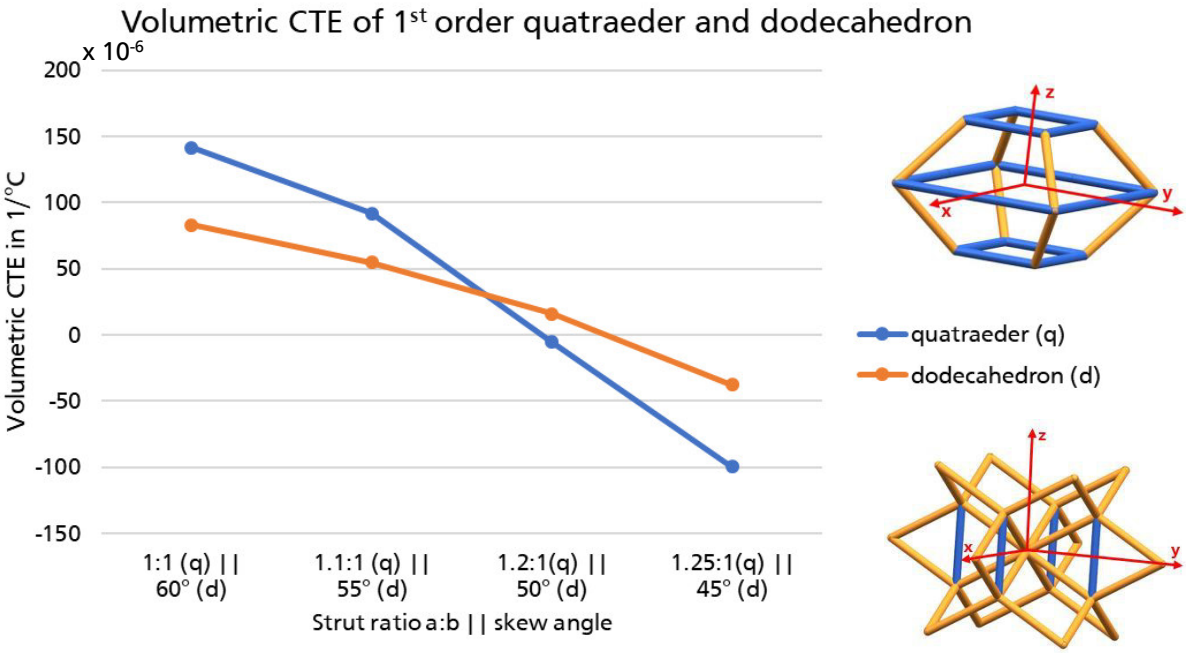

x 10^{-6} 1/°C	1:1(q) || 60°(d)	1.1:1(q) || 55°(d)	1.2:1(q) || 50°(d)	1.25:1(q) || 50°(d)
x-/y-axis (q)	106.57	106.57	106.57	106.57
z-axis (q)	-71.26	-119.65	-214.38	-305.90
volumetric (q)	141.51	91.80	-5.54	-99.57
x-/y-axis (d)	-11.73	-25.71	-44.91	-71.48
z-axis (d)	106.57	106.57	106.57	106.57
volumetric (d)	82.88	54.60	15.87	-37.62

Figure 40: Volumetric CTE of 1st order quatraeder and dodecahedron

Although the 1st order unit cell of the quatraeder starts at a higher positive volumetric CTE than the 1st order unit cell of the dodecahedron, it ends up at a more negative value. As a conclusion, the volumetric CTE of the quatraeder has a bigger slope over the same period compared to the dodecahedron. Therefore, the dodecahedron is neglected and only the quatraeder is considered in the following investigations of a 2nd order structure.

6.2.2 Simulative Prediction of 2nd Order Unit Cell Quatraeder

The 2nd order quatraeder is assembled of 120 1st order quatraeders, where the small squares on top and bottom consist of 20 1st order unit cells and the big square in the middle is made out of 40 1st order unit cells. The linking bars that were formerly assigned to pureB are now each aligned out of five 1st order quatraeders. The assembled CAD-model of the 2nd order quatraeder can be seen in Figure 41.

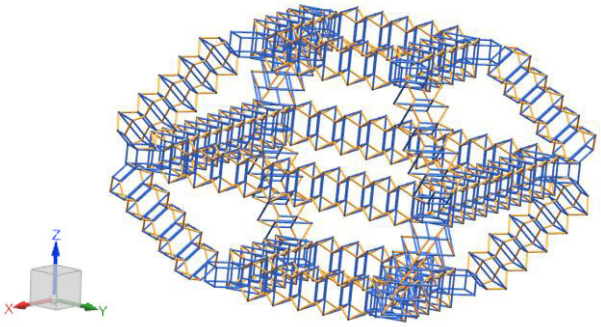

Figure 41: CAD-model of 2nd order quatraeder

By comparing the simulative results of the 1st order with the 2nd order quatraeder in Figure 42 it can be seen that the higher order unit cell starts at a lower volumetric CTE than the 1st order unit cell and that with -54.54 x 10^{-6} 1/°C it already has a negative value at an aspect ratio of 1:1. Both trends run almost parallel but with the 2nd order quatraeder having a slightly steeper slope. With the 2nd order quatraeder having a negative volumetric CTE of -360.94 x 10^{-6} 1/°C at an aspect ratio of 1.25:1 it is more negative than the 2nd order octet-truss with a predicted volumetric CTE of -299.38 x 10^{-6} 1/°C at a skew angle of 55° and a CTE ratio of 6:1. The biggest difference between the 1st and 2nd order quatraeders is that the CTEs of the 2nd order quatraeder in the x-, y-, and z-direction are all negative at any strut ratio, where the 1st order quatraeder has to compensate the expansion in x- and y-direction by shrinking in z-direction.

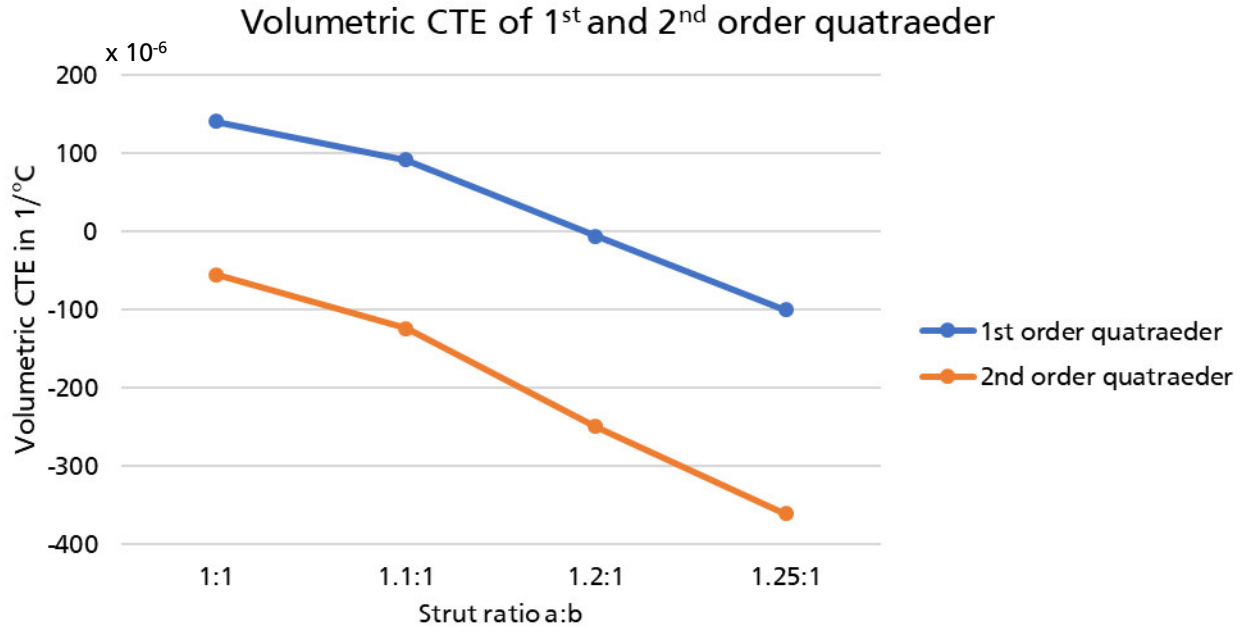

x 10^{-6} 1/°C	1:1	1.1:1	1.2:1	1.25:1
x-/y-axis (1st)	106.57	106.57	106.57	106.57
z-axis (1st)	-71.26	-119.65	-214.38	-305.90
volumetric (1st)	141.51	91.80	-5.54	-99.57
x-/y-axis (2nd)	-17.04	-39.78	-81.50	-118.96
z-axis (2nd)	-20.59	-44.62	-88.92	-128.73
volumetric (2nd)	-54.54	-123.54	-249.22	-360.94

Figure 42: Volumetric CTE of 1st and 2nd order quatraeder

This simulative prediction of the 1st order dodecahedron and especially of the 1st and 2nd order quatraeders demonstrates the possibility of these structures regarding a negative volumetric CTE. The 2nd order quatraeder shows an even higher potential than the 2nd order octet-truss.

With finishing the analysis of the new designed unit cells, the research about the negative CTE in practical and theoretical way stops to face the problems of the current multi-material printer and to improve the system.

7 Improvement of the Multi-Material Printer

Due to the fact that the multi-material printer is a complete new set up prototype some steps are not working out quite well yet and incidents occur during the printing process. In this chapter, the current state is listed with issues that have an important impact on the performance of the multi-material printer. Moreover, ideas are gathered for improving the system and recorded in a list of requirements followed by the development and design of the new system by using a morphological matrix and comparing different concepts. The best concept is chosen and the changes and improvements are implemented. Finally, the results are stated in comparison to the current multi-material printer.

7.1 Current State

Having a look at the multi-material printer and the printing process externalizes several problems which have a dramatic influence on the printing results as well as on the availability of the printer itself. The most urgent problems refer to the setup and the design of the printing process.

In Figure 43 it is illustrated how the y-axis actuator and the x-axis actuator are mutually arranged. Before and after every change of resin the printhead crosses the x-axis actuator and because of leakage the resin drops from time to time onto the spindle. The movement of the x-axis actuator during the printing process transports the resin into the ball bearing and after a while the resin gets attached to the bearings which cures and congests the actuator. As a consequence, the ball bearing has to be fully disassembled, cleaned and reassembled. More critical is that the x-axis actuator sticks in its position while the printing process continues. A printing failure and spilling of resin and ethanol on top of the desk are the results of this incident.

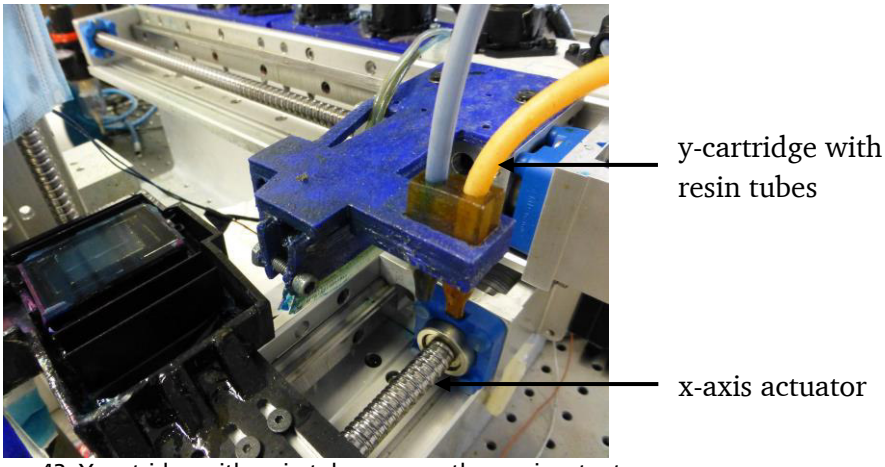

Figure 43: Y-cartridge with resin tubes crosses the x-axis actuator

Congestion of the x-axis actuator can be also caused by a blocked waste tube. This happens if pieces of the sample break apart or resin clusters get stuck in the drain. The main reason for this problem is the thin inner diameter of 3.175 mm of the waste tube. Besides the danger of congesting the x-axis actuator through the spilling of an ethanol and resin mix, this setting is also an enormous danger for the whole system. The electronics like the microcontroller are placed on the same desk as the multi-material printer and a huge overflow of the x-cartridge causes a flooding of the desk. This problem of the congested drain is shown in Figure 44.

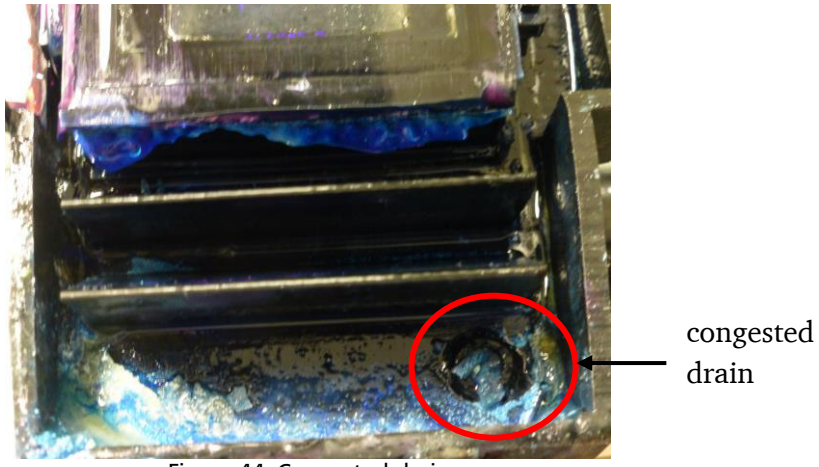

Figure 44: Congested drain

Another problem is the design of the x-cartridge. The x-cartridge consists out of nine parts that are printed on the Autodesk EMBER system and is shown in Figure 45. For assembling the x-cartridge the parts have to be glued together but the design does not have any planned fixing points or pins between the single parts so that every x-cartridge is unique. Consequence of this design is that the x-cartridge is often not exactly horizontal which means that the printing stage is not set completely flat on the PDMS window. Adjustments have to be made if possible for this case, otherwise the x-cartridge has to be broken apart and glued again or the parts have to be printed again if these steps are not working. Either way the height of the printing stage has to be adjusted in the code after replacing the x-cartridge which is time consuming. Another disadvantage that goes with this issue is that the accuracy of the multi-material printer gets lost because after the change of the height, the PDMS window is not anymore perfectly in focus.

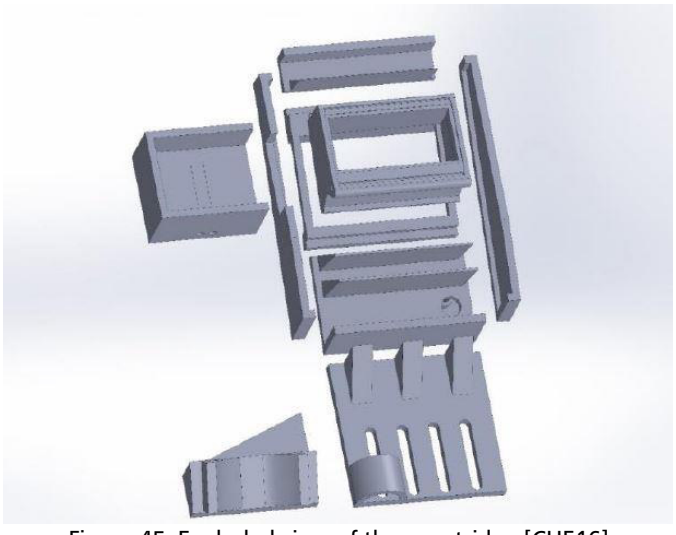
Figure 45: Exploded view of the x-cartridge [CHE16]

Furthermore, the dimension of the washing chamber of the x-cartridge is not suitable for this printing process. During the washing cycle water spills over and drops of ethanol drip onto the mirror which changes the focus on the PDMS window and reduces the quality of the printed sample or even leads to a printing failure. This incident is visualized in Figure 46 (a) and in Figure 46 (b) with the current solution of placing a bottle with paper beneath the washing chamber. In this way, the paper wipes the drops of the outer face of the washing chamber at every movement of the x-axis actuator.

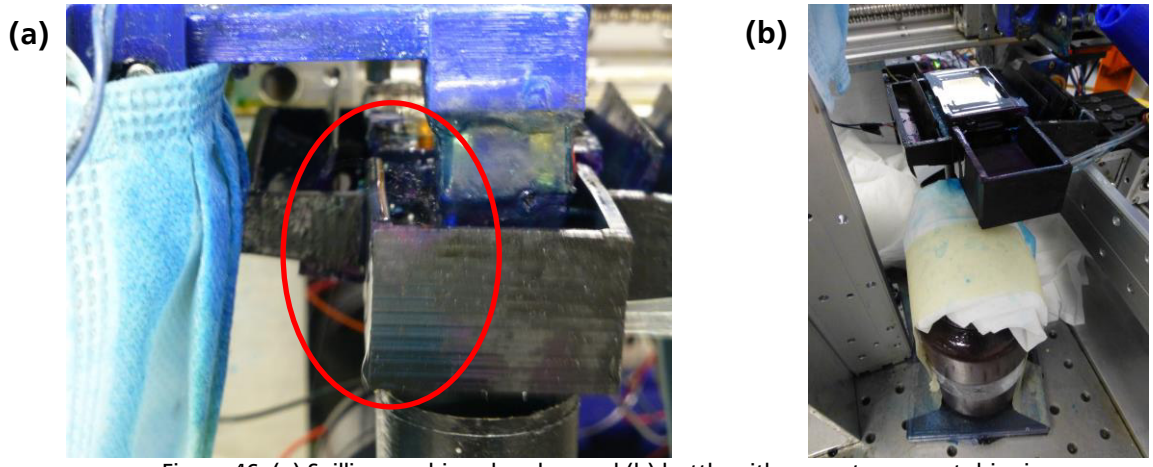

Figure 46: (a) Spilling washing chamber and (b) bottle with paper to prevent dripping

Besides the dimension of the washing chamber, the washing procedure has to be reconsidered. Currently the sample is washed with ethanol from the bottom. This works for resins with a low viscosity but a higher viscosity resin is hard to wash out because there will remain some resin close to the printing stage. Resin leavings in the sample will mix up the new deposited resin and will reduce the purity of the sample.

Another critical point of the x-cartridge is its low bending stiffness. Adhesive forces especially during the printing of the first few layers cause bending of the x-cartridge at the transition point right above the x-axis actuator. The bending stiffness of this design is computed by using a bar as an analogous model:

$$\begin{aligned} bending\ stiffness &= E * I \\ &= E * \frac{w * h^3}{12} \\ &= 550\ MPa * \frac{70\ mm * (20\ mm)^3}{12} \\ &= 25.67\ Nmm^2 \end{aligned} \qquad \text{[GHS11]}$$

Where E equals the Young's modulus of the Autodesk black resin with 550 MPa, and I the second moment of area with the width w of 70 mm and the height h of 20 mm of the area at the transition. For releasing the first few layers of every printed sample from the PDMS window the x-cartridge gets bended by moving the printing stage upwards. This action stresses the x-cartridge at the point where the part that is screwed on the x-axis actuator and the part with the drain are glued together. The consequences after printing several samples are cracks at this transition. Through these cracks the position of the x-cartridge changes by the time and an ethanol-resin mix spills over the x-axis actuator which causes congestion and blocks the x-axis actuator. An example for this case is shown in Figure 47.

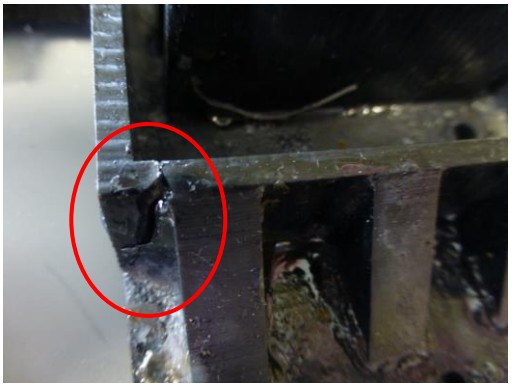

Figure 47: Crack at the x-cartridge

For drying the sample, a home-made fan is used. The fan is attached to the x-cartridge and blows at an angle of approximately 30°. During the drying process, ethanol and resin are blown out of the sample straight towards the z-axis actuator. This pollution leads to a malfunction of the z-axis actuator and contaminates the desk. At the moment, a surgical mask protects the z-axis actuator from congesting, which can be seen in Figure 48.

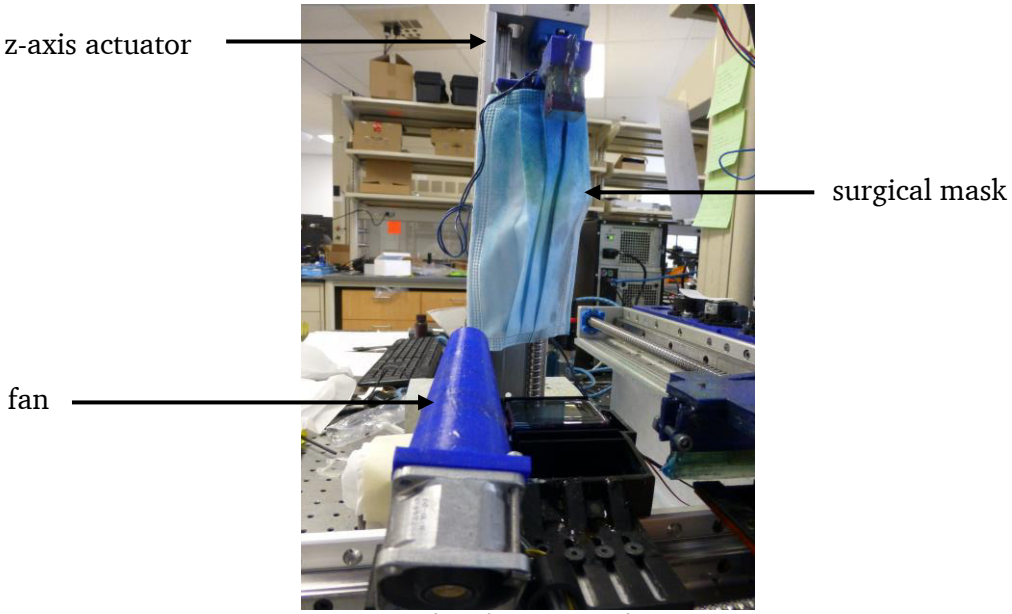

Figure 48: Surgical mask to protect the z-axis actuator

The last point that is notable to mention is the amount of resources the printer uses for the printing process. For the coating, an amount of 1.5 – 1.7 ml of the resin is necessary to cover the PDMS window at each change of resin. A usual sample, like the 2nd order unit cell with a skew angle of 60° has a height of 14 mm – subtracting the height of the support material – and consists in total of 692 layers. Hence there are 173 switches between the resins and the amount of used resin adds up to around 294.1 ml each. Additionally, the printer uses 26 ml of ethanol for each change of resin including the cleaning process of the PDMS window and the washing of the sample which is in total 4.5 l of ethanol.

These described issues including their impacts are summarized in Table 7 and show that the current multi-material printer is very insufficient and unstable.

Issue	Impact
Crossing of x- and y-axis:	- Congestion of the x-axis actuator - Flooding of the desk with ethanol
Congested drain:	- Congestion of x-axis actuator - Flooding of the desk with ethanol
Multipart x-cartridge:	- Lack of accuracy
Small washing chamber:	- Contamination of the mirror with ethanol - Loss of printing quality
Insufficient washing process:	- Loss of printing purity
Low stiffness of x-cartridge:	- Cracks and damage of the x-cartridge - Congestion of the x-axis actuator
Inappropriate drying process:	- Congestion of z-axis actuator - Contamination of the desk
Waste of resources:	- High amount of resins and ethanol required - Very costly

Table 7: Summary of the issues with impacts of the current multi-material printer

The aim is to improve the system regarding its availability as well as its efficiency regarding the use of materials. Ideas and objectives for the improvement of the system are noted down in the following list of requirements.

7.2 List of Requirements

By considering the current disadvantages of the multi-material printer the objectives for an update of the system are mainly an improvement of the availability and efficiency so that the need of supply is reduced dramatically and the multi-material printer operates in a sustainable way.

The pollution of the system by resin and ethanol has to be avoided by making a change in the arrangement of the system. This means that the x- and y- axis are not supposed to cross each other. Additionally, the contamination by the fan has to be eliminated. Referring to the x-cartridge the inclination of the PDMS window has to be adjustable and a change of the height is desirable. Also, the waste tube is supposed to work properly to drain off the liquids after each washing and cleaning cycle. Moreover, an increase of the stiffness of the x-cartridge is necessary to withstand the bending forces during the printing process. For the washing process, a redesign of the washing chamber as well as the washing process itself has to be considered. Currently the washing chamber is too small and the process of washing from below is not sufficient. Regarding the entire process and the resources, the challenge is to save at least 50% of resin and 50% of ethanol for three reasons. First of all, a smaller amount of resins and ethanol increases the efficiency of the multi-material printer. Secondly, the reduction leads to a more sustainable production. Last but not least, the saving of resources goes along with a saving of money. This means that the costs per sample get lowered. Desirable would also be a reduction of the cycle time which means printing two layers of each resin including the two washing cycles in less than 150 s.

These requirements of the updated multi-material system are summarized and listed in the Table 8 below and are separated in necessary requirements (NR), area requirements (AR), and desirable requirements (DR). They serve as a guide and orientation for the improvement of the multi-material printer.

	Req.	No.	Description	Data, Values, Explanations
Setup	NR	1	No pollution of the system by resin and ethanol	No crossing of resin tubes and actuators No contamination by the fan
x-cartridge	NR	2	Adjustable inclination of the PDMS window	After assembling the x-cartridge the possibility of readjustment has to be provided
	AR	3	Reliable liquid drain	Inner diameter > 3.175 mm and/or additional pump for the waste liquids
	NR	4	Increase stiffness of x-cartridge	New design of the frame with higher bending stiffness
Washing	NR	5	Redesign of washing process	Washing from just below is not sufficient
	AR	6	Redesign of the washing chamber	Area: > 20 x 15 mm Depth: > 20 mm Narrow enough to avoid spilling
Process / Resources	AR	7	Reduce the need of resin	Saving goal: > 50%
	AR	8	Reduce the need of ethanol	Saving goal: > 50%
	DR	9	Reduce the cycle time	Goal: < 150 s

Table 8: List of requirements for the updated multi-material printer

7.3 Development and Design of the new System

After analyzing the current state of the multi-material printer, revealing the problems, and setting up the list of requirements the next strategic approach for the improvement of the system is made in terms of a morphological matrix to find and evaluate concepts of a new system.

7.3.1 Morphological Matrix

At the beginning of the development of the updated system the morphologic matrix is a common method to figure out the different combinations that are given by various opportunities in each area. After brainstorming and reconsidering the possibilities of the current system Table 9 provides a survey of the options for improving the system.

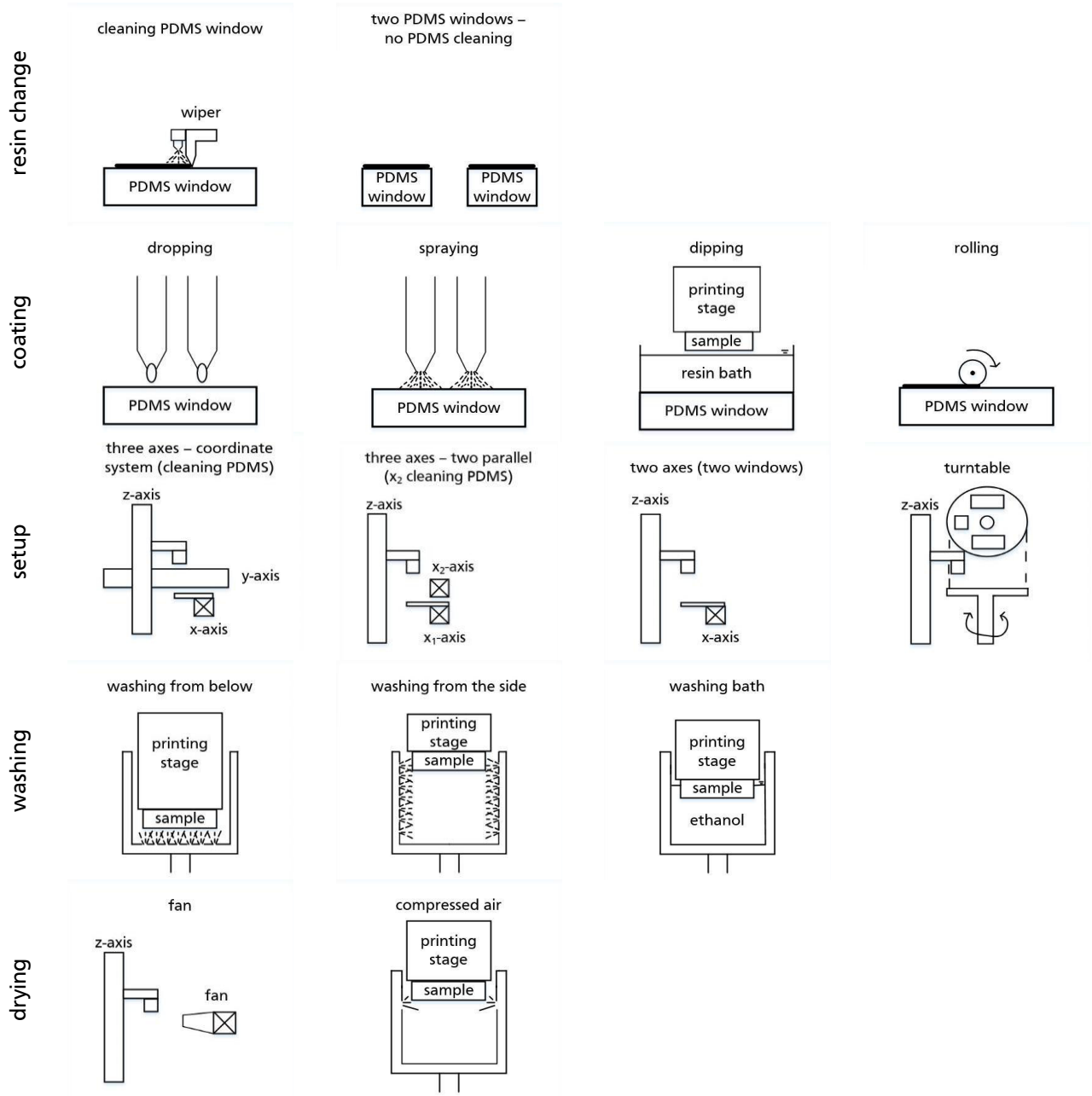

Table 9: Morphological matrix

There are two different ways to handle the change of resin. One way is to work with a single PDMS window that is used for both resins and cleaned at every change of the material. The other way is to utilize two PDMS windows, one for each resin. In this case no cleaning of the PDMS windows is necessary so that ethanol, which is used for this cleaning process, is saved.

For the process of recoating the dropping method is one option. Releasing a certain amount of resin drops on the PDMS window assures a completely covered printing area so that the layer is printable. Another option that works similar to the dropping method is the spraying method. Thereby, the resin gets sprayed onto the PDMS window with an injector. The coating of the PDMS window is also possible by permanent coverage with resin like a resin bath on top of the printing area. However, this method works only in combination with two PDMS windows because otherwise an enormous waste of resin for a change is inevitable. The fourth recoating possibility is the use of a roll soaked with resin to cover the PDMS window.

Arranging the setup for the multi-material printer offers, like the recoating process, four different possibilities. Firstly, the printer is built up on three axes like it is the current state. Secondly, also using three axes but arranged in a different way. Hereby, the x- and y-axis are set up parallel so that a crossing of these two axes is avoided. Thirdly, the y-axis gets eliminated so that in total only two axes are in use. However, this possibility requires necessarily the option with two PDMS windows to realize an accurate working and high-quality printing process. Fourthly, the x- and y-axis get substituted by a turntable that includes two PDMS windows as well as a method for washing and drying the sample.

Reconsidering the washing process opens various solution that operate by themselves or work in combination with each other. For the first two solutions, the ethanol gets injected into the washing chamber through several small holes either from the bottom of the washing chamber or from the side. In this way, the resin gets washed out of the sample and drains off with the ethanol through a waste tube on the bottom of the washing chamber. A more conservative operating method is a simple dipping of the sample into a bath of ethanol for a certain time period and shaking it by using either a vibrator on top of the printing stage or moving the sample up and down within the ethanol bath.

After washing the sample, the next step is to dry it before printing a new layer with the other resin. This process of drying is feasible by using a fan that blows out the ethanol leftovers. Moreover, using compressed air is another option for drying the sample. In this case the sample moves up and down between two notches that are connected to an air compressor and blow the sample dry.

In conclusion, there are at least two options of each area for developing new concepts of a multi-material printer. In the following section three different concepts are explained and discussed regarding their benefits and drawbacks before picking the best concept in a final evaluation.

7.3.2 Concept A “Current Multi-Material Printer”

The first concept, Concept A “Current Multi-Material Printer”, represents the prototype of the multi-material printer that is in use. Concept A uses a single PDMS window for the printing process. The coating is achieved by dropping the resins onto the printing area and the setup is arranged with three axes, where the y-axis crosses the x-axis. For the washing process, the sample gets washed from below and drying is enabled by using a fan. This concept serves as a benchmark for the other two concepts to

see if they are better or worse than the current multi-material printer. The advantages and disadvantages of Concept A “Current Multi-Material Printer” are listed in Table 10 below.

Advantages	Disadvantages
+ new resin for each cycle	- very high amount of resin and ethanol required
+ low cycle time	- contamination of the surroundings
+ drying speed	- danger of congestion of the drain
	- danger of congestion of the x-axis actuator
	- insufficient washing process

Table 10: Advantages and disadvantages of Concept A "Current Multi-Material Printer“

7.3.3 Concept B “Multi-Material Printer with Parallel Axes”

Concept B “Multi-Material Printer with Parallel Axes” uses one PDMS window and the method of spraying for recoating the printing area with resin. To avoid contamination the x- and y-axis of this system do not cross and are assembled in parallel. Also, the washing process is planned differently so that the ethanol gets injected from the side to wash off the resin. Moreover, for the drying process the option of drying the sample from two sides with compressed air is chosen. Benefits and drawbacks of this method are listed in Table 11.

Advantages	Disadvantages
+ new resin for each cycle	- high amount of resin and ethanol required
+ appropriate washing process	- slow drying process
+ no contamination	

Table 11: Advantages and disadvantages of Concept B "Multi-Material Printer with Parallel Axes"

7.3.4 Concept C “Multi-Material Printer with two PDMS Windows”

The third way of how to assemble the multi-material printer is Concept C “Multi-Material Printer with two PDMS Windows”. As the name already indicates this system uses two PDMS windows, one for each resin. The supply of resin for the recoating is provided by a resin bath on top of each PDMS window so that the printing area is covered with resin all the time. For this kind of setup only two axes, x- and z-axis, are required because the cleaning process for the PDMS windows no longer exists. Washing the sample is achieved through a combination of washing from the side and the ethanol bath. First the sample gets washed from the side, while the used ethanol fills up the washing chamber until the ethanol reaches the bottom of the notches for the compressed air. Then the printing stage moves up- and down within the resin bath while a vibrator on top of the printing arm excites the stage to improve the washing process. Afterwards, the sample is dried by compressed air as done in the previous concept. The pro and counter arguments for this concept are noted down in Table 12.

Advantages	Disadvantages
+ low amount of resin and ethanol required	- slow drying process
+ excellent washing process	
+ no contamination	
+ high reliability	

Table 12: Advantages and disadvantages of Concept C "Multi-Material Printer with two PDMS Windows"

These three concepts that make use of the various options of the morphological matrix lead to different results for the new system of the multi-material printer, respectively serve as a benchmark like the current version. To figure out whether the two new concepts are better than the current multi-material printer and if so, which one of these two offers the larger room for improvements, the concepts are rated in the following section.

7.3.5 Rating of the Concepts

For the rating of the concepts different assessment criteria are considered that are weighted regarding their importance. A weighting of three means that the criteria is very important for a proper working system. Hence, criteria like reliability, need of resin, cleanness – means no contamination – or the quality of the washing process have a weight of three. However, the total cycle time has a weight factor of one because for a prototype the clock cycle is not as important as it is for a machine that is supposed to work in mass production. For the criteria of maintenance effort, need of ethanol, and drying time the factor two is assigned because of their mediocre necessity for a successful printing system. For a better distinction, every criterion is rated with one, three, or nine for each concept. The ratings are multiplied by the weighting for each criterion and the products are added up to achieve the total points for the concept. In Table 13 a survey of the assessment criteria as well as the weighting and the total points for each concept are provided.

assessment criteria	weighting	concept A	points A	concept B	points B	concept C	points C
reliability	3	1	3	9	27	9	27
save of resin	3	1	3	3	9	9	27
save of ethanol	2	1	2	1	2	3	6
cleanness	3	1	3	9	27	9	27
maintenance effort	2	3	6	3	6	3	6
washing quality	3	1	3	3	9	9	27
drying time	2	9	18	3	6	1	2
total cycle time	1	9	9	1	1	1	1
sum			**47**		**87**		**123**

Table 13: Assessment matrix of the concepts for the multi-material printer

On the basis of the assessment matrix the rank of the concepts is clear. With 123 points Concept C “Multi-Material Printer with two PDMS Windows” gets the most points mainly because of its high reliability, the save of resources, as well as the cleanness and the washing quality. The low score on the total cycle time does not affect the results too much because of the weighting of one. Second place in this rating goes to Concept B “Multi-Material Printer with Parallel Axes”. This concept gets a score of 87 points and loses the most points in areas like the save of resin and ethanol as well as in the area of the washing quality in comparison to Concept C. The Concept A “Current Multi-Material Printer” gets the lowest score with 47 points. This result is traced back to the low reliability, the enormous waste of resources, the lack of cleanness and an insufficient washing quality. The high scores for the drying time and the total cycle time are not able to compensate this loss of points.

To sum it up, we can say that Concept B and Concept C are both better than Concept A which is currently in use. However, the assessment matrix points out that Concept C offers the most promising results for improvement. This is the reason why Concept C is chosen to be implemented to achieve primarily a higher reliability and a reduction in the need of resources.

7.4 Implementation of Concept C "Multi-Material Printer with two PDMS Windows"

The final step, after analyzing the current system, setting up a list of requirements, creating a morphological matrix with various options for a new system, generating concepts and their rating, is the implementation of the best concept. Concept C "Multi-Material Printer with two PDMS Windows" is chosen to be the system that is able to best fulfill the research objectives regarding high availability and saving of resources.

For the implementation a complete new design of the x-cartridge is necessary. But before describing the individual parts in detail the new x-cartridge is shown in the exploded view in Figure 49 to get an idea of how the new multi-material system is assembled.

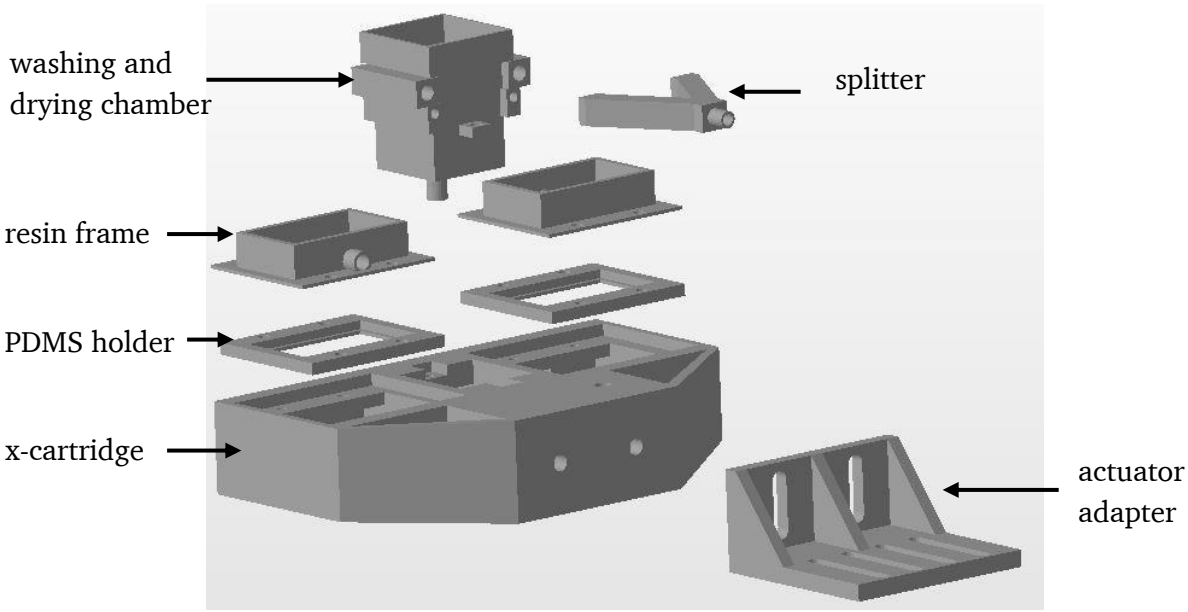

Figure 49: Exploded view of the new x-cartridge

The two PDMS windows are placed on the left- and the right-hand side of the washing and drying chamber which is placed in the middle of the x-cartridge. A splitter divides the airflow of the compressed air to each side of the drying chamber and the part at the right bottom corner is the actuator adapter that connects the x-axis actuator with the x-cartridge. The connection with inserted nuts at the transition enables an adjustment of the height and the slope after assembling the x-cartridge. Furthermore, the bending stiffness at the transition has been increased by the factor of 2.9 from 25.67 Nmm² up to 74.25 Nmm² by using the formula of chapter 7.1 with the same Young's modulus E but with the width w of 60 mm and the height h of 30 mm of the new design.

Both PDMS holders for the PDMS windows have a frame on top to serve as a resin vat. This connection is sealed with a rubber foil and by using two separate parts, the cleaning process at a change of resin is simplified and also allows a quick substitution. In the frame, there is a hole designed for a resin tube that is connected to a 12 V peristaltic pump that is controlled by Arduino for the automatic refill of the resin vat by pumping 1 ml every 7 min during the printing process. This is necessary because by lifting the printed sample and moving it towards the washing and drying chamber, resin leftovers remain in the free spaces of the sample and are removed from the resin vat. The CAD-model of one of the two PDMS holders and the frame for the resin vat are represented in Figure 50.

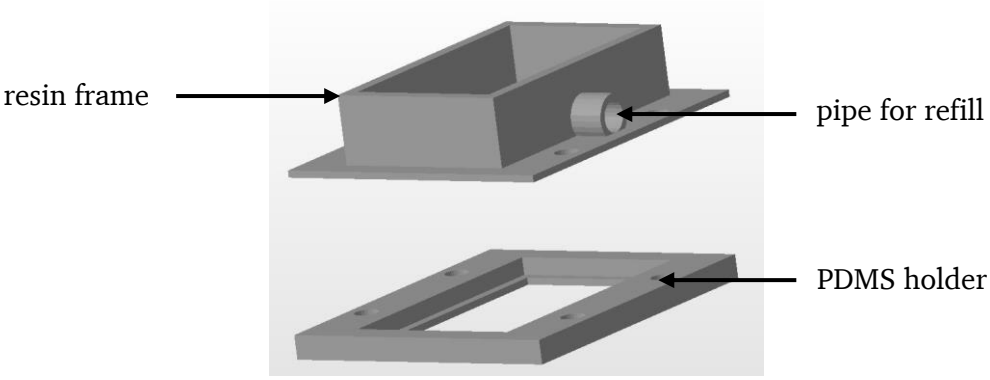

Figure 50: CAD-model of the PDMS holder and the frame for the resin vat

For washing the sample from the side and filling the washing chamber with ethanol, two 12 V peristaltic pumps are used and a third one is needed to suck the waste liquid out of the washing chamber before the drying process starts. Additionally, a vibrator that is already attached on top of the printing arm shakes when the sample is dipped into the ethanol bath. The dimension of the washing area is 24 x 24 x 21.6 (25) mm with a slope towards the drain. The red circle in Figure 51 points out that the washing process from the side is made up of nine rectangular pockets of the size of 1 x 0.25 mm. These pockets have an inclination of 15°, are arranged beneath the notch for the drying process, and face towards the top of the chamber. The size of the notches is 24 mm long by 1 mm high with an inclination of 5° towards the bottom of the chamber. This design change prevents the ethanol from spilling and dropping on the mirror as was the case in the previous setup. Also, the inner diameter of the drain increases by up to 4 mm and by adding the pump it is ensured that the tube does not get congested.

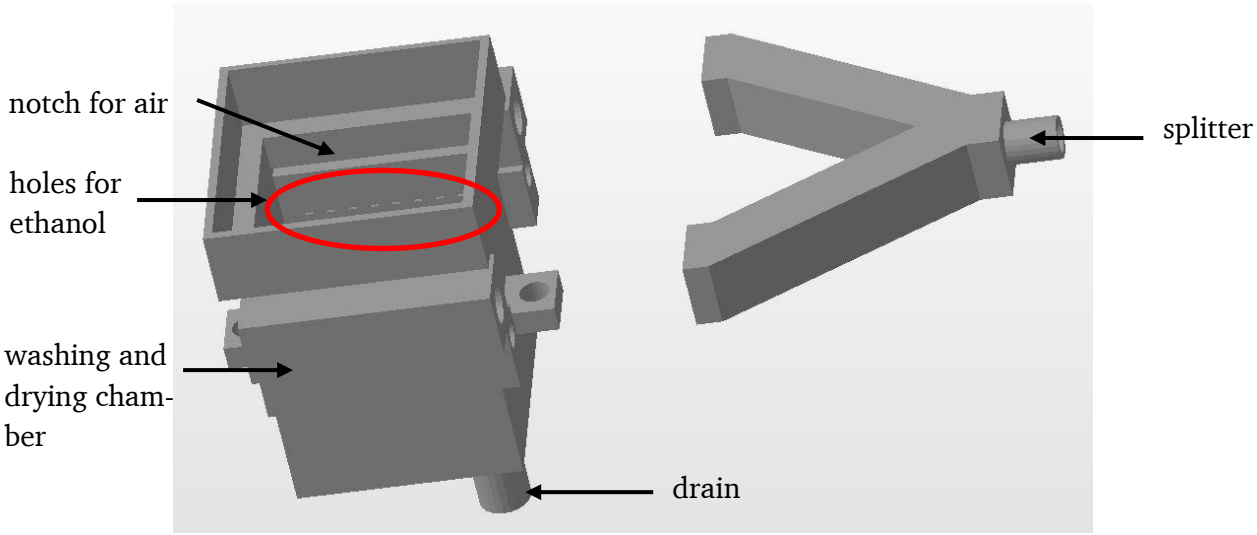

Figure 51: CAD-model of washing and drying chamber and splitter

A 12 V DC electric valve, which is closed at the powerless status, and a regulator provide a constant air pressure during the drying process. The air is led through a splitter to reach both sides of the chamber. The adjusted air pressure depends on the minimum size of the struts as well as the length to diameter ratio of the sample. In this case for a second order sample with a strut diameter of around 200 μm and a length to diameter ratio of 5:1 the pressure of the compressed air is set to 7.0 bar.

Combining the washing and drying function in one chamber creates a compact setup and protects the system from getting contaminated.

Figure 52 illustrates the applied changes of the new design of the multi-material printer. The white dot on top of the printing arm is the vibrator that shakes the printing stage during the washing process. The supply of resin and ethanol is ensured by their respective tubes at the frame and the washing chamber.

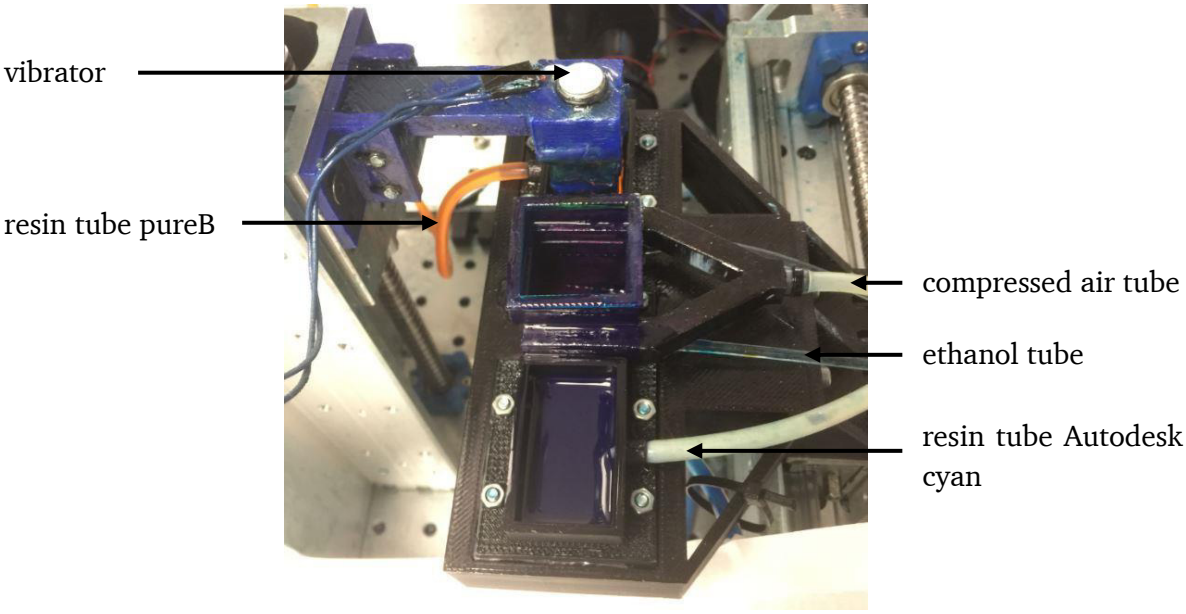

Figure 52: Setup of the new design of the multi-material printer

7.5 Results

The new setup for the multi-material printer comes with a lot of characteristic changes. The utmost objective was to increase the reliability of the system regarding repairs and downtimes as well as the dramatic reduction of the use of resin and ethanol. With a complete revision of the washing and drying process the system is able to run stable and no mix of ethanol and resin is blown into the z-axis by a fan. Reducing the number of axes from three to two axes eliminates the problem of the y-cartridge leaking while crossing the x-axis actuator. Also, the increase of the diameter of the drain and adding an additional pump prevents the system from congesting. Considering the efficiency of the new system, the amount of resin that is needed for a printing cycle of two layers of each resin is now just 0.5 ml because of the automatic refill every seven minutes. In comparison to the 1.7 ml needed for the former printing method there is a reduction of 72.0%. The change of the washing method and the abolition of the cleaning of the PDMS window leads to a decrease of the need of ethanol from 26 ml to 12 ml which is 53.8% less than before.

As a drawback of the updated multi-material system it should be mentioned that a reduction of the time for a printing cycle could not be accomplished. In contrast, the time increased by 33.3% from 150 s to 200 s. This rise is caused by the fact that it has to be made sure that leftovers within the sample are washed out completely and the sample is perfectly dried before dipping it into the other resin vat. For ensuring this, the washing and drying time of the new system have been increased. But by considering that the multi-material printer is made for manufacturing very small-series and not made for mass production the time, as already seen in the rating of the concepts, plays a minor part. Also, by the high reliability this drawback cancels out by printing time consuming samples overnight which was not possible with the previous unstable system.

In conclusion, we can say that the new design of the multi-material system is an enormous improvement regarding reliability and saving of resources which counterbalances the small drawback of the longer printing cycle. The final results of Concept C "Multi-Material Printer with two PDMS windows" are compared with the points in the list of requirements in Table 14 to show the rate of fulfillment and to verify the improvements.

	Req.	No.	Description	Achievements
Setup	NR	1	No pollution of the system by resin and ethanol	No contamination by avoiding crossing axes and using a new washing and drying chamber with compressed air
x-cartridge	NR	2	Adjustable inclination of the PDMS window	The new design enables adjustments in height and inclination even after assembling
	AR	3	Reliable liquid drain	Inner diameter: 4.0 mm, before 3.175 mm Additional pump added to suck out liquids
	NR	4	Increase stiffness of x-cartridge	Bending stiffness at the transition increased from 25.67 Nmm² to 74.25 Nmm² (factor 2.9)
Washing	NR	5	Redesign of washing process	Washing from the side plus ethanol bath
	AR	6	Redesign of the washing chamber	Dimension: 24 x 24 x 21.6 (25) mm Narrow and deep enough for printing area (20 x 15 mm) to avoid spilling
Process / Resources	AR	7	Reduce the need of resin	Resin saving: 72.0%, goal: > 50%
	AR	8	Reduce the need of ethanol	Ethanol saving: 53.8%, goal: > 50%
	DR	9	Reduce the cycle time	200 s, goal: < 150 s, 33.3% longer

Table 14: Rate of fulfillment of the list of requirements

This chapter about the improvement of the multi-material printer offers a way on how to approach setting up a new system. It starts with an analysis of the current state, figuring out the issues and the room for improvements by listing the requirements for the new multi-material printer. Then a morphological matrix is created providing the foundation for the creation of various concepts and with the help of an assessment matrix the best concept is chosen. Finally, the implementation of the improvements leads to a more reliable and resin saving multi-material printer and the results are verified by comparing them with the initially set objectives in the list of requirements.

In the last chapter of this thesis the work is reviewed by discussing the results and offering ideas for future research work.

8 Conclusion and Future Work

In the end, the gained knowledge about the coefficient of thermal expansion of multi-material hierarchical structures as well as the improvements of the multi-material printer is reviewed and prospects of future research work are provided.

8.1 Results

The results of the analytic prediction show that a negative thermal expansion of a 1st order octet-truss is only achievable in the z-direction and lowers with an increase of the CTE ratio of the two base materials and also with a decrease of the skew angle from 60° to 55°. For the 1st order unit cells there is still an expansion in x- and y-direction and thus the volumetric CTE is positive. By increasing the hierarchical order from one to two only the CTE $\alpha_{z,1st}$ of the 1st order sample matters and due to the fact that it is negative, the whole 2nd order unit cell shrinks uniformly. From the results, it can be seen that the skew angle θ has a higher impact on the volumetric CTE than the ratio between the two components. The minimum volumetric CTE for a 2nd order unit cell of an octet is -109.94 x 10^{-6} 1/°C at a skew angle of 60° and -299.38 x 10^{-6} 1/°C at an angle of 55°, both at a CTE ratio of 6:1.

At the thermal expansion tests of the multi-material structures of the 1st order octet-truss 60° shrinkage is clearly observable in all directions and thus the structure has a negative volumetric CTE. But this experimental result is in contrast to the analytic prediction that states that the sample is supposed to shrink in the z-direction and has a positive volumetric CTE for the 1st order unit cell. Considered as a possible reason for this deviation is the transgression of the glass transition temperature of pureB and thereby a change of the characteristics of the resin. The experimental results of the 2nd order samples for 60°, 55°, and 55° with new joints have a volumetric CTE of around zero or even slightly positive despite the results of the 1st order sample. Possible reasons considered for this case are an error of measurement by using the pixel measurement method, the not always completely printed joints of the samples, and the size effect. After examination of these reasons the latter – size effect – is determined to be the main reason for the deviation between the theory and the experimental results. A decrease of the strut diameter for higher order samples leads to cracks that break the struts apart and prevent the structure from shrinking. In contrast, the cracks force the 2nd order structures to expand.

By reviewing existing 1st order single-material unit cells, the shape of the dodecahedron and the quatraeder are spotted to be potential multi-material structures with the capability of a negative volumetric CTE. Simulative results point out that the quatraeder offers bigger opportunities regarding the thermal deformation by considering different strut ratios and for the dodecahedron changing the skew angle. Results for the 2nd order quatraeder demonstrate that the negative volumetric CTE of -360.94 x 10^{-6} 1/°C is even more negative at a strut ratio of 1.25:1 than it is for the octet-truss with -299.38 x 10^{-6} 1/°C at an angle of 55°.

For the multi-material printer, several challenges are considered to improve the system regarding reliability and the need of resources. An analysis of the current system points out in the list of requirements the room for improvements. With the help of a morphological matrix three concepts are created, rated, and the best one is chosen for future implementation. The new concept changes the printer from one to two PDMS windows and with this the recoating process is improved. Moreover, compressed air is used instead of a fan for the drying cycle. These changes are the key factors for a better and more stable

system. Additionally, the reconsideration of the washing process enables printing at a higher quality and with less blending of the different materials.

To put it in a nutshell, these improvements lead to a reduction in the use of resin by 72.0% and the use of ethanol by 53.8%. The 33% increase in time for the printing process is compensated by the higher reliability and the elimination of break downs. This is also the reason that the printer is still a prototype and manufacturing only small-series and not high volume.

8.2 Future Work

Further steps to proceed in this research area are to increase the printing area of the multi-material printer to eliminate the size effect for higher order structures. Moreover, the goal is to print at least five samples to conduct a series of tests to increase the accuracy of the thermal expansion tests. By using a bigger sample size, outliers can be easily detected and removed. Also, new resins should be considered that are resistant and avoid cracking at high temperatures. If possible, it would also be good to have an even higher CTE ratio than the Autodesk cyan to pureB ratio of 5.9:1.

Besides the adjustments for the approach of the thermal expansion tests, the structure of the quatraeder should be investigated for the 1st and 2nd order to confirm the simulative results and widen the area of unit cells with potential for a negative volumetric CTE. Also, the mechanical properties of this quatraeder unit cell should be investigated and compared with the multi-material octet-truss.

8.3 Summary

In conclusion, we can say that the theory offers some approaches to deal with the problem of undesired thermal expansion. With the 1st order unit cell of an octet-truss a negative deformation in the z-direction is achievable, while the 2nd order unit cell offers the possibility of a uniform negative deformation. But the results of the subsequently conducted thermal expansion tests are in contrast to the analytically predicted values leading to the discovery that the total size of the struts of the microscale structures influences the results of the tests. The smaller the strut diameter, the more vulnerable the struts are to cracks resulting in poor or unexpected test results. Besides the octet-truss, in simulation the quatraeder shows a high potential for achieving a negative volumetric CTE in a range that is even lower than the one for the octet-truss.

In addition to the investigations of the unit cells regarding the negative thermal expansion, changes to the multi-material printer are also studied to improve the system with regards to its reliability and efficiency. The new system uses two PDMS windows and a redesigned washing and drying chamber with compressed air instead of a fan. In this way, the research objectives are met and the disadvantage of the longer printing time is compensated by the fact that clock cycle is not the main criterion for a prototype. With these improvements, the new multi-material printer can run stable without any off times and will save an enormous amount of resources. In this way, more samples at lower costs can be built and with testing a larger series of unit cells the thermal expansion tests lead to more accurate results.

9 References

[AE13] T. Atkins, M. Escudier, “A Dictionary of Mechanical Engineering”, Oxford University Press, 1st ed., Jan. 2013.

[AND15] R. Anderl, “Virtual Product Development A”, lecture, fall term, 2015/2016.

[BÁR11] P. J. Bártolo, “Stereolithography - Materials, Processes and Applications”, New York, Springer, 2011.

[BBR01] A. Bertsch, P. Bernhard, and P. Renaud, “Microstereolithography: Concepts and applications”, IEEE, vol. 2, pp. 289-298, EFTA 2001.

[BF16] C. Beyer, D. Figueroa, “Design and Analysis of Lattice Structures for Additive Manufacturing”, J. of Manufacturing Science and Engineering, vol. 138, pp. 121014-121014-15, Dec. 2016.

[BGB15] A. Bandyopadhyay, T. PL. Gualtieri, S. Bose, “Global Engineering and Additive Manufacturing”, Additive Manufacturing, CRC Press, pp. 1-18, 2015.

[BJB02] A. Bertsch, S. Jiguet, P. Bernhard, P. Renaud, “Microstereolithography: a Review”, MRS Online Proceedings Library, vol. 758, Jan. 2002.

[BM15] A. H. Blackwell, E. Manar, “Prototype”, UXL Encyclopedia of Science, Science in Context, 3rd ed., 2015.

[BS12] H.-J. Bargel, G. Schulze, “Werkstoffkunde”, Springer Vieweg, Berlin, 11th ed., 2012.

[CM14] C. J. Cleveland, C. G. Morris, “Dictionary of Energy - Second Edition”, Elsevier Ltd., p.117, 2014.

[CMW10] J.-W. Choi, E. MacDonald, R. Wicker, “Multi-material microstereolithography”, Springer, The International Journal of Advanced Manufacturing Technology, vol. 49, pp. 543-551, Jul. 2010.

[CWL09] J.-W. Choi, R. Wicker, S.-H. Lee, K.-H. Choi, C.-S. Ha, and I. Chung, “Fabrication of 3D biocompatible/biodegradable micro-scaffolds using dynamic mask projection microstereolithography”, J. Mater. Process. Technol., vol. 209, no. 15-16, pp. 5494-5503, Aug. 2009.

[DZ17] P. Dudek, K. Zagórski, “Cost, resources, and energy efficiency of additive manufacturing”, EDP Science, E3S Web of Conference, vol. 14, start page 01040, Jan. 2017.

[GHS11] D. Gross, W. Hauger, J. Schröder, W. A. Wall, J. Bonet, “Engineering Mechanics 2 – Mechanics of Materials”, Heidelberg, Springer, 2011.

[GIL10] D. G. Gilmore, “Spacecraft Thermal Control Handbook”, The Aerospace Press, 2nd ed., Oct. 2002.

[GJS08] P. Glöckner, T. Jung, S. Struck, K. Studer, “Radiation Curing – Coatings and Printing Inks”, Vincentz Network, May 2008.

[GR15] M. J. Galba, T. Reischle, “Additive Manufacturing of Metals Using Powder-Based Technology”, Additive Manufacturing, CRC Press, pp. 97-142, 2015.

[GRS15] I. Gibson, D. Rosen, B. Stucker, “Additive Manufacturing Technologies – 3D Printing, Rapid Prototyping, and Direct Digital Manufacturing”, Springer, New York, 2nd ed., 2015.

[HCL08] Y. M. Ha, J. W. Choi, S. H. Lee, “Mass production of 3-D microstructures using projection microstereolithography”, J. of Mechanical Science and Technology, vol. 22, pp. 514-521, Mar. 2008

[HNK10] M. A. Hopcroft, W. D. Nix, T. W. Kenny, “What is the Young’s Modulus of Silicon?”, J. of Microelectromechanical Systems, IEEE, vol. 2, pp. 229-238, Apr. 2010.

[HOR06] E. Hornbogen, “Werkstoffe – Aufbau und Eigenschaften”, Springer, Berlin Heidelberg, 8th ed., 2006.

[IS10] B. Ilschner, R. F. Singer, “Werkstoffwissenschaften und Fertigungstechnik – Eigenschaften, Vorgänge, Technologien”, Springer, Berlin, Heidelberg, 5th ed., 2010.

[KFG08] P. Kurzweil, B. Frenzel, F. Gebhard, “Physik Formelsammlung – Für Ingenieure und Naturwissenschaftler”, Wiesbaden, Vieweg, 2008.

[KMN14] S. Koltzenburg, M. Maskos, O. Nuygken, “Polymere – Synthese, Eigenschaften und Anwendungen”, Springer, Berlin Heidelberg, 2014.

[LAM14] P. M. Lambert, “Design and Fabrication of a Mask Projection Microstereolithography System for the Characterization and Processing of Novel Photopolymer Resins”, Master’s Thesis, Virginia Polytechnic Institute and State University, Jun. 2014.

[LIM07] A. S. Limaye, “Multi-objective process planning method for mask projection stereolithography”, dissertation, Georgia Institute of Technology, Dec. 2007.

[LMS06] Y. Lu, G. Mapili, G. Suhali, S. Chen, K. Roy, “A digital micro-mirror device-based system for the microfabrication of complex, spatially patterned tissue engineering scaffolds”, J. of biomedical materials. Part A, vol. 77A, pp. 396-405, Jan. 2006

[MLC99] S. Monneret, V. Loubère, S. Corbel, “Microstereolithography using a dynamic mask generator and a non-coherent visible light source”, Design, Test, and Microfabrication of MEMS, vol. 3680, pp. 553-561, Mar. 1999.

[MS16] S. S. Muthu, M. M. Savalani, “Handbook of Sustainability in Additive Manufacturing: Volume 2”, Springer, Singapore, 2016

[MW05] W. Martienssen, H. Warlimont, “Handbook of Condensed Matter and Materials Data”, Springer, Berlin, Heidelberg, New York, 2005.

[PHL11] I. B. Park, Y. M. Ha, S. H. Lee, “Dithering method for improving the surface quality of microstructure in projection microstereolithography”, Int. J. Adv. Manuf. Technol., vol. 52, no. 5, pp. 545-553, Feb. 2011.

[PZC12] Y. Pan, C. Zhou, Y. Chen, “A Fast Mask Projection Stereolithography Process for Fabrication Digital Models in Minutes”, J. of Manufacturing Science and Engineering, vol. 134, pp. 051011-1 – 051011-9, Oct. 2012.

[SCH14] B. Schröder, “Kunststoffe für Ingenieure – Ein Überblick”, Springer Vieweg, Wiesbaden, 2014.

[SH14] J. Stampfl, M. Hatzenbichler, “Additive Manufacturing Technologies”, CIRP Encyclopedia of Production Engineering”, Springer, pp. 20-27, 2014.

[SFW05] C. Sun, N. Fang, D. M. Wu, X. Zhang, “Projection micro-stereolithography using digital micro-mirror dynamic mask”, Sensors & Actuators: A. Physical, vol. 121, pp. 113-120, 2005.

[STR00] V. Strehmel, “Bildung und Struktur vernetzter temperaturstabiler polymerer Materialien”, Professorial Dissertation, Martin-Luther-Universität Halle-Wittenberg, Mar. 2000.

[TS00] K. Takahashi, J. Setoyama, “A UV-Exposure System Using DMD”, Electronics and Communications in Japan (Part II: Electronics), vol. 83, pp. 56-58, Jul. 2000.

[VA16] R. Vaidya, S. Anand, “Optimum Support Structure Generation for Additive Manufacturing Using Unit Cell Structures and Support Removal constraint”, Procedia Manufacturing, vol. 5, pp. 1043-1059, 2016.

[WWH16] V. Weißmann, J. Wieding, H. Hansmann, N. Laufer, A. Wolf, R. Bader, “Specific Yielding of Selective Laser-Melted Ti6Al4V Open-Porous Scaffold as a Function of Unit Cell Design and Dimensions”, Metals, vol. 6, p. 166, Jul. 2016.

[www0] https://ember.autodesk.com/overview#tech_specs, loaded 04.28.17.

[www1] http://www.instron.us/en-us/products/testing-accessories/environmental-chambers-furnaces/environmental-chambers/chambers/3119-609, loaded 06.17.17.

[www2] https://us.vwr.com/store/product/4639460/vwr-professional-hot-plates, loaded 07.28.17.

[www3] https://www.boreal.com/store/product/8892247/vwr-analog-hotplate-stirrers, loaded 07.28.17.

[XP16] H. Xu, D. Pasini, “Structurally Efficient Three-dimensional Metamaterials with Controllable Thermal Expansion”, Scientific Reports, vol. 6, pp. 34924-1 – 34924-8, Oct. 2016.

[YHB17] L. Yang, K. Hsu, B. Baughman, D. Godfrey, F. Medina, M. Menon, S. Wiener, “Additive Manufacturing of Metals: The Technology, Materials, Design and Production”, Springer, 2017.

[YGT14] N. Yamamoto, E. Gdoutos, R. Toda, V. White, H. Manohara, C. Daraio, “Thin Films with Ultra-low Thermal Expansion”, Advanced Materials, vol. 26, pp. 3076 – 3080, May 2014.

[ZLW14] X. Zheng, H. Lee, T. H. Weisgraber, M. Shusteff, J. DeOette, E. B. Duoss, J. D. Kuntz, M. M. Biener, Q. Ge, J. A. Jackson, S. O. Kucheyev, N. X. Fang, C. M. Spadaccini, “Ultralight, Ultrastiff Mechanical Metamaterials”, Science, vol. 344, pp. 1373-1377, Jun. 2014.

10 Appendix

10.1 Derivation of the Coefficient of Thermal Expansion in z-direction

Assumption of linear elastic thermal expansion whereas nonlinearities are not considered.

Definitions:

l_1: length of material with high CTE

l_2: length of material with low CTE

α_1: CTE of material with high CTE

α_2: CTE of material with low CTE

h_{tri}: height of the triangle

h_{tet}: height of the tetrahedron

ΔT: temperature difference between initial and final state

θ: skew angle

Computation of the height in tetrahedron at initial state:

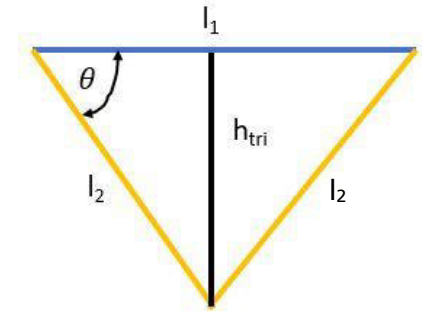

$$h_{tri} = sin\theta * l_2$$

$$cos\theta = \frac{\frac{1}{2}l_1}{l_2} \rightarrow \frac{l_1}{l_2} = 2 * cos\theta \qquad (a)$$

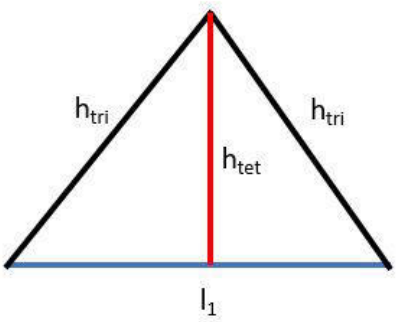

$$h_{tet} = \sqrt{{h_{tri}}^2 - \left(\frac{1}{2}l_1\right)^2}$$

Computation of the height in the tetrahedron at the final state (after heating up the sample by ΔT):

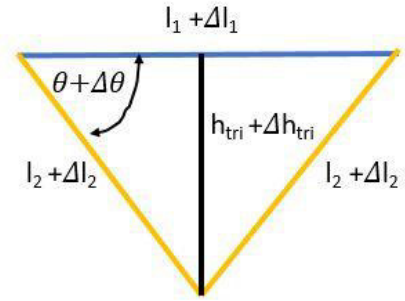

$$h_{tri} + \Delta h_{tri} = \sqrt{(l_2 + \alpha_2 \Delta T l_2)^2 - \left(\frac{1}{2} l_1 + \alpha_1 \Delta T \frac{1}{2} l_1\right)^2}$$

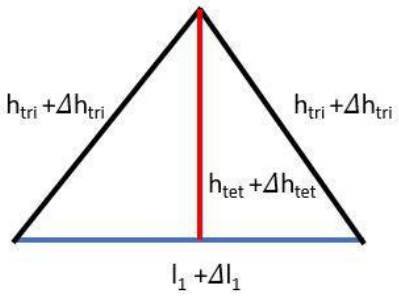

$$h_{tet} + \Delta h_{tet} = \sqrt{(h_{tri} + \Delta h_{tri})^2 - \left(\frac{1}{2} l_1 + \alpha_1 \Delta T \frac{1}{2} l_1\right)^2}$$

$$\alpha_z = \frac{1}{\Delta T} * \frac{h_{tet} + \Delta h_{tet} - h_{tet}}{h_{tet}} =$$

$$= \frac{1}{\Delta T} * \frac{\sqrt{\left(\sqrt{(l_2 + \alpha_2 \Delta T l_2)^2 - \left(\frac{1}{2} l_1 + \alpha_1 \Delta T \frac{1}{2} l_1\right)^2}\right)^2 - \left(\frac{1}{2} l_1 + \alpha_1 \Delta T \frac{1}{2} l_1\right)^2} - \sqrt{(sin\theta * l_2)^2 - \left(\frac{1}{2} l_1\right)^2}}{\sqrt{(sin\theta * l_2)^2 - \left(\frac{1}{2} l_1\right)^2}} =$$

$$= \frac{1}{\Delta T} * \frac{\sqrt{{l_2}^2 (1 + \alpha_2 \Delta T)^2 - \frac{1}{4} {l_1}^2 (1 + \alpha_1 \Delta T)^2 - \frac{1}{4} {l_1}^2 (1 + \alpha_1 \Delta T)^2} - \sqrt{(sin\theta * l_2)^2 - \frac{1}{4} {l_1}^2}}{\sqrt{(sin\theta * l_2)^2 - \frac{1}{4} {l_1}^2}} =$$

multiplying numerator and denominator with $\frac{1}{{l_2}^4}$ *plus using equation* (a):

$$\alpha_z = \frac{1}{\Delta T} * \frac{\sqrt{(1 + \alpha_2 \Delta T)^2 - 2cos^2\theta (1 + \alpha_1 \Delta T)^2} - \sqrt{sin^2\theta - cos^2\theta}}{\sqrt{sin^2\theta - cos^2\theta}} =$$

using addition theorem:

$$\alpha_z = \frac{1}{\Delta T} * \frac{\sqrt{(1 + \alpha_2 \Delta T)^2 - 2cos^2\theta (1 + \alpha_1 \Delta T)^2} - \sqrt{1 - 2cos^2\theta}}{\sqrt{1 - 2cos^2\theta}}$$

10.2 Images of the Base Material of the Thermal Expansion Tests

	At T = 22°C	At T = 150°C
Autodesk black	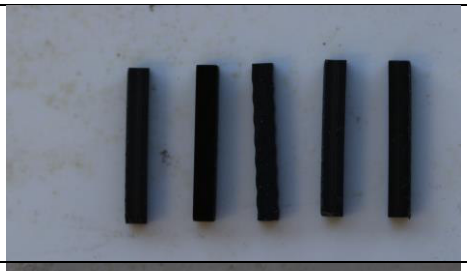	
Autodesk clear	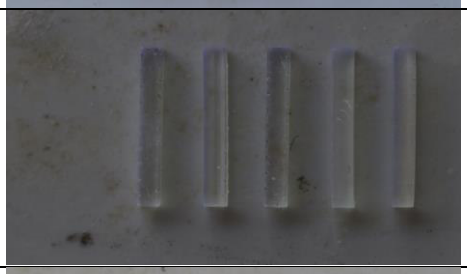	
Autodesk cyan	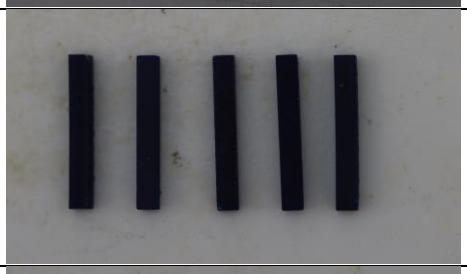	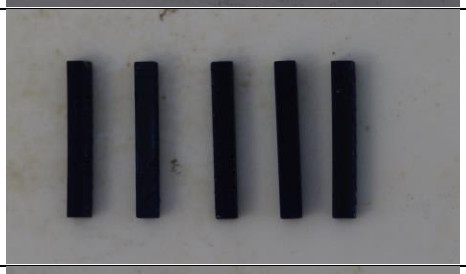
formlabs flexible	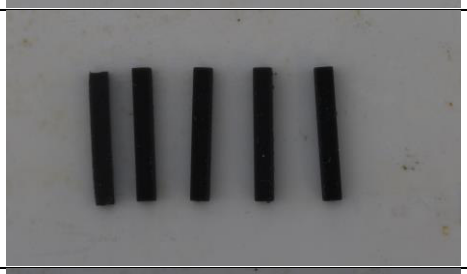	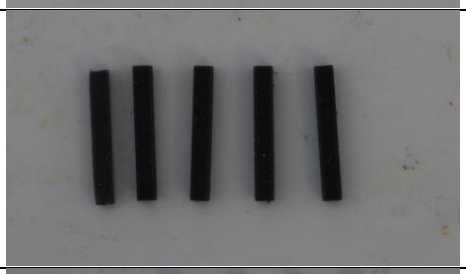
pureA		
pureB	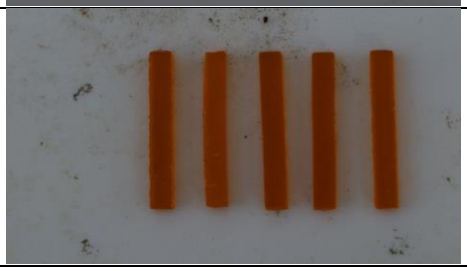	

10.3 Images of the 1st and 2nd Order Unit Cells of the Thermal Expansion Tests

	At T = 22°C	At T = 150°C
1st order unit cell 60° x-y-axis		
1st order unit cell 60° z-axis	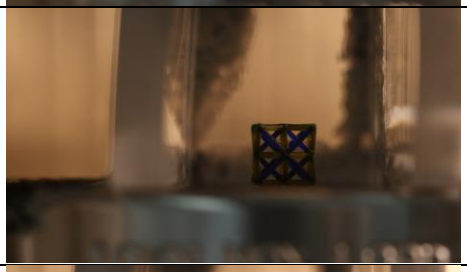	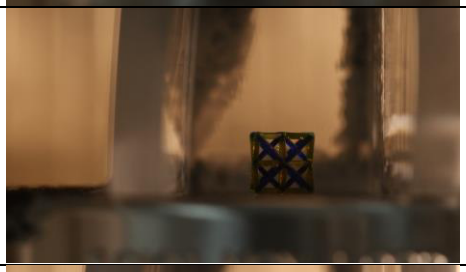
2nd order unit cell 60° x-y-z-axis	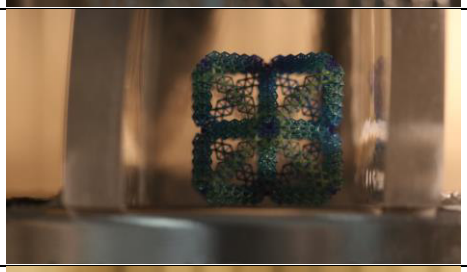	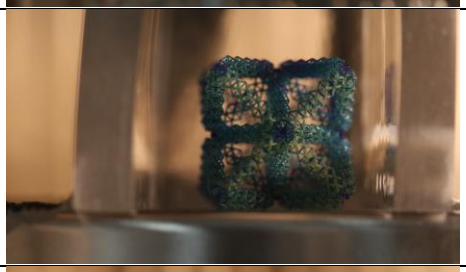
2nd order unit cell 55° x-y-axis	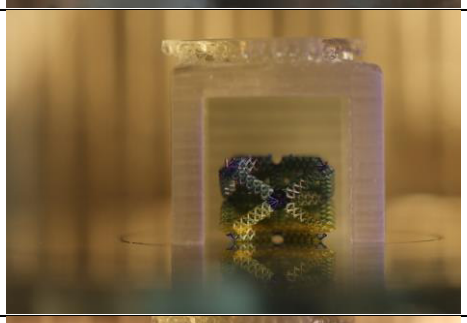	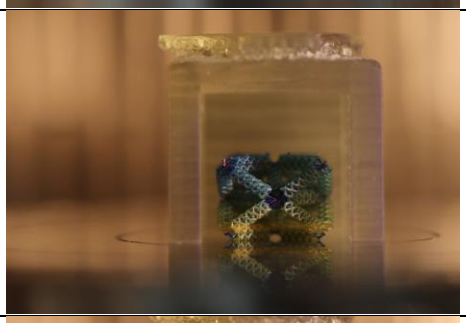
2nd order unit cell 55° z-axis	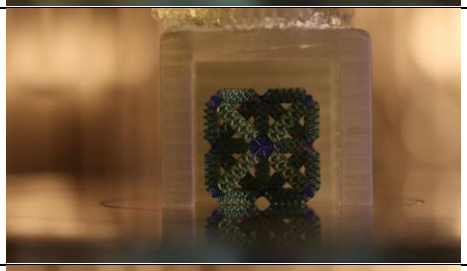	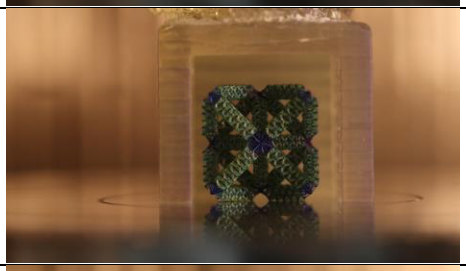
2nd order unit cell 55° new joints x-y-axis